



universität
wien

DIPLOMARBEIT

Titel der Diplomarbeit

Depth-resolved PIXE analysis with a polycapillary X-ray lens

angestrebter akademischer Grad

Magister der Naturwissenschaften (Mag. rer. nat.)

Verfasser:	Lea Reichhart
Matrikel-Nummer:	0305857
Studienrichtung:	411 Physik
Betreuer:	Ao. Univ.-Prof. DI Dr. Robin Golser

Wien, am 1. Dezember 2008

Abstract

Proton induced X-ray emission spectroscopy (PIXE) is a well-known non-destructive method for elemental analysis. By extending the established external PIXE-setup at the Vienna Environmental Research Accelerator (VERA) with polycapillary optics, depth resolved measurements could be performed. By means of external total reflection, polycapillaries show focusing abilities for X-rays, most suited for the energy range of some keV. Various capillary-setups were mounted in front of one X-ray detector at VERA. The intersection between the proton beam (about 150 μm in diam.) and the "tube-shaped" detection channel (of the order of 100 μm in diam.) defines a small volume, where X-rays can be detected from. By mechanically moving a target through this intersection, depth-dependent information of elemental composition was evaluated. In the course of the experimental work three different types of polycapillaries have been used. In particular a half-lens, a lens and a Poly-CCC (Polycapillary conic collimator) have been characterized with respect to focusing behavior and other spatial properties as well as transmission features as function of X-ray energy. All these qualities are lumped together in the so called sensitivity curve for each polycapillary in the VERA setup. These curves are the results of depth scans performed with an artificial foil-sandwich, which consists of single element foils. The foil-sandwich is ideally suited to measure the size of the detection volume for each polycapillary as a function of X-ray energy. By analyzing the intensity during the depth scans the transmission of X-rays through the polycapillaries relative to a second detector was determined. The maximum transmission is $\approx 4\%$ for the half-lens, $\approx 30\%$ for the lens and $\approx 40\%$ for the Poly-CCC, respectively. Moreover, the near Gaussian shape of depth scans (FWHM $\approx 200\ \mu\text{m}$, $\approx 500\ \mu\text{m}$, and $\approx 250\ \mu\text{m}$ for half-lens, lens and Poly-CCC, respectively) allows centroid analysis with a resolution of a few μm . For real-world samples, an enhancement of the signals from the surface relative to the bulk can be realized by locating the sample surface at the margin of the detection volume. Thus, polycapillaries with high transmission, in particular Poly-CCC are perfectly suited for PIXE analysis of drawings.

In addition, the accuracy of the PIXE-ART facility at VERA was verified by comparing results from XRF-measurements at the Academy of Fine Art in Vienna and from PIXE-measurements at the Louvre in Paris. Objects of interest were art historical samples, e.g. coins from the time of the Roman Caesar Traian and from the Ottoman empire. All assessed absolute values of elemental concentrations agree within 2 % or better.

Zusammenfassung

Protonen-induzierte Röntgenemissions-Spektroskopie (PIXE) ist eine etablierte Methode zur zerstörungsfreien Elementanalyse. Der PIXE-ART Aufbau bei VERA (Vienna Environmental Research Accelerator) wurde mit Hilfe von Polykapillarlinsen um die Möglichkeit zur Durchführung tiefenaufgelöster Messungen erweitert. Polykapillaren besitzen auf Grund externe Totalreflexion, die bei Röntgenstrahlung beim Übergang von Luft in Materie auftritt, fokussierende Eigenschaften. Es entsteht ein zylinderförmiger Fokusbereich ($\approx 100 \mu\text{m}$ im Durchmesser). Die Taille dieses Nachweisbereiches der Polykapillare, die koaxial mit dem Detektor positioniert wird, schneidet sich mit dem ebenso zylinderförmigen Anregungsvolumen des einfallenden Protonenstrahls ($\approx 150 \mu\text{m}$ im Durchmesser). Dieses Schnittvolumen definiert einen Raumbereich aus dem Röntgenstrahlung detektiert werden kann. Wird nun manuell eine Probe durch diesen Bereich bewegt, erhält man Informationen über die Elementverteilung als Funktion der Tiefe. Im Rahmen der Diplomarbeit wurden drei verschiedene Typen von Polykapillaren verwendet und ihre Eigenschaften charakterisiert. Im speziellen handelte es sich um eine Halblinse, eine Linse und eine Poly-CCC (Polycapillary conic collimator). Das Fokussierverhalten einer Polykapillare und die damit im Zusammenhang stehende Änderung des Detektionsvolumen in Abhängigkeit von der Energie der Röntgenstrahlung, kann durch eine sogenannte Sensitivitätskurve beschrieben werden. Die Kurven resultieren aus gemessenen Tiefenprofilen unterschiedlicher, künstlich hergestellter Foliensandwiches. Diese sind aus μm -dünnen, nur aus einem Element bestehenden Metallfolien aufgebaut. Die aufgenommenen Tiefenprofile folgen beinahe perfekt der Form einer Gaußverteilung (FWHM $\approx 200 \mu\text{m}$, $\approx 500 \mu\text{m}$, und $\approx 250 \mu\text{m}$ für Halblinse, Linse und Poly-CCC). Dies erlaubt eine Schwerpunktsbestimmung (und damit Ortsangabe) mit einer Auflösung von nur wenigen μm . Durch die gemessenen Intensitäten in den Tiefenprofilen konnte eine Transmissionskurve für die jeweilige Polykapillare ermittelt werden (maximale Transmission $\approx 4 \%$, $\approx 30 \%$, und $\approx 40 \%$ für Halblinse, Linse und Poly-CCC). Diese Werte wurden relativ zu einem zweiten Röntgendetektor bestimmt und sind wie auch alle anderen gemessenen Eigenschaften der Polykapillaren charakteristisch für das bei VERA gegebene Protonenstrahlprofil und Detektorsetup. Bei praktischen Messungen können durch die Positionierung des Detektionsvolumen genau vor der zu untersuchenden Probe die Signale aus der Oberfläche bevorzugt, die aus dem Untergrund stark unterdrückt werden. Im Falle der Poly-CCC, die sehr gute Transmission aufweist, ist das ein großer Gewinn für die Untersuchung wertvoller Zeichnungen.

Zusätzlich wurde die externe PIXE-ART Anlage bei VERA auf ihre Genauigkeit überprüft. Dies wurde durch den Vergleich mit der XRF-Anlage an der Akademie der Bildenden Künste in Wien und der PIXE-Anlage am Louvremuseum in Paris erreicht. Gegenstand der Messungen waren kunsthistorische Proben, zum Beispiel Denare aus der Zeit des römischen Kaisers Traian und Münzen aus dem osmanischen Reich. Die ermittelten Elementkonzentrationen stimmen auf 2 % oder besser überein.

Contents

1	Introduction and motivation	1
2	Theoretical considerations	3
2.1	PIXE	3
2.1.1	External PIXE	3
2.1.2	Principle of PIXE, Moseley’s Law	4
2.1.3	Fluorescence yield, Auger process	5
2.1.4	Ionization cross section	6
2.1.5	Protons in matter	7
2.1.6	X-rays in matter	8
2.1.7	X-ray detection	9
2.1.8	X-ray yield	10
2.2	Polycapillary X-ray optics	12
2.2.1	Properties of polycapillary x-ray optics	14
2.2.2	Transmission through glass capillaries	16
2.2.3	Comparison and features of polycapillary types	18
2.2.4	Summary of properties	19
3	Experimental setup	21
3.1	The accelerator of VERA	21
3.1.1	Beam trajectory simulations	23
3.2	The PIXE assembly at VERA	25
3.2.1	Detection setup	26
3.2.2	Proton beam profile	29
4	Depth resolved measurements	31
4.1	Characterization of Polycapillaries	31
4.1.1	Specification of the target sandwich	31
4.1.2	Preparations, measurements and results	33
4.1.3	A coin sample	45
5	Determination and verification of elemental concentrations	47
5.1	Description of the samples for verification	47
5.1.1	Traian coins	47
5.1.2	Coins from the Ottoman Empire	49
5.1.3	Iridescent Art Nouveau glass	49

5.2	GUPIXWIN	50
5.2.1	Detector efficiency	50
5.3	Results	52
5.3.1	Standards	52
5.3.2	Traian coins	54
5.3.3	Ottoman Empire coins	57
5.3.4	Iridescent glass samples	58
5.4	Possibilities with the use of Polycapillaries	61
5.4.1	Determination of concentrations	61
5.4.2	Measurements and Results	61
6	Conclusion and Outlook	65
A	Appendix	67
A.1	Depth scans of foil sandwiches	67
A.1.1	Cu-Ti	68
A.1.2	Fe-Cu	73
A.1.3	Fe-Au	77
A.1.4	Ti-Fe	80
B	Appendix	83
B.1	Guiding protons through polycapillary optics	83
B.1.1	Introduction and theoretical considerations	83
B.1.2	Measurements and Results	84
B.1.3	Conclusion and Outlook	92
	Bibliography	93
	Acknowledgments	103
	Curriculum vitae	105
	Lebenslauf	107

1 Introduction and motivation

Proton induced X-ray emission (PIXE) is a well established non destructive material analysis method for a wide range of different elements. It is considered to be quite accurate at determining matrix element compositions. Nevertheless a lot of samples, especially art objects, are inhomogeneous or show a layered structure. In such cases typical PIXE is not able to resolve the structure. If the distribution of elements are located near the surface additional analysis methods, such as Rutherford Back-Scattering (RBS), can be used to discern inhomogeneity. Another method available is differential PIXE analysis, which is for example used for analyzing precious objects [7]. The penetration-depth of protons into a target changes depending on their energy. In differential PIXE this energy dependence is used to get information from different depths. As a consequence a continuously new tuning of a great deal of the facility which provides the protons, for each individual energy considered, is necessary.

In the year 2003 depth-resolved X-ray fluorescence spectroscopy was introduced by Kanngießer et al. [18]. With the intersection of the focused incident X-ray beam with a focused detection channel a confocal probing volume was formed. By moving the samples through this volume, information about depth could be analyzed. This idea was adapted recently so that it could be used when performing PIXE measurements [19]. Polycapillary-structures permit a focused detection channel to be achieved. These glass-optics are optimized for guiding X-rays by means of external total reflection and were developed about twenty years ago at the Kurchatov Institute, Moscow [21].

The principal aim of this thesis was to establish depth resolved PIXE analysis at the Vienna Environmental Research Accelerator. This could be achieved in collaboration with Prof. Birgit Kanngießer from the TU Berlin and with the Institute of Scientific Instruments, ifg in Berlin. The feature was added to the external PIXE-ART facility (installed in the year 2004 [20]). An improvement of the original device was also part of this work. The motivation originates in the better overall material analysis of precious art objects with information in depth as well as better spatial resolution in the sample plane.

Furthermore investigations about different polycapillary-optics were carried out. Three different types, in particular a half-lens, a lens and a conic-collimator structure were characterized to gain more knowledge of properties and handling with those capillaries.

In addition, to get information about the accuracy and the present state of the PIXE-ART setup at VERA, samples provided by the Academy of Fine Arts in Vienna were analyzed by means of their elemental composition. The samples are selected coins from the time of the Roman Cesar Traian and from the period of the Ottoman Sultans Murad III and Mehmed III. Furthermore iridescent Art Nouveau glasses from Tiffany and Loetz have been studied. These measurements conduce additional results for answering historical and art historical questions as well as a comparison of the PIXE-ART setup at VERA with other PIXE facilities and other material analysis methods respectively.

2 Theoretical considerations

2.1 PIXE

PIXE is a well-established nondestructive technique for quantitative material element analysis. It was introduced at the Lund Institute of Technology in 1970 [15]. Protons show the most advantages in the possible projectiles of charged particles. First, they produce a significant less amount of Bremsstrahlung than electrons. Theoretical it is inverse proportional to the square of mass and the expected background for protons should be marginal. But, taking the secondary electrons produced during the scattering process of the proton (projectile) in the target material into account, a background could be detected. Furthermore, the advantage of protons compared to heavier ions, is the deeper penetration into the target material (see section Protons in matter). Johansson and Campbell [13] presented very early a short summary of the advantageous properties of PIXE element analysis:

- simultaneous analysis of many elements in a very wide region of Z (see figure 2.8)
- sensitive method for trace element analysis, detection limits in the ppm region
- short detection time (only several minutes)
- possibility of external in air analysis (see section External PIXE)

2.1.1 External PIXE

The possibility of performing investigations with an external proton beam is very comfortable and the the only way for analysis of art objects. A brief summary of advantages of in air set-ups is given by Calligaro et al. [4]:

- it allows the analysis of items of any size and shape
- it avoids the alteration due to vacuum (dehydration, outgassing, etc.)
- it reduces the risk of heating and beam-induced damages
- it eliminates the need of sample preparation such as the deposit of conductive coating
- it improves system efficiency by simplifying sample positioning and changing

2.1.2 Principle of PIXE, Moseley's Law

The basic principal of PIXE is to produce characteristic X-rays, which are unique in their energy for each element. For inducing these X-rays, charged particles (protons) bombarding the target ionize the atoms due to Coulomb-interaction. The protons produce inner shell holes in the specimens atoms. An electron from an outer shell will fall into this inner shell vacancy (see figure 2.1). Within 10^{-16} s the excited atom will de-excite to its ground state by sending out an photon with a certain energy value or alternatively an electron, the so called Auger electron (see section 2.1.3 Fluorescence yield, Auger process). The emitted X-ray energy equals the difference of the binding energies of the inner shell with the unoccupied place and the filled outer shell.

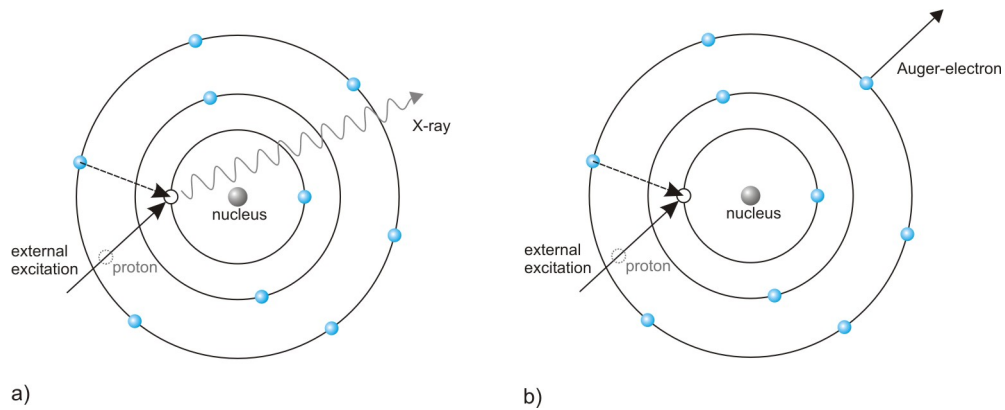


Figure 2.1: a) Sketch of characteristic X-ray production incident. b) De-excitation through Auger electron emission.

Is the hole in the innermost shell, the K-shell ($n=1$), filled by an electron from the next higher shell, L-shell ($n=2$), the transition is called $K\alpha$. A scheme for the notations of characteristic X-rays is given in figure 2.2. The selection rules for allowed transitions are:

$$\Delta n \geq 1, \Delta l = \pm 1, \Delta j = 0, \pm 1$$

In 1913 Moseley discovered the experimental relation between the atomic number Z of an element and the frequency of the characteristic emitted X-ray. By using Braggs Law of diffraction in a crystal, $n\lambda = 2d\sin\theta$, he could determine the energy of the produced X-ray. Moseley's Law for K-lines is shown in formula 2.1 where 13.6 eV is the ionization energy of a hydrogen atom, Z is the atomic number, the 1^2 in the fraction $\frac{1}{1^2}$ indicates that the lower energy level with the hole is the K-shell, m represents the level of the higher state the falling electron originated from, e.g., $m = 2, 3, \dots$ and the 1.0 in the factor $(Z-1.0)$ is called the shielding constant and defines the shielding of the core charge through other electrons. This number is specific for

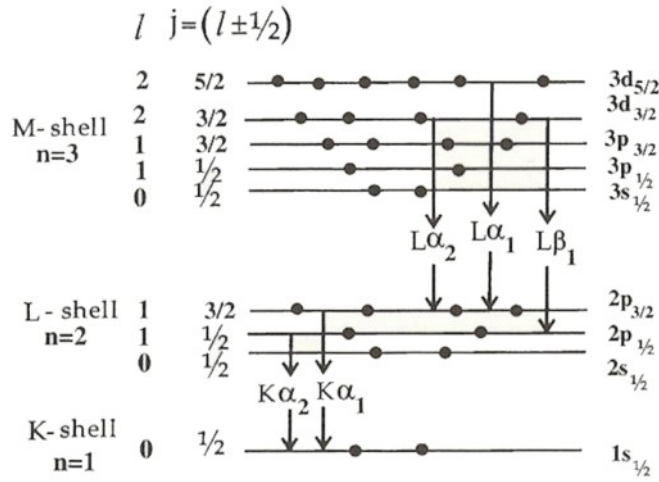


Figure 2.2: Notation of characteristic X-ray transitions including related energy levels, quantum numbers and electron occupation, [38].

each series of lines. For L-lines it is ≈ 7.4 . The de-excitation energies are in the order of keV.

$$E_K \cong 13.6 \text{ eV} \cdot (Z - 1.0)^2 \cdot \left(\frac{1}{1^2} - \frac{1}{m^2} \right) \quad (2.1)$$

A detailed set of X-ray emission energies for each element are given from Jeffrey B. Kortright and Albert C. Thompson in the X-Ray Data Booklet [35], which is used as reference in this work.

2.1.3 Fluorescence yield, Auger process

As already mentioned in the section before there are two main possibilities of the de-excitation procedure. First there is the X-ray emission, which probability is described by the fluorescence yield ω_Z (see approximation formula from Burhop 2.2). The competitive process, which is greater for lighter atoms, is the release of an so called Auger electron (see figure 2.1). In this case the selection rules are not applied. Hence the kinetic energy of the emitted Auger electron only depends on the energy level of the original vacant state, the initial level of the electron, which fills the vacancy and the initial level of the Auger electron.

$$\omega_Z = \frac{1}{1 + cZ^{-4}} \quad c(K) \dots 1.2 \cdot 10^6 \quad C(L) \dots 6.4 \cdot 10^7 \quad (2.2)$$

Figure 2.3 shows the dependence of the fluorescence yield of the atomic number Z . It shows, compared to the ionization cross section, which we will see in the next section, an opposite behavior with increasing Z . The fluorescence yield increases with the atomic number and is greater for K-shell holes. The total cross section for producing X-ray through proton bombarding consists of the product between the fluorescence yield and the ionization cross section.

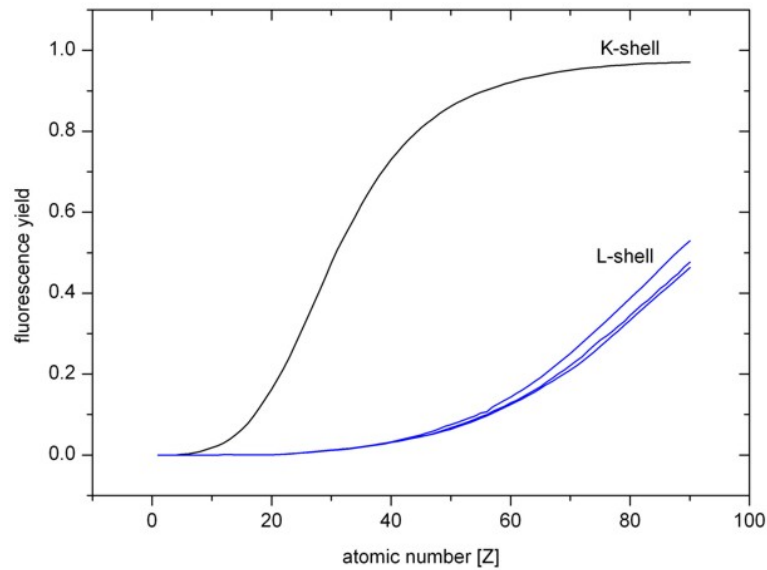


Figure 2.3: Fluorescence yield as a function of the atomic number Z .

2.1.4 Ionization cross section

The cross-section σ_i for the ionization of an inner shell, referring to a certain target atom, increases with the injection energy of the projectile and reaches a maximum when the projectile velocity and the velocity of the electron in this specific shell are of the same order. Thus, σ_i is greater for L-shell hole production. Figure 2.4 shows the ionization cross-section for different elements depending on the energy.

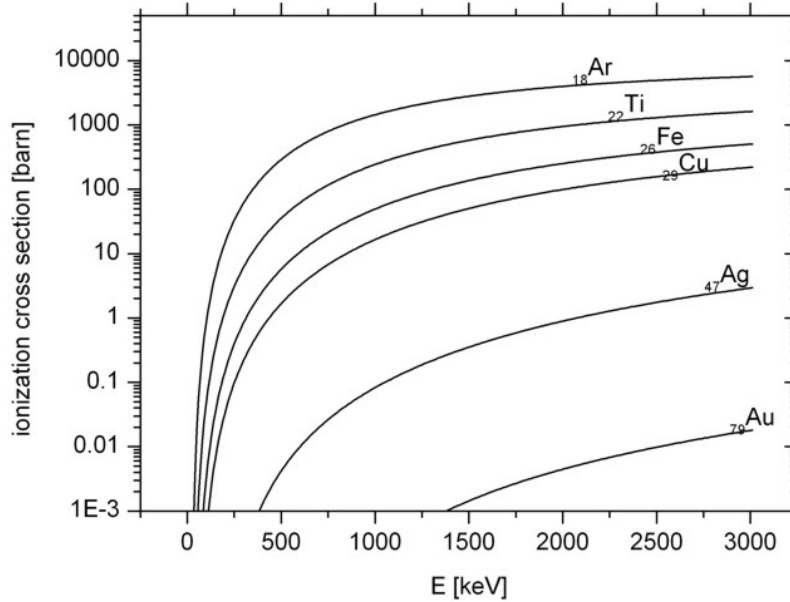


Figure 2.4: Ionization cross section through proton bombarding for different elements (data taken from VIBA-LAB [28]).

2.1.5 Protons in matter

When protons enter matter they lose energy due to ionization by collision with the target atoms. The Stopping Power (see formula 2.3) depends on material and density of the specimen and on the velocity of the incident protons. The energy loss $\frac{dE}{dx}$ was described approximately by Bethe and Bloch and is shown in formula 2.4 where E_1 , Z_1 , and v_1 is the energy, atomic number and velocity of the projectile respectively, Z_2 the atomic number of the target and J the mean excitation potential of the target. The energy loss of protons shows the highest value shortly before stopping completely. This kind of profile is called a Bragg curve.

$$S(E) = \rho^{-1} \frac{dE}{dx} \quad (2.3)$$

$$-\frac{dE}{dx} = \frac{4\pi Z_1^2 e^4}{m_e v_1^2 (4\pi\epsilon_0)^2} \cdot Z_2 \cdot \ln\left(\frac{2m_e v_1^2}{J}\right) \quad (2.4)$$

The relatively short stopping path of protons (even shorter for helium or alpha particles) in matter is especially for external PIXE a limitation in terms of analyzing

thick samples. Figure 2.5 shows the range for 3 MeV protons in air and in an specimen of iron.

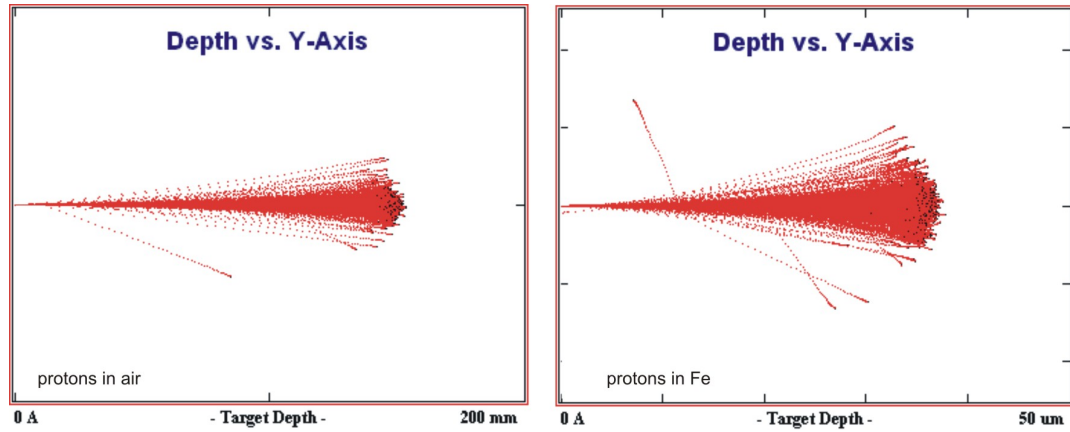


Figure 2.5: Penetration depth and angular distribution due to scattering processes of protons in air and Fe.

2.1.6 X-rays in matter

Not only the charged particle sustain loss while entering the target material. The produced characteristic X-rays have to go all the way through the target from the place they were produced to reach the detector. Electromagnetic-rays suffer from intensity loss going through matter due to photo effect, Compton effect and pair production. In the energy range of characteristic X-rays only the cross-section of the photo effect is sufficiently high. It shows the greatest cross-section in the several keV energy range. To describe that loss, the mass attenuation coefficient is used and can be calculated with the exponential attenuation law (formula 2.5), where I and I_0 are the intensities after penetrating through a material and the initial intensity, respectively. ρ and x represent the density and mass thickness (thickness multiplied with the density) of the sample and μ is the attenuation coefficient itself given in cm^{-1} , which is different for each element and compound.

$$I/I_0 = e^{-(\mu/\rho)x} \quad (2.5)$$

An example for the energy dependence of the mass attenuation coefficient is shown for iron in figure 2.6.

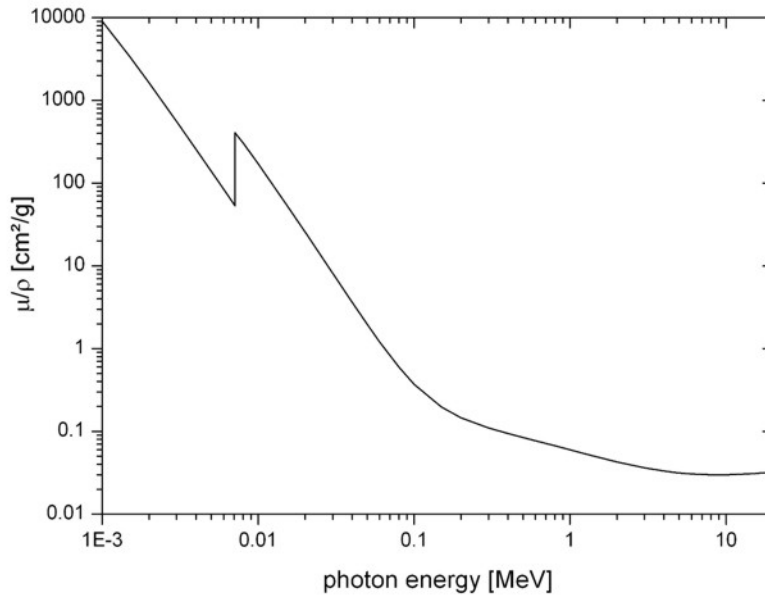


Figure 2.6: X-ray mass attenuation coefficient for element Fe, data taken from NIST, Physical Reference Data. At ≈ 8 keV the ionization edge for the iron K-shell is visible.

2.1.7 X-ray detection

The physics of detecting X-rays is very similar to the one in the section before, but here the complete absorption of the photons is the preferred situation. Again photo effect is the mechanism to collect the energy of the photons and produce an electrical signal. The commonly used detectors for X-ray analysis are semi-conductor-crystals e.g. Si ($Z=14$). The number of produced electron-hole pairs in the crystal represent the energy of the measured X-ray. Both, electrons and holes, are used for producing the electronic signal, which is then converted into a digital signal after a impulse processing procedure, containing a preamplifier, an amplifier and a Multi-Channel-Analyzer. A high voltage has to be applied at the detector crystal for good charge separation. The typical output is an energy dispersive spectrum (e.g. figure 3.7).

The line shape of a detected peak is approximately Gaussian. But for an exact description of an element specific X-ray line the non Gaussian components of the peak have to be considered [8]. If not, there is a possibility that fitting codes interpret these effects as small concentration of another element. Figure 2.7 shows a sketch of all individual components. In addition to the Gaussian (G) peak a shelf (S) reaching almost zero is caused through losses of photo-electrons produced near the surface of the detector crystal and loss of silicon K Auger electrons respectively. Due

to the near surface absorption of low energies this effects increase with lower X-Ray energy. The second small shelf (ST) refers to escapes of thermal induced ionization electrons due to diffusion out of the surface. Moreover the main Gaussian shaped component is a convolution of a Lorentzian and a Gauss distribution and therefore a Voigt function. The Lorentzian curve is the natural line shape of a characteristic X-ray. The second smaller peak in the line-shape plot is the so called Si-escape peak. It originates from the loss of a characteristic Si $K\alpha$. Hence the energy of the main peak is reduced by 1.739 keV and therefore shifted to the left in the energy dispersive spectra. This phenomenon also occurs only if the X-ray is generated close to the crystal surface.

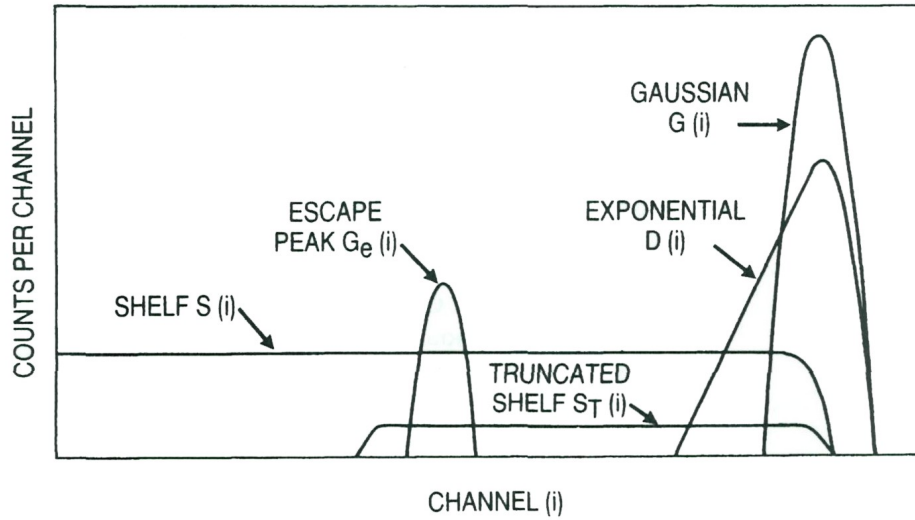


Figure 2.7: Components of line-shape of a typical Si(Li) detector spectra, [14].

2.1.8 X-ray yield

The area of a peak is directly related to the concentration of the corresponding material. For quantitative analysis of element concentrations the yield of all included processes, also the detection itself, has to be calculated. A very good overview of this topic for thick and thin specimen analysis is given in [14]. In the present work only the general equation for K shell X-rays is presented in formula 2.6 for the yield and in formula 2.7 for the transmission factor, respectively.

$$Y(Z) = \frac{N_{Av}\omega_{K,Z}b_{K,Z}t_{K,Z}\epsilon_Z^i(\Omega/4\pi)}{A_Z} \cdot N_p \cdot C_Z \cdot \int_{E_0}^{E_f} \frac{\sigma_Z(E)T_Z(E)}{S_M(E)} dE \quad (2.6)$$

$$T_Z(E) = \exp \left[- \left(\frac{\mu}{\rho} \right)_{Z,M} \frac{\cos \alpha}{\sin \theta} \int_{E_0}^E \frac{dE}{S_M(E)} \right] \quad (2.7)$$

N_{Av} denotes the Avogadro's number, $\omega_{K,Z}$ the fluorescence yield, $b_{K,Z}$ the line intensity fraction, $t_{K,Z}$ the transmission through all absorbers between detector and sample, ϵ_Z^i the detector efficiency (see also chapter Verification of quantities GUPIX), $(\Omega/4\pi)$ the solid angle "seen" by the detector, A_Z the atomic mass of the target material, N_p the number of incident protons, C_Z the concentration, E_0 and E_f are the initial and final proton energy, $\sigma_Z(E)$ the K-shell ionization cross section and $S(E)$ the stopping power for a certain proton energy according to penetration depth. The footnote Z indicates the atomic number of the used material in each case, K the K-shell and M the matrix elements (main elements in the specimen). The transmission factor $T_Z(E)$ describes the loss in intensity of the X-ray on the way to the detector with α and θ as the angles between incident beam and the perpendicular to the sample surface and detector and sample surface respectively. Figure 2.8 shows limits of detectable concentrations depending on the atomic number for PIXE analysis.

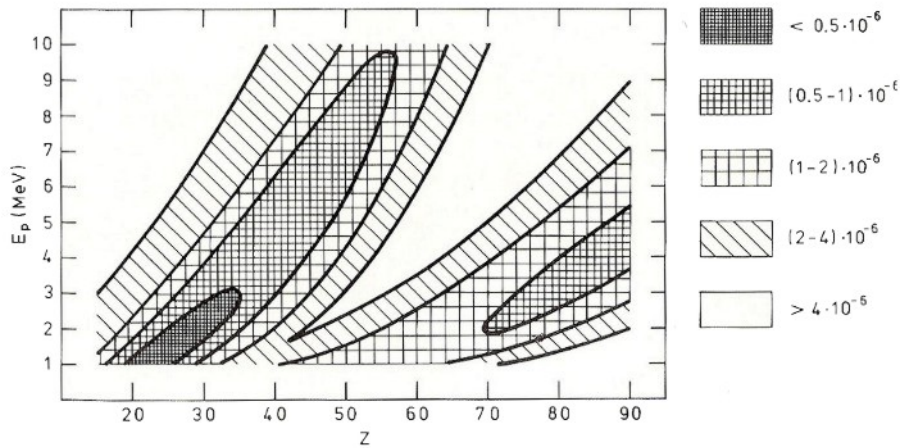


Figure 2.8: Ranges and minimum detectable concentrations of elements as a function of atomic number and proton energy for organic specimens [13].

2.2 Polycapillary X-ray optics

One of the main studies in this work is the investigation of polycapillary X-ray optics and to perform depth resolved PIXE-analysis. These capillaries are used for guiding the X-rays, produced in the target, to the detector in the way similar to converging lenses. The detection volume is represented through the intersection of the external proton-beam and the focal "tube" of the polycapillary, which is inserted in the detection channel (see figure 2.9). By moving a target through that volume, information in depth can be derived. The use of a defined detection volume, also called probing volume, was introduced in combination with X-ray fluorescence analysis (XRF) at the TU Berlin [18]. In this case a confocal volume was formed by inserting a capillary optic in detection channel as well as in the excitation channel [24].

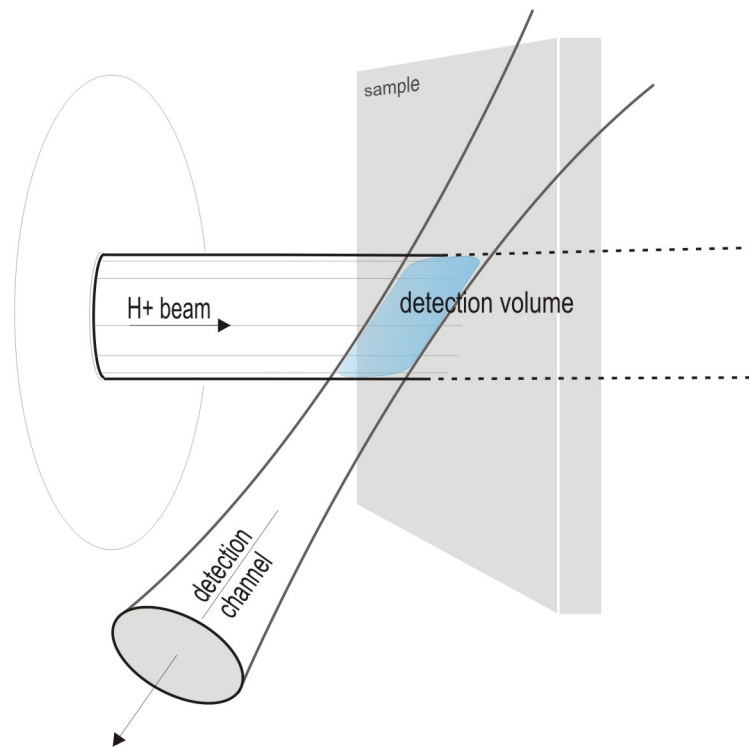


Figure 2.9: Intersection of excitation channel and detection channel.

There are different types of polycapillary optics. First it can be manufactured similar to a biconvex lens and therefore it shows on both sides, inlet and outlet, focus points (Polycap.-lens). The second type is a half lens with only one focus point (Polycap.-half-lens). The third investigated type in this work is a so called polycapillary conic collimator (Poly-CCC). All three types, were used for quantification measurements and comparison (see section 4.1 Characterization of polycapillaries).

The three different types are shown in the sketch of figure 2.10. The dimensions of the capillaries used in the experimental part are listed in table 2.1.

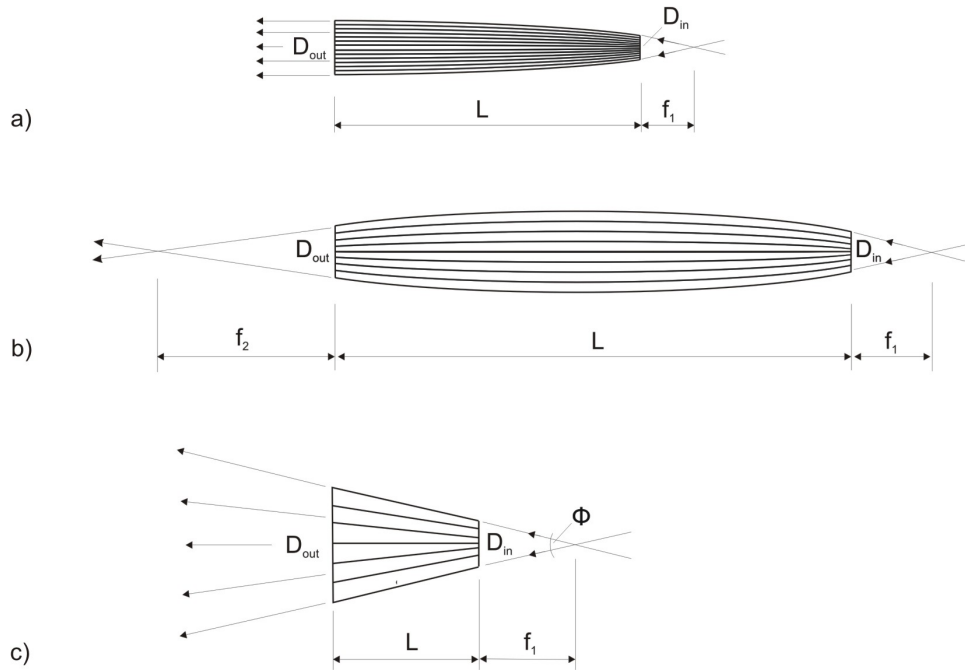


Figure 2.10: Sketches of Polycapillaries: a) half-lens b) lens c) Poly-CCC

	22mkl 06	73mls 08	71mls PCCC14
	semilens	lens	Poly-CCC
L, length [mm]	22.8	82.4	15.7
D_{in} , entrance diameter [mm]	1.8	5.7	3.15
D_{out} , exit diameter [mm]	2.7	6.9	6.9
f_1 , entrance focal length [mm]	6.6 ± 0.1	59 ± 1	8.7
f_2 , exit focal length [mm]	-	101 ± 0.1	-
ϕ , capture angle [°]	-	-	19.9

Table 2.1: Dimensions of polycapillaries

2.2.1 Properties of polycapillary x-ray optics

In general a polycapillary lens consist of up to several millions very small hollow channels (glass capillaries, see figure 2.12). They are bent in such a way, that the divergent X-rays collected in a focus area are guided to form a quasi-parallel beam in the case of a half-lens, a second focal point if it is a full lens, when leaving the polycapillary. In the case of the Poly-CCC the divergence is restricted to a certain capture angle. To guide the X-rays through these thin capillaries external total reflection is utilized [5], [37]. Electromagnetic waves change their phase velocity when going from one material into a different one. If the incidence angle differs from the perpendicular at the interface also the propagation direction changes. This is described with the law of refraction of Snellius 2.8 (see also figure 2.11):

$$n \cdot \sin\alpha = n' \cdot \sin\alpha' \quad (2.8)$$

With n and n' being the index of refraction in the first and the second material respectively, as well as α and α' the incident and the refracted angle respectively.

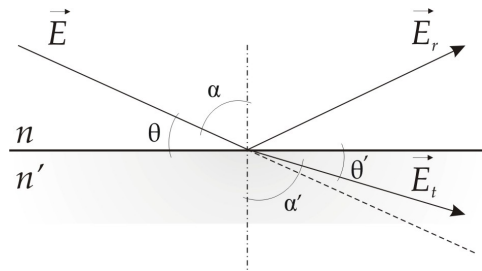


Figure 2.11: Sketch referring to the law of Snellius, the transition of electromagnetic waves from one material into another.

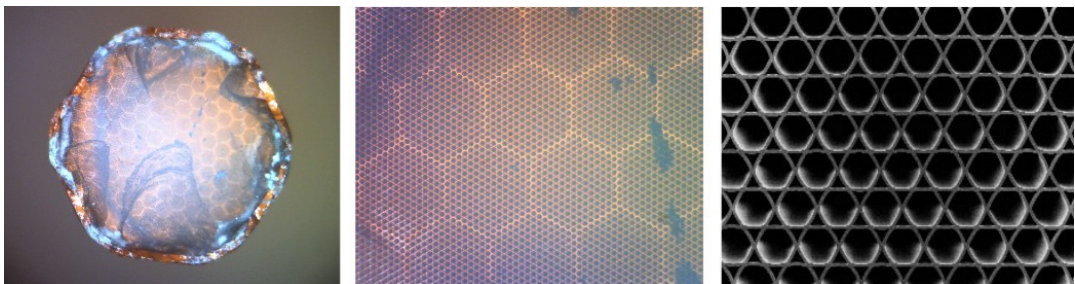


Figure 2.12: Structure of glass polycapillaries, the diameter of the hollow channel is in the order of some $10\mu\text{m}$. Fig. left and middle: Polycap. lens 73mls 08, Fig. right: closer look at structure - ifg Berlin [30]

When the incoming ray goes from the optically denser material into the thinner one a critical angle θ_c exists. At this angle the refraction angle θ' equals zero. The refracted light follows the interface of the two materials. If the entrance angle is even smaller than θ_c , θ' cannot be real and the beam of light is totally reflected (2.9).

$$\theta_c = \arccos(n'/n) \rightarrow \theta' = 0 \quad (2.9)$$

In contrast to visible light the real part of the refraction index n (2.10) for X-rays in matter is less than 1. Hence, total reflection occurs from air or vacuum into solid matter.

$$n = 1 - \delta - i\beta \quad (2.10)$$

β (2.11) describes the absorption in the medium and δ (2.12) the change of the phase velocity [6].

$$\beta = \frac{\lambda}{4\pi} \mu \quad (2.11)$$

$$\delta = 2.7 \cdot 10^{-6} \frac{Z \cdot \rho_{[g/cm^3]}}{A} \lambda_{[\text{\AA}]}^2 \quad (2.12)$$

- λ ...wavelength
- μ ...linear absorption coefficient in a medium
- Z ...atomic number
- A ...nuclear number

Because of the small values for δ , θ_c approximately follows equation (2.13).

$$\theta_{c[rad]} \cong \sqrt{2\delta} \quad (2.13)$$

The angle of total reflection depends on the wavelength of the incoming X-rays and is therefore inversely proportional to the energy. Formula 2.14 gives that property for a quartz crystal as a reflector material. Moreover, also the focal spot size of the polycapillary will change with the incoming X-ray energy. Consequently the volume from where the X-rays are collected varies in size. This leads to different FWHM for different elements. Therefore elements with a higher Z show a slightly smaller FWHM because of their higher characteristic X-ray emission energy. Furthermore

this inverse proportional dependence on photon energy and on critical angle results in suppression of high energy X-rays.

$$\theta_{c[mrad]} \cong \frac{32.2}{E_{[keV]}} \quad (2.14)$$

2.2.2 Transmission through glass capillaries

However total external reflection may be accompanied with absorption. In order to fully describe the transmission probabilities of X-rays through polycapillary glass structures several phenomenons have to be taken into consideration. First of all with every hit of the X-rays with the surface of the capillary a certain amount of intensity will be lost. The processes can be calculated with the formulas of Fresnel. The assumption of a homogeneous medium is fulfilled because of the small penetration of the X-rays into the material [29]. Principally also the roughness of the reflector surface has to be considered. But those changes in intensity are negligible if we assume that the micro roughness of glass-capillaries is also in the order of some Å and the wave length of the reflected X-rays are also in the order of atomic structures. Still, they penetrate to a certain depth into the material. For small angles (measured from the critical angle) the penetration depth is approximately energy independent and reaches a limiting value z (see formula 2.15). The limit is in the order of some nm.

$$z = \sqrt{\frac{m_e c^2}{8\pi n_e e^2}} \sqrt{\frac{1}{\sqrt{1 + (\beta/\delta)^2} + 1}} \cong \sqrt{\frac{m_e c^2}{16\pi n_e e^2}} \quad (2.15)$$

m_e is the mass of an electron and n_e the electron density of the reflector material.

With $n_1 = 1$ for air and $n_2 = 1 - \delta - i\beta$ for the dense material and the intensity of the reflected part I_r of the beam relative to the incoming I_0 , i.e. the reflectivity $R(\theta)$ follows from Fresnel theory 2.16 [9]:

$$R(\theta) = \left(\frac{I_r}{I_0}\right) = \frac{\rho^2(\sin\theta - \rho)^2 + \beta^2}{\rho^2(\sin\theta + \rho)^2 + \beta^2} \quad (2.16)$$

$$\rho^2 = \frac{1}{2} (\sqrt{(\sin^2\theta - 2\delta)^2 + 4\beta^2} + (\sin^2\theta - 2\delta))$$

If no absorption in the reflector material would occur the expected reflectivity for smaller angles than the critical one would equal 1 over the whole range. Figure 2.13 shows the reflectivity dependent on the incident angle for SiO_2 . Dependent on the ratio β/δ the change at the critical angle is more or less sharply defined. The bigger

β/δ , that means the bigger the absorption, the more flat the curve becomes. Furthermore the reflectivity is strongly dependent on the atomic number of the reflector material. At the absorption edges strong suppression of the intensity occurs.

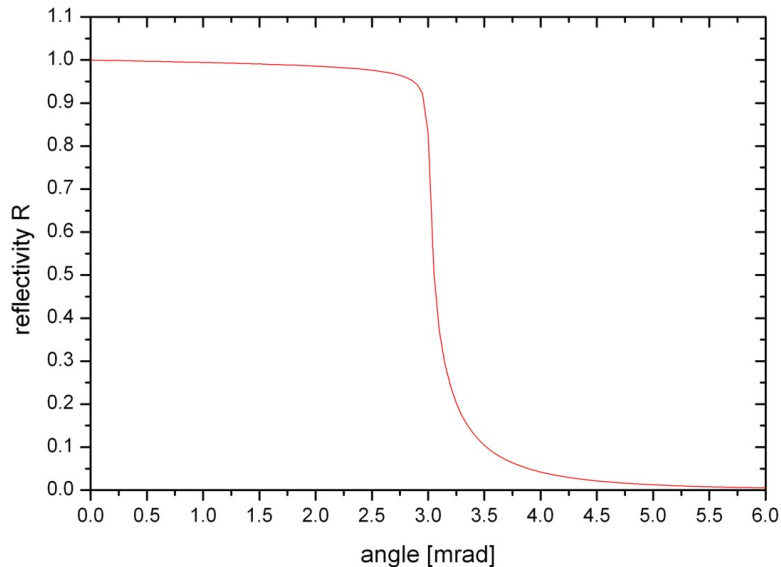


Figure 2.13: Reflectivity of 10keV X-Rays with SiO_2 as reflector material.

The second aspect, that has to be considered to understand transmission properties, is the way of the rays through the capillaries [27]. For a single capillary within a bent polycapillary, one wall is convex the other is concave. There are two possibilities for X-rays to get through. First the rays hit the wall, get reflected and strike the opposite wall and so on until reaching the outlet of the capillary. Due to oscillation of the reflection angle θ , it decreases and increases in the consecutive strokes, each reflection is still relatively efficient. Also the final divergence of the beam at the exit side is small. A second case of a trajectory through a capillary is the so called whispering gallery mode. Here the incident angle is that small that the X-rays are reflected only at the concave wall. Because of that the possibility of reaching angles above the critical angle is low and also the reflection coefficient is big. A disadvantage of this mode is the great number of hits needed to go through.

Poly-CCC are a special case. Due to the straight channels no whispering gallery mode is possible. When used in the correct orientation i.e. the smaller opening towards the source, the conical shape of individual capillaries decreases consecutive reflection angles. This makes Poly-CCC most efficient in terms of transmission.

2.2.3 Comparison and features of polycapillary types

Polycapillaries are mainly used to overcome the limits of regular collimators. Due to the great acceptance angle polycapillaries may provide intensity gains of several hundred percent when compared to collimators with the same spatial resolution. This is particularly useful in the detection channel of ion beam analysis and X-ray fluorescence analysis when the sample does not allow for high irradiation doses. In the following the main types are compared again with respect to the detection side.

Polycapillary conic collimator, Poly-CCC

The system only collects rays with incidence angles relative to the channel axis smaller than the critical angle of total reflection. The spatial resolution of such capillaries follows a simple formula [3] (2.17):

$$D = 2\varphi_c f \tag{2.17}$$

where D is the spatial resolution in one dimension (diameter of the spot), φ_c the critical angle of total reflection and f the focal distance of the system. As a consequence the focal distance and the spatial resolution are direct proportional and a shorter focal length provides a smaller detection area.

Poly-CCC are limited in their useful length because it makes no sense when the exit side of the Poly-CCC exceeds the area of the detector crystal. Therefore, the acceptance angle is also restricted. A particular advantage is the high transmission due to the low number of necessary reflections (see before). A disadvantage is the loss of spatial resolution for high energetic X-rays [17]. High energetic X-rays (more than 17keV) have the possibility to pass through the walls of the capillaries without being totally reflected. Due to the lower linear absorption coefficient for higher energies, longer structures would be necessary to cut off properly the unfocused X-rays.

Polycapillary lens and half-lens

The feature of lens and half-lens structures is their ability of X-ray focusing. These capillaries are good for small crystal detection areas. A big disadvantage is the low transmission of those structures due to the large number of reflections required to follow the bending of the channels. This is especially the case for the type of a lens with two focal spots. It should also be mentioned that the maximum bending is limited for technical reasons. So, there is always a tradeoff between spatial resolution, transmission and detector size.

2.2.4 Summary of properties

Polycapillary X-ray optics show the following advantages and disadvantages being used in the detection channel for X-rays analysis (see also [1]):

- Restricted detection volume offers the possibility of depth resolved analysis.
- Due to the behavior of the critical angle of total reflection, lighter elements are favored as well as high Z-elements where L X-rays are in a similar energy range.
- The angular divergence of X-rays at the exit is in the order of several mrad.
- Protons cannot penetrate through polycapillary optics (see also section 2.1.5 Protons in matter and quantitative considerations in Appendix B). Therefore no additional filter in front of the detector is necessary.
- Absorption of X-rays in every reflection leads to bad transmission.

3 Experimental setup

The experiment was carried out at the Vienna Environmental Research accelerator, VERA. Some years ago a beam-line for performing external PIXE was installed within the work of [20], [26]. It is now improved and combined with other analysis methods like PIGE (Proton Induced Gamma Emission) and RBS (Rutherford Back Scattering). In the following sections a brief overview of the accelerator VERA is given and the experimental setup for the present work is described in detail.

3.1 The accelerator of VERA

The accelerator VERA is a 3MV Pelletron Tandem accelerator primarily installed for AMS (Accelerator Mass Spectrometry). It was built by National Electrostatics Corporation (NEC) in Wisconsin, USA and since the year 1996 it is operational at Vienna [22], [31]. Figure 3.1 shows the sketch of the actual accelerator facility. For PIXE purposes the cesium-beam sputter source runs with TiH_2 cathodes for producing negatively charged hydrogen ions. (note: A second sputter source was installed at VERA, which was also tested and successfully used for PIXE purposes. A mixture 1:2 of HfH_2 with Ag-powder was used there as cathode material.) The energy of the ions at the low energy side of the facility equals $E_{inj}=70\text{keV}$ (see formula 3.1).

$$E_{inj} = q \cdot U_{ex} = q \cdot (U_{cathode} + U_{extraction} + U_{source\ high\ voltage}) \quad (3.1)$$

q...charge, U...voltage

The first 45° Electrostatic Analyzer (ESA) selects the particles in accordance to the adjusted voltage (see formula 3.2).

$$U = \frac{2E \cdot d}{q \cdot \rho} \quad (3.2)$$

d...distance of ESA plates, ρ ...bending radius

U...voltage between both plates, E...energy of particles

Before entering the accelerator the beam is bent with a 90° Analyzing Magnet, called BM 01-1, (beam selection formula see 3.3)

$$B = \frac{\sqrt{2ME}}{q\rho} \quad (3.3)$$

B...magnetic field, M...atomic mass

The Tandem Accelerator utilizes one high voltage terminal two times. The applied high voltage for the proton beam in this work is 1.5 MV. The first cascade of ring electrodes accelerates the negatively charged particles to about 1.5 MeV and, after stripping two electrons another 1.5 MeV are added through the second drift segment.

Another analyzing magnet BM-03, an ESA and diverse focusing components lead the beam into the the beam switching magnet, which selects the -20° beam-line towards the PIXE-ART station (see figure 3.1, PIXE-Art label). Within this beam-line a horizontal and a vertical slit with an opening of 0.5 mm are situated. They are used for pre-collimating the proton-beam 48 cm before the exit into air to reduce background rays (γ -rays from nuclear reactions) originating from collision of the beam with construction material.

The various steerers, lenses, beam profile monitors, etc. are required for tuning, but are not described explicitly here.

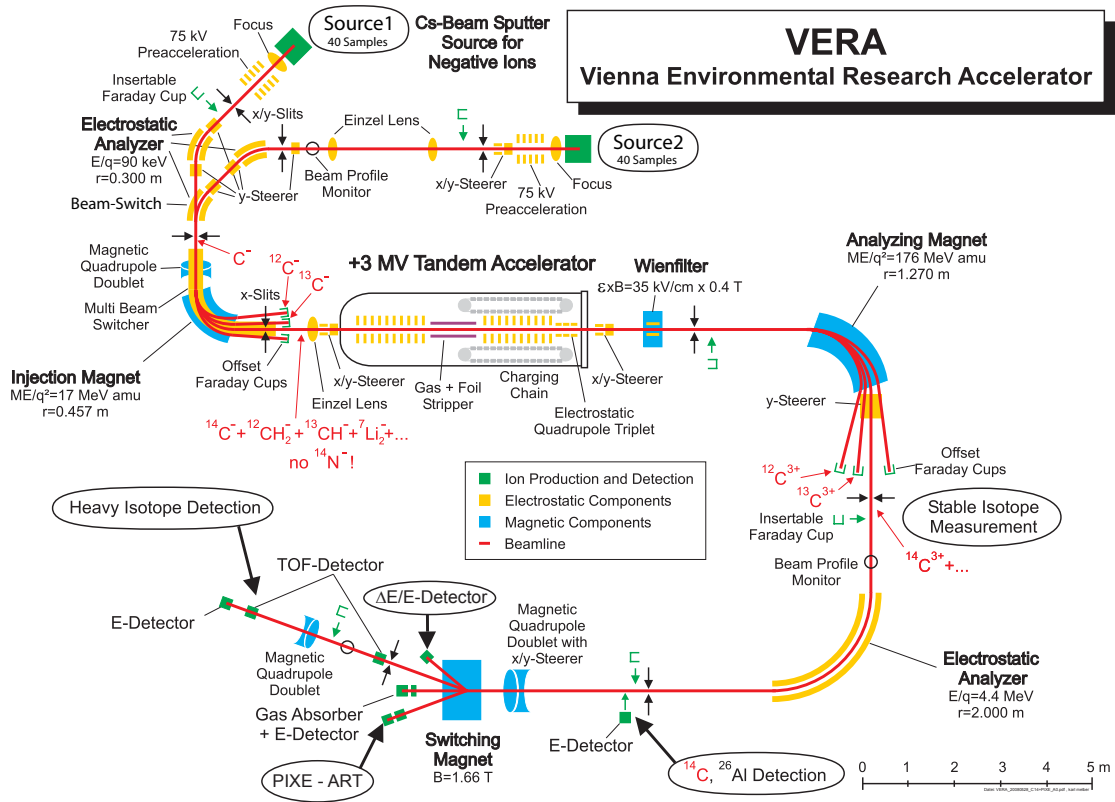


Figure 3.1: Scheme of the Vienna Environmental Research Accelerator VERA.

3.1.1 Beam trajectory simulations

Because of difficulties with position instabilities of the proton beam at the PIXE-ART station a simulation of the ray-trajectories for different energies was carried out together with Martin Martschini utilizing the COSY-code (see figure 3.2 and 3.3). Due to small fluctuations of $\Delta E/E \approx 3 \cdot 10^{-4}$ of the terminal voltage the energy is not stable. Of greatest interest was to find the location of the achromatic point (same position for different energies) of the system. Usually it is situated before the switching magnet and even before the Quadrupol Dublet MQ-L4. Utilizing the Wienfilter the achromatic point should be moved behind the switcher magnet to establish more spatial stability of the beam. Unfortunately the maximum value of the magnetic field produced by the Wienfilter is lower ($B_{max} \cong 0.15 T$) than the 0.5 T that would be necessary. Practically with a field that strong in the Wienfilter the rays of only a sleightly diffrent energy would hit the walls of the bending elements.

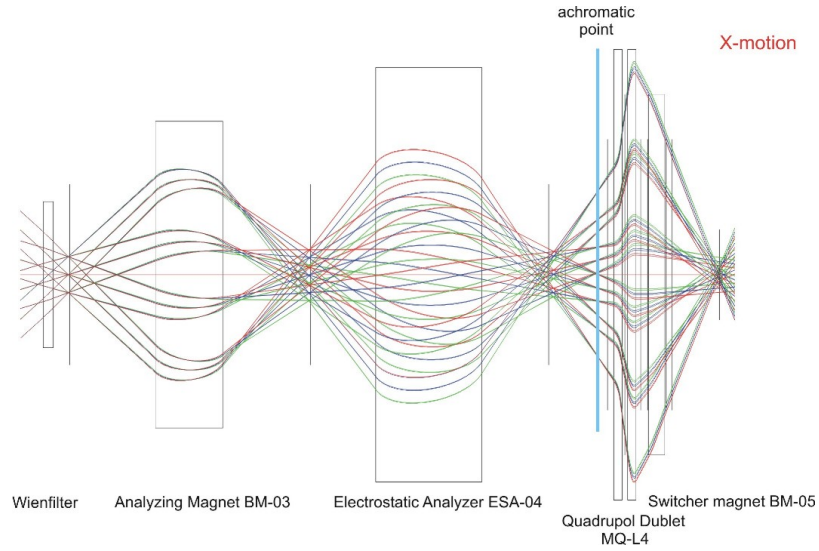


Figure 3.2: Side view of the beam trajectories (without use of the Wienfilter) through the bending units starting from the accelerator exit.

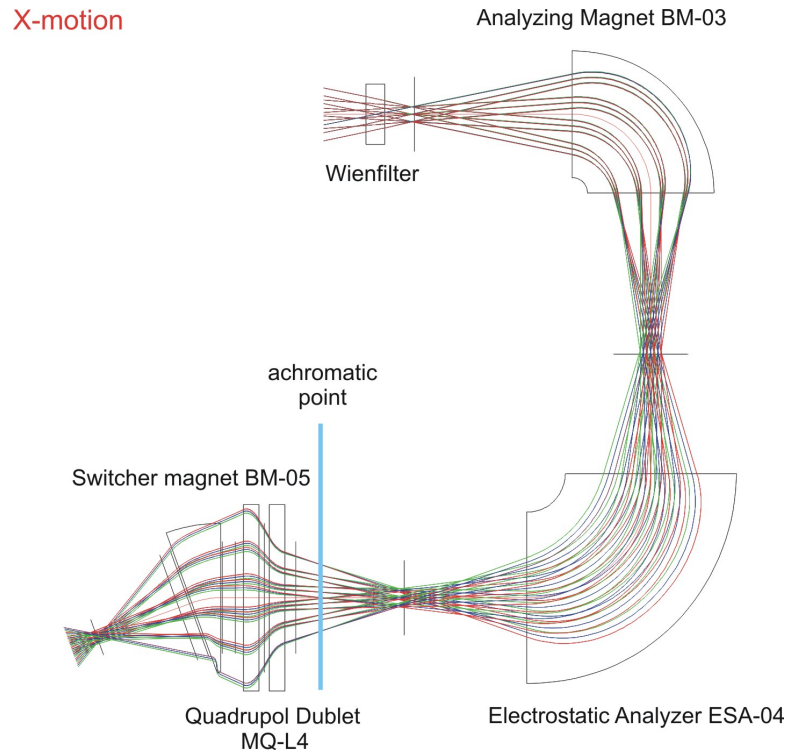


Figure 3.3: Top view of the beam trajectories (without use of the Wienfilter), the achromatic point is located shortly before the Quadrupols.

3.2 The PIXE assembly at VERA

The main parts of the measuring setup are the exit for the protons out of the vacuum system into air and the detection assembly. An overview of the equipment is shown in picture 3.4.

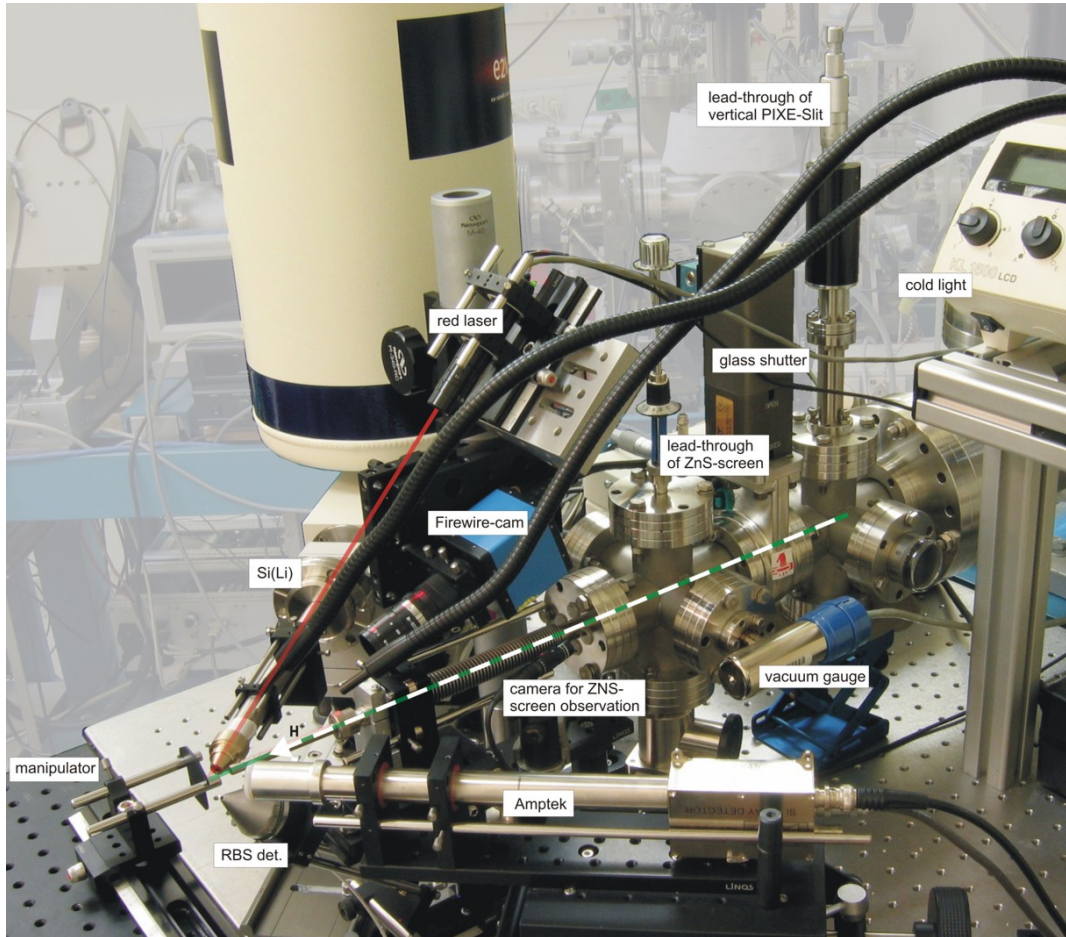


Figure 3.4: PIXE setup at VERA.

After guiding the beam via the switcher magnet into the PIXE-beam-line, the goal is to focus the beam at the exit window. This can be achieved with two steerers and the quadrupole doublet right in front of the switcher magnet. A movable ZnS-screen in the beam line short after the PIXE-slits is used for tuning procedures. Due to its fluorescence with high energy protons the beam can be visualized. The beam of protons gets collimated twice. First at the PIXE-slits mentioned before to half a millimeter square. After entering the nozzle (10 cm total length, 6 mm in diameter) a second collimator made from carbon with a hole of 150 μm restricts the beam to

its final dimensions. The exit window is a 100 nm thick Si_3N_4 window glued on to the carbon collimator. It is thin enough to not deteriorate the protons in energy too much. On the other hand it is thick enough to create a barrier between atmospheric pressure and the vacuum in the beam-line, which is in the order of 10^{-4} mbar.

To define the exact point where the proton beam is hitting the target a green laser beam is going collinear with the protons through the vacuum tube of the PIXE beam-line, exits the nozzle and produces a spot at the external target. At a position of exactly 1 cm in front of the nozzle exit window the green laser crosses with a red laser (cross shaped) that comes from 45 degrees above. Because of that intersection, reproducible positioning of the target is possible (see figure 3.5). For this purpose a three axis computer controlled manipulator, that allows positioning with an accuracy of (50 ± 10) μm , is used. Via Firewire camera the picture of the target is shown at the computer running the control system. With simple drag-and-drop on the monitor it is possible to move the manipulator.

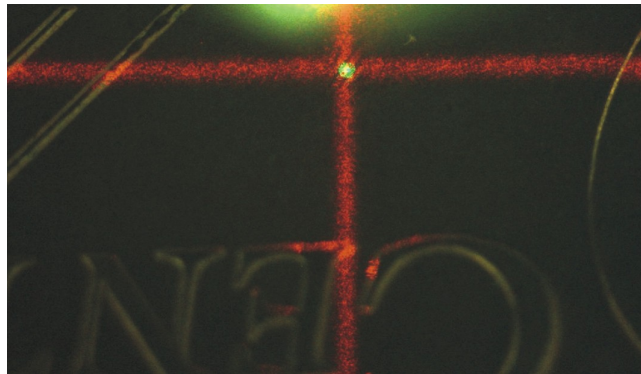


Figure 3.5: Positioning lasers on a 2 Cent coin.

3.2.1 Detection setup

The typical detection setup for performing depth resolved PIXE consist of two detectors: a Si(Li) X-ray detector and a pin-diode detector (Amptek) (see picture 3.6). The Si(Li) detector needs to be cooled all time with liquid nitrogen. It is used in combination with the polycapillary, which is inserted between the detector entrance window ($12 \mu\text{m}$ Be) and the target. The nominal resolution of the Si(Li) is 135eV at 5.89 keV Mn $K\alpha$ and the detection area of the silicon crystal equals 50 mm^2 . The Amptek detector shows, worse resolution features and a greater background. It is used for normalization of the measurements to get rid of errors due to variation of the proton current. The Amptek is equipped with a $150 \mu\text{m}$ Capton-foil in front of its entrance window to stop back scattered protons to penetrate into the detector crystal. In cases where the Si(Li) is used without capillary optics a simi-

lar filter has to be used. Both detectors are at 45° relative to the proton beam access.

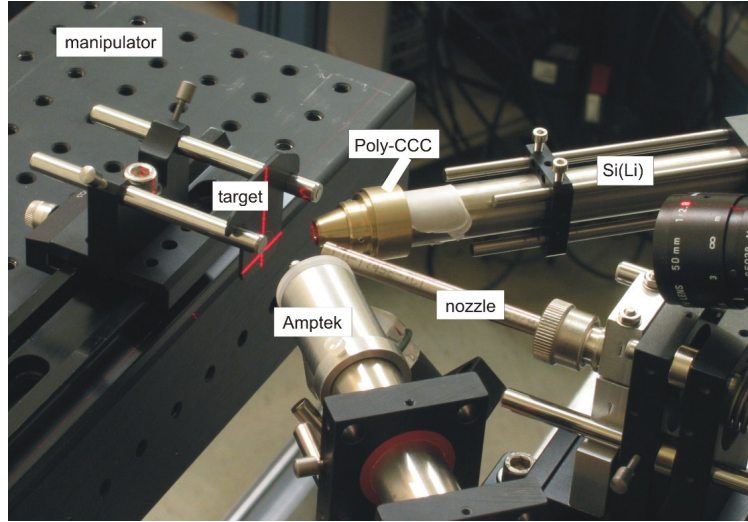


Figure 3.6: Detector Setup used for depth resolved PIXE measurements.

The data acquisition system for both detectors have to be calibrated in energy. The typical standard used for calibration is a ^{55}Fe source, which decays through electron capture to ^{55}Mn . Figures 3.7 and 3.8 show typical ^{55}Fe spectra with the expected Mn $K\alpha$ and $K\beta$ lines at 5.89 keV and 6.49 keV respectively. Comparing the two spectra, the difference in resolution is striking. The FWHM of the Mn $K\alpha$ peak for the Amptek-detector is mostly between 190 eV and 220 eV, the FWHM for the Si(Li)-detector is always around 140 eV.

Also a part of this work was to combine different techniques into one setup. Therefore next to PIXE, PIGE (Proton Induced Gamma Emission) and RBS (Rutherford Back Scattering Analysis) were applied to the assembly. A high purity Germanium detector for detecting γ -rays of nuclear reactions can be mounted instead of the Amptek. To perform RBS measurements a surface barrier detector is located, again under a angle of 45° , underneath the proton nozzle.

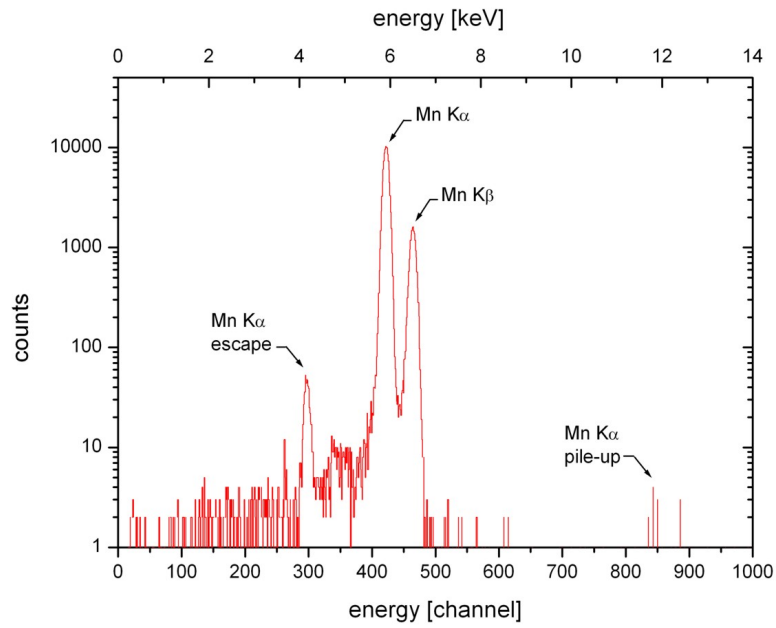


Figure 3.7: ^{55}Fe spectra for energy calibration of the Si(Li)-detector.

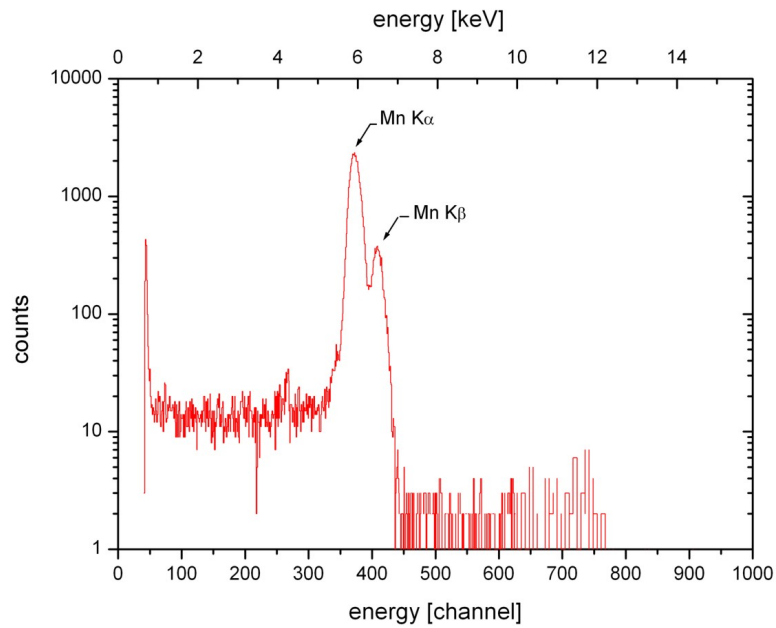


Figure 3.8: ^{55}Fe spectra for energy calibration of the Amptek-detector.

3.2.2 Proton beam profile

For visualizing the beam profile in air exactly at the point where the protons hit the sample, a scan with a Gold-Tungsten-wire with $20\ \mu\text{m}$ in diameter was performed (see figure 3.9 and 3.10). The wire was moved in horizontal and vertical direction at 1 cm after the nozzle window. For analysis the W $L\alpha$ line at 8.4 keV was normalized with the Ar $K\alpha$ peak at 2.96 keV. We assume that the Ar counts are proportional to the mean proton current during a measuring period. The results are shown in table 3.1.

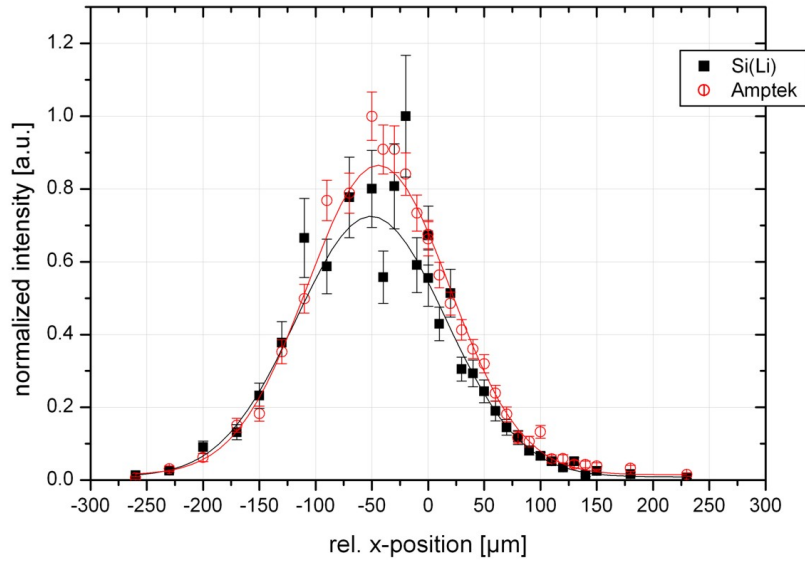


Figure 3.9: Beam profile in horizontal direction scanned with a $20\ \mu\text{m}$ Gold-Tungsten-wire.

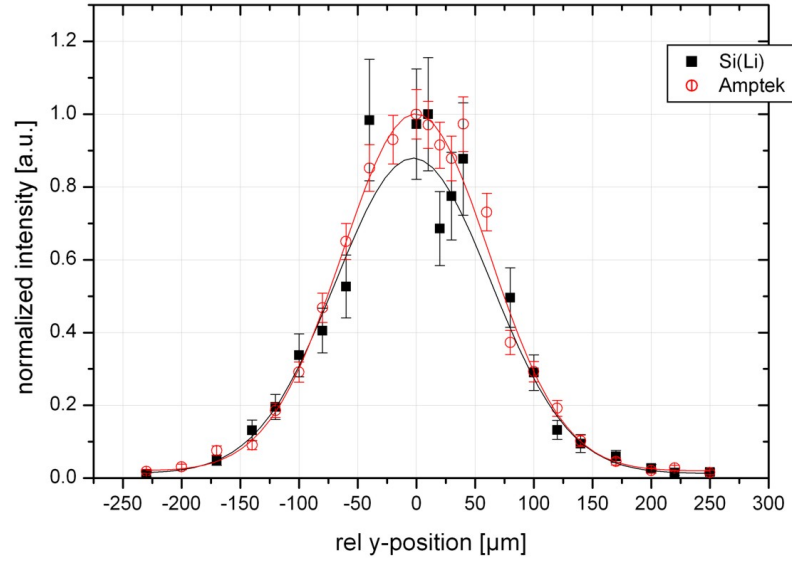


Figure 3.10: Beam profile in vertical direction scanned with a 20 μm Gold-Tungsten-wire.

	horizontal	vertical
FWHM [μm]	152 ± 4	150 ± 5
FWTM [μm]	289 ± 7	289 ± 8

Table 3.1: Dimensions of the H^+ -beam in 1cm distance, measured with a 20 μm -wire.

4 Depth resolved measurements

As the main part of this thesis depth resolved PIXE was performed. The intersection of the proton beam with the "acceptance tube" of a polycapillary forms the detection volume (see also section Polycapillary X-Ray optics). By moving the sample through this volume, layers of different materials can be analyzed.

4.1 Characterization of Polycapillaries

Three different types of polycapillary X-Ray optic structures (see 2.1) have been characterized. A special "sandwich sample" of metal foils was constructed and manufactured in the workshop. Of great interest for the thesis are the changes of the detection volume dependent on X-ray energy, the intensity gains relative to conventional collimators and the ability to enhance the surface relative to the bulk of the sample.

4.1.1 Specification of the target sandwich

The size of the intersection volume (FWHM) for different polycapillaries can be achieved through depth-scans of thin foils (some μm) [17]. To get not only information about the focal spot size dependent on the energy but also particular details about the resolution in depth a target sandwich consisting of two foils was constructed. Each metal foil is glued on a special target holder, that can be used for front as well as for the back position (see 4.1). The target holders, each with a hole of 2 mm in diameter, are mounted in such a way that the foils are facing each other. The distance between is continuously variable with micro meter resolution. Moreover the whole sandwich is installed on a 3-axis translation and 2-axis tilt stage. The stage allows "perfect" positioning of the sample at the intersection point. With an additional z-translation stage the whole assembly can be moved back and forth through the detection volume. In figure 4.2 a typical measuring setup is shown. The foils are listed in table 4.1.

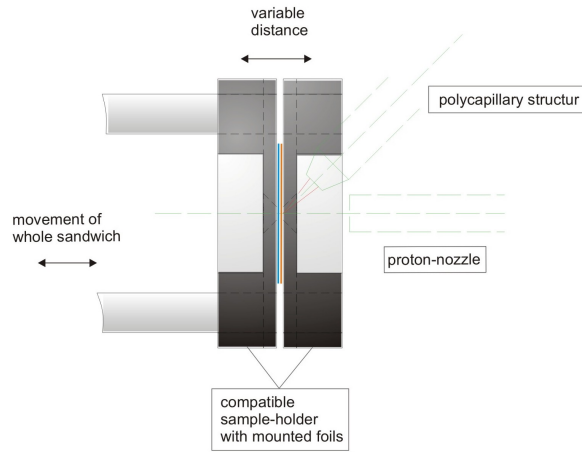


Figure 4.1: Foil-sandwich construction.

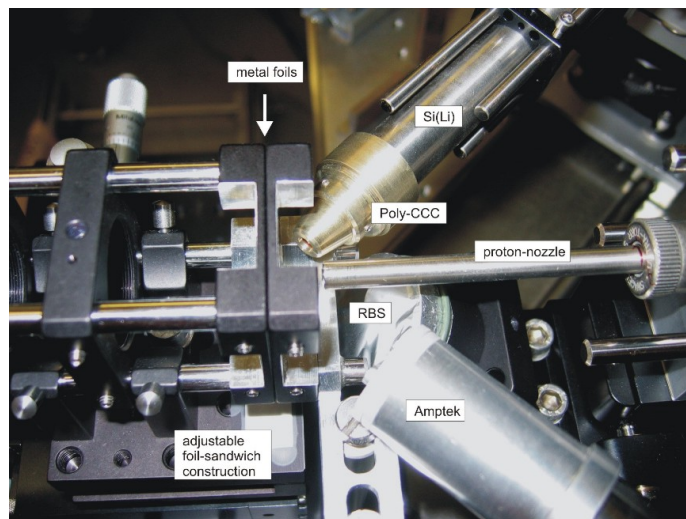


Figure 4.2: Foil-sandwich target during experiments with Poly-CCC 71mls-PCCC14.

material	thickness
Fe	3 μm
Cu	7 μm
Ti	10 μm
Au	4 μm , 20 μm

Table 4.1: Metal foils for the depth scans.

4.1.2 Preparations, measurements and results

Alignment of polycapillaries

The first step of a measuring period is adjusting the polycapillary optics position for maximum intensity (figs 4.3, 4.4). For both lens structures this procedure included scans in horizontal and vertical direction, performed with a tilt station on which the capillaries were mounted in front of the Si(Li) detector. The position along the detector axis has to match the focal distance of each polycapillary. In the case of the Poly-CCC a specially manufactured housing allowed the direct mounting at the end of the Si(Li) nozzle. Because of that, alignment was achieved by moving the whole detector. As a target a carbon-steel foil was used. Due to the composition of different materials this sample shows X-ray lines over a wide range of energies. As a consequence the overall intensity gain is related to the total number of counts (normalized to the counts in the Amptek). This alignment plots already show the different behaviors of polycapillaries. The smaller the lens the more difficult it is to adjust. The Poly-CCC shows, as expected, the greatest transmission of (24 ± 1)% (see also table 4.2). (Note: Due to the fixed mounting on to the detector the positioning procedure in x direction was different from the lenses.) In addition to the total intensity the gross-peak-area of the Fe $K\alpha$ line at 6.4 keV was compared to the same region of interest of the Amptek spectra.

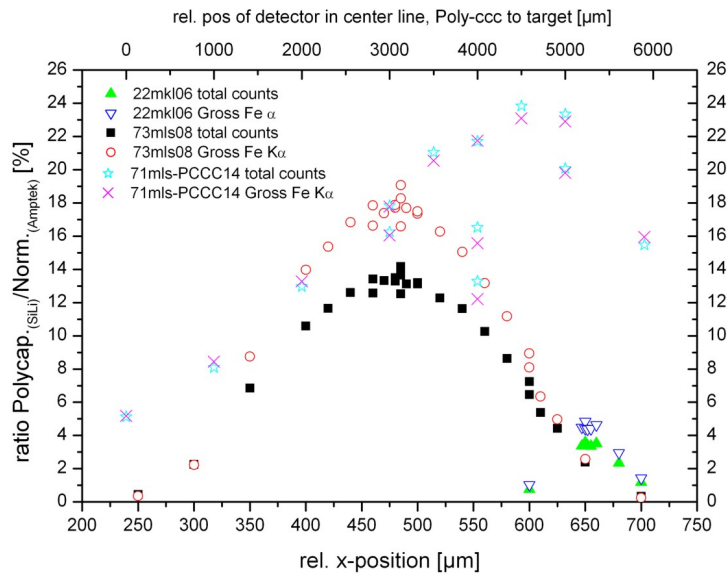


Figure 4.3: Positioning scan in horizontal direction. Due to problems with the fixation of the housing the measuring points of the Poly-CCC show greater scatter.

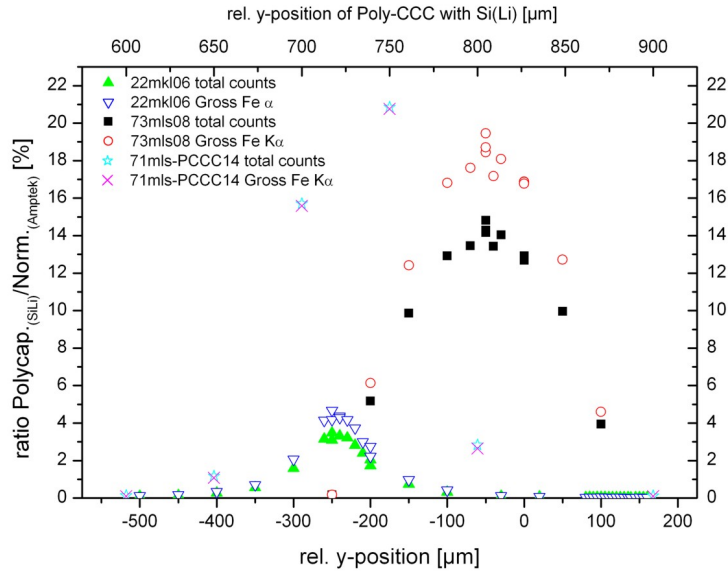


Figure 4.4: Positioning scan in vertical direction.

<i>max. intensity</i> [%]	22mkl06	73mls08	71mls-PCCC14
<i>total spectra</i>	3.6 ± 0.1	14.8 ± 0.1	24 ± 1
<i>Fe Kα</i>	4.8 ± 0.1	19.5 ± 0.1	23 ± 1

Table 4.2: Maximum transmission of polycapillaries during the alignment procedure.

Depth scans and sensitivity curves

After alignment, depth scans with sandwiches of different foil combination were carried out. Each spectra was acquired with a live time of 100 s. The proton current was in the range of some nA depending on the day-to-day tuning of the whole facility. All spectra are recorded and evaluated with the Amptek ADMCA Software. Typical spectra of those foil depth-scans are shown in figure 4.5 and 4.6. They compare the Amptek and the Si(Li) combined with the Poly-CCC for different positions. The change in intensity for the Fe and the Cu peak respectively at different distances from the detection-volume for the case with the Poly-CCC and Si(Li) combination is clearly visible. On the other hand the spectra acquired with the Amptek remain almost constant (and are used for normalization as mentioned before). The Peak to Peak ratios of the two different detection channels are current independent and give relative transmission values.

With respect to the energy of the characteristic X-ray for each individual element the scans represent sensitivity curves of the specific polycapillary structure. The

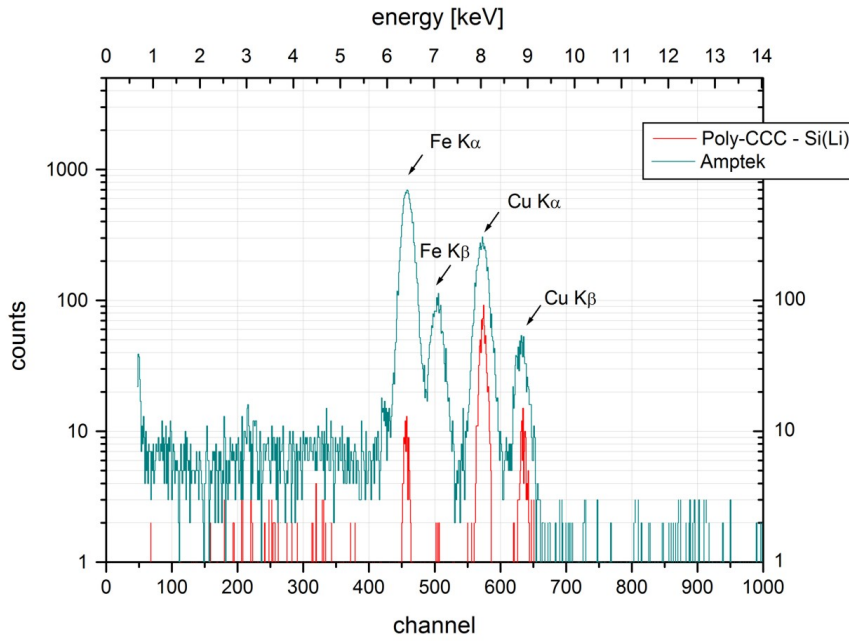


Figure 4.5: Individual spectra of a Fe-Cu foil-sandwich depth-scan with a distance between the foils of $300 \mu\text{m}$ at the relative position $300 \mu\text{m}$.

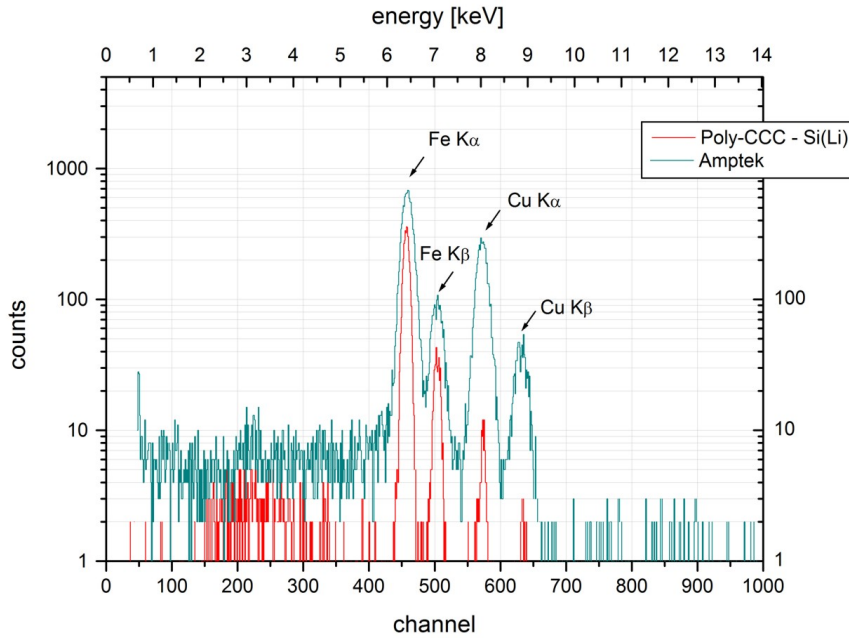


Figure 4.6: Individual spectra of a Fe-Cu foil-sandwich depth-scan with a distance between the foils of $300 \mu\text{m}$ at the relative position $-50 \mu\text{m}$.

scans follow approximately a Gaussian shaped curve. In the case of ideally thin foils that fit is in good agreement with the measurements. This is only valid as long as the dimensions of the proton beam does not dramatically exceed the spatial extension of the focal "tube" of the polycapillary. As a result, and due to the geometry of the intersection, the tip of the curve would get flattened. If the target is of infinite thickness (compared to the small penetration depth of protons) the form of the sensitivity curve deviates more and more from a Gaussian form. Physical effects such as stopping power of protons, deductive energy loss and energy dependent cross sections for X-Ray production as well as self attenuation of electromagnetic rays are strongly affective. Hence, measuring thick target does not represent the sensitivity curve and the intersection volume respectively. (As a first approximation this kind of scans can be described by a convolution of a Gaussian shaped sensitivity curve with a rectangular step function. This square function would represent the limited penetration depth of the protons.)

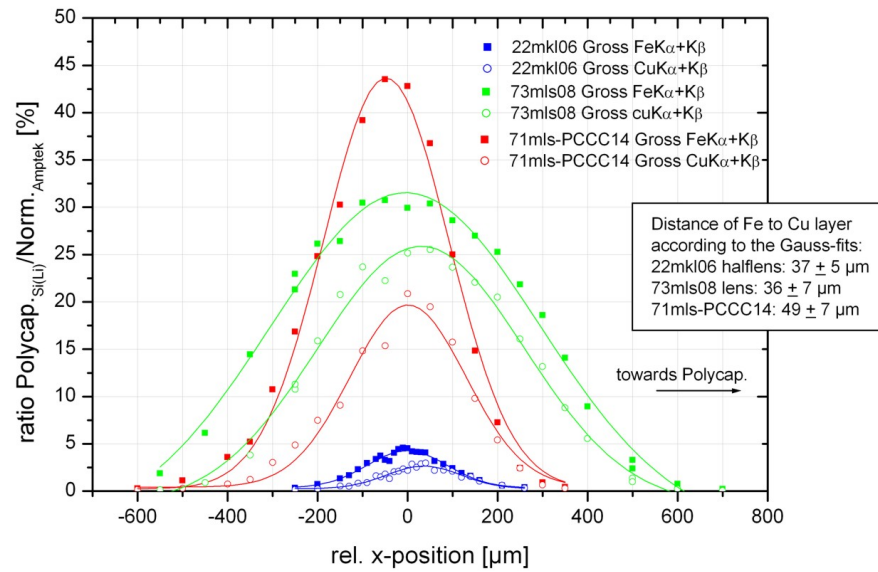


Figure 4.7: Depth scan of a sandwich where a 3 μm thick Fe foil is the front layer and a 7 μm Cu foil is the second, the nominal distance between the foils equals 30 μm. The plot compares all three types of polycapillaries. The values for the measured foil distances are given in the box beneath the legend.

Figure 4.7 is a typical depth scan in comparison with all three tested polycapillaries. The scan shows the ratio of the counts in defined Gross peak areas between the Si(li) (equipped with the polycapillary) and the Amptek. The FWHMs of the Gaussian fits represent the size of the detection volume. All the other conducted

scans can be found in the Appendix A which refer to the obtained FWHM values in table 4.3. The smallest capillary, halfens 22mkl-06 shows the smallest FWHM as expected. Still, the value is higher than the nominal focal spot size would have predicted. This is because of the relatively large extension of the incident proton-beam. Therefore, in this case, the FWHM-scan represents more the size of the proton-beam than the detection volume defined by the construction of the polycapillary itself.

<i>element/energy</i>	22mkl06	73mls08	71mls-PCCC14
Au at 9.7 & 11.4 keV	-	393 ± 13	180 ± 22
Cu at 8.05 & 8.9 keV	204 ± 12	512 ± 15	307 ± 12
Fe at 6.4 & 7.06 keV	219 ± 8	674 ± 40	307 ± 36
Ti at 4.5 & 4.9 keV	217 ± 22	961 ± 178	377 ± 16
Au at 2.12 keV	-	-	348 ± 26

Table 4.3: FWHM in μm of the detection volume for the three types of polycapillary with respect to the X-ray energy.

The plots in figure 4.8, 4.9 and 4.10 are compilations of all measured points combined by normalizing to 1, distinguished only by the incoming X-ray energy. These so called sensitivity curves for the size of the detection volume are all in good agreement with a Gaussian shaped fit. In the case of the lens-structure the dependency of the volume size on the X-ray energy is conspicuously visible (fig. 4.9). Here the curves follow the inverse proportionality of the energy to the critical angle of total reflection and consequently the expansion size of the focal area increases and decreases respectively. Nevertheless, especially going to lower energies, the measuring points are widespread. This deviation also occurs in the measurements with the half-lens structure (fig. 4.8). But, due to the less widening with decreasing energy, the sensitivity curves for Fe and Ti X-rays overlap. The plot achieved with the Poly-CCC seems to be also in good agreement with the expected change in FWHM. Only the Gaussian of the Au M line at 2.12 keV, and therefore a explicit lower energy than all the other measured lines, does not follow that rule. It appears that the fit is located in the same region as Cu at an average energy of ≈ 8.5 keV. A possibility to explain this unexpected behavior, is the loss in reflectivity of the glass material at larger incident angles. Due to their low energy the theoretical expansion of the focal plane would be bigger in size, but it experiences a restriction by great loss in transmission at the edging.

Those intensity curves converted into sensitivity functions would already be the convolution of the incident proton beam with the detection area of the polycapillary. This theoretical description of the detection volume would be necessary for elemental concentration analysis of layered structure measured with a polycapillary setup.

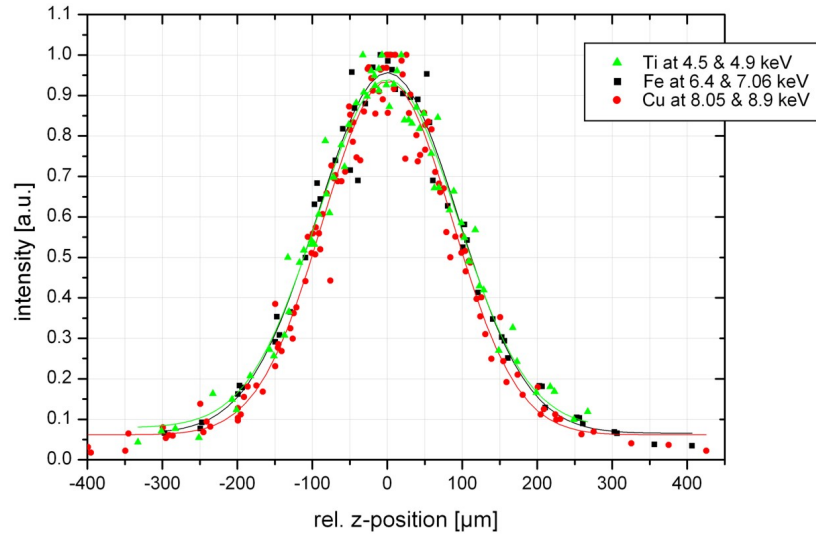


Figure 4.8: Sensitivity curves for different X-Ray energies referring to polycapillary half-lens 22mkl 06.

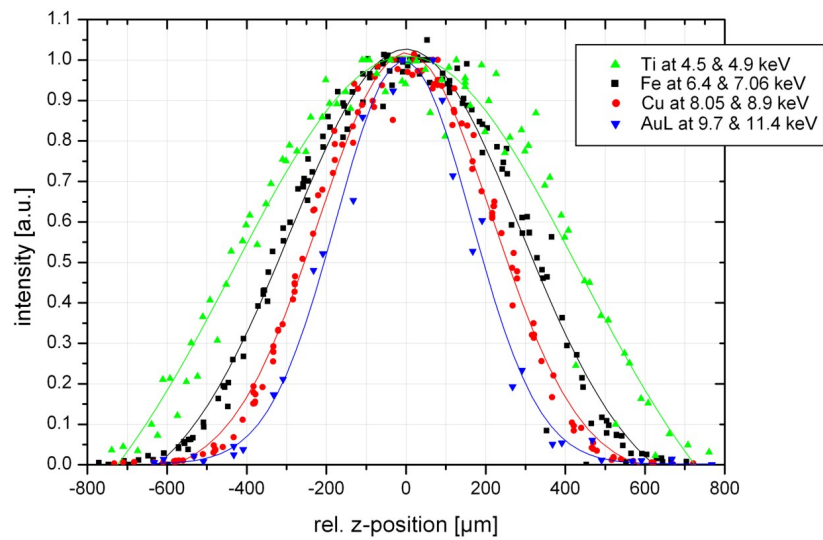


Figure 4.9: Sensitivity curves for different X-Ray energies referring to polycapillary lens 73mks 08.

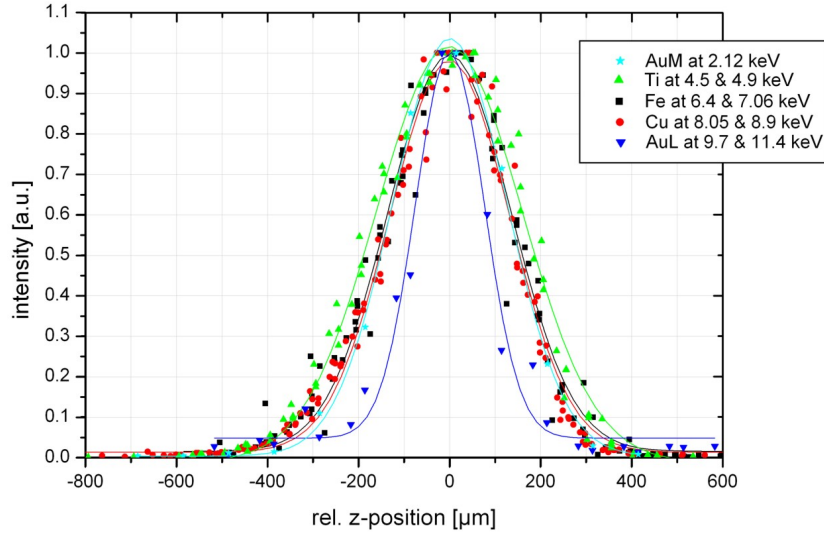


Figure 4.10: Sensitivity curves for different X-Ray energies referring to Poly-CCC 71mls.

Figure 4.11 shows the habit of changing the distance between target and Poly-CCC entrance. It is representative for the acceptance angle of the capillary and the localization of the focal "tube" waist. Due to problems with mounting the housing of the capillary, the measurements for the depth scans were performed at position 0 mm which promised the most stable conditions. But referring to this plot better values for intensity gains as well as for the FWHM could be achieved at position -2 mm. The FWHM could be reduced by a factor (0.63 ± 0.02) and the transmission increased by a factor of (1.2 ± 0.1) respectively. The according FWHM and transmission intensities are listed in table 4.4.

rel. Poly-CCC - target pos.	FWHM [μm]	max. transmission [%]
0mm	317 ± 8	28.4 ± 0.1
2mm	539 ± 28	10.6 ± 0.1
-2mm	200 ± 3	35.0 ± 0.1
-4mm	435 ± 30	11.9 ± 0.1

Table 4.4: FWHM and max. intensities referring to different distances of Poly-CCC and target.

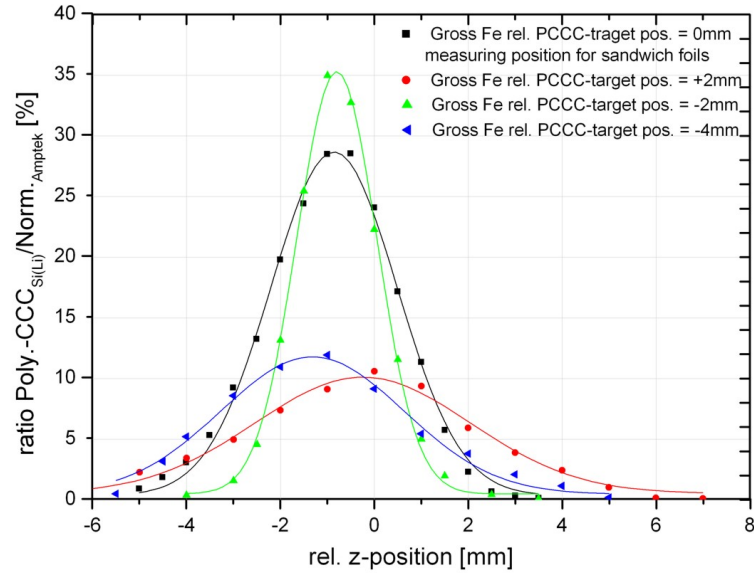


Figure 4.11: Change of distance between Poly-CCC entrance and target impact point.

Transmission

The next plot (4.12) shows the gained transmission intensity by using polycapillary optics in the detection channel. The determined values are only in relation to the simultaneously measured signal which had reached the Amptek-detector. In the energy range from 6.4 keV to 8.9 keV the ratio between Si(Li) and Amptek are 4.4% - 2.4%, 25.2% - 29.5% and 42.0% - 16.3% for hal-lens, lens and Poly-CCC respectively. This transmission seems quite low, but taking into account that the Amptek "sees" a solid angle of 0.08 sr which is a factor of 180 to 1430 times larger, depending on the X-ray energy, with respect to the observed area of a particular polycapillary the term of transmission gain is more than valid. (The factor is calculated by assuming the measured FWHM of the sandwich scans to be the diameter of a collimator which is situated at the same distance from the target as the Amptek.)

The Poly-CCC shows the strongest transmission. Especially at 2.12 keV, the Au M line, a gain of 3450% was observed. One of the main reason for such an outstanding value will be the bad efficiency of the Amptek in this low energy region. Comparing the values of the middle energy region of the Poly-CCC to those of the lens-structure it is visible that in the majority of the cases the conic collimator shows higher transmission, even if the detection volume of the lens is almost two times larger in diameter. This effect is due to the great length of the lens and the focusing spot on both sides. These two geometry factors cause a strong increase in the num-

ber of needed total reflections to guide the photons through the capillary. Hence, more hits result in a bigger loss of intensity, due to absorption effects. This is also the reason why the transmission intensity decreases with lower energies in the case of half-lens and lens. A lower energy would indicate a larger critical angle and a greater acceptance angle respectively. But a larger incident angle of the X-rays also results in more hits of the capillary walls and therefore a slightly decrease can be observed. This is not effective for the Poly-CCC because of two advantages. First, it is the shortest polycapillary structure in the set. And secondly, the straight alignment of the individual capillaries reduces the number of reflection dramatically (see also section 2.2 Polycapillary X-ray optics).

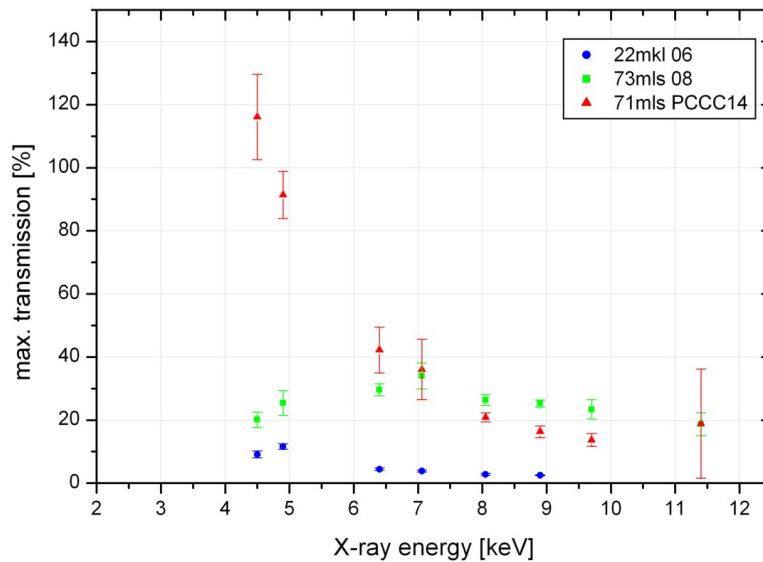


Figure 4.12: Maximum of transmission dependent on energy in comparison with the different polycapillary types.

Background suppression

In terms of how the different layers of materials in depth are suppressed by this measurement method the positive discrimination of the front layer was investigated. For this purpose the depth scan of the Fe-Cu-sandwich sample (referring scans see figure 4.7) was analyzed. To assure the equal comparison of different materials, two main factors have to be taken into account. At first the K-shell ionization cross section is different for each individual atomic number and dependent on the incident proton energy, which will change with the penetration-depth due to ionization processes. The loss in energy, when the protons have pass the first layer of Fe, was calculated

with the software package RBS V3.21 [34] and could be determined to be not negligible. The ratio between the different cross section of Fe and Cu was then calculated with the associated data acquired with the Amptek. Moreover, effects in terms of self absorption of the X-rays in the target, even if only of minimal impact, as well as fluorescence yields, are included. The second important factor is the individual response of the polycapillary for different X-ray energy. Hence the sensitivity curve and the size of the detection-volume respectively are strongly effecting the detected X-ray counting rate of the individual characteristic X-ray. Therefore the relative gain in intensity between Fe and Cu has to be included. Figures 4.13, 4.14 and 4.15 show for both layers the intensity gain in percentage when assuming the not considered layer to be a 100% at each position in the depth scan. The front iron layer is obviously in favour in all three plots. If the detection volume is still before the front foil and has not entered the sandwich yet, this gain can reach, in the cases of the lens and the Poly-CCC, values of 1100%. By measuring with the half-lens 485% could be determined. The copper back layer hardly reaches 100%, even at its highest intensity. The individual maximum values are 73%, 88% and 48% for half-lens, lens and Poly-CCC respectively. It can be concluded that with the use of polycapillaries a strong background suppression can be achieved. Therefore these kind of optics are suitable for any kind of measurements where the background layer (e.g. paintings) would effect the result negatively.

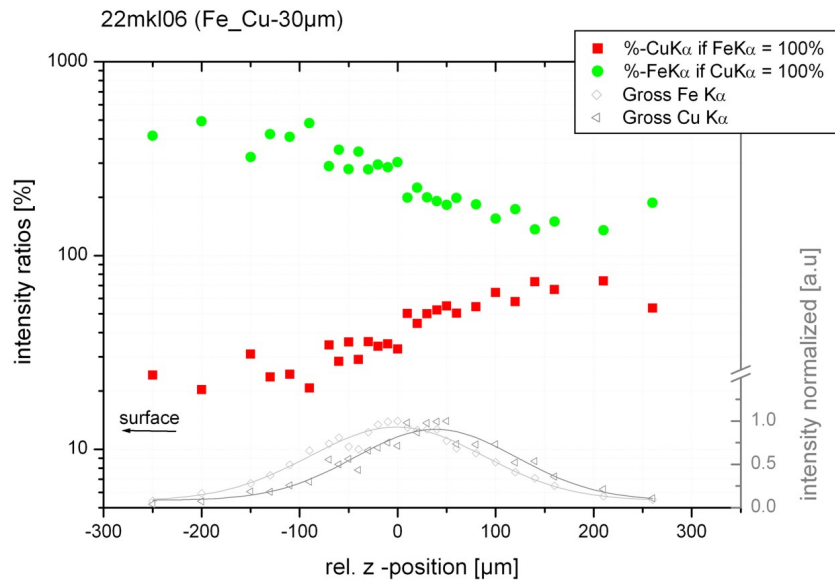


Figure 4.13: Scan of a Fe-Cu sandwich with a $30\mu\text{m}$ distance, performed with **half-lens 22mkl 06** (gray scales), intensity gain of front and back layer (colored scales).

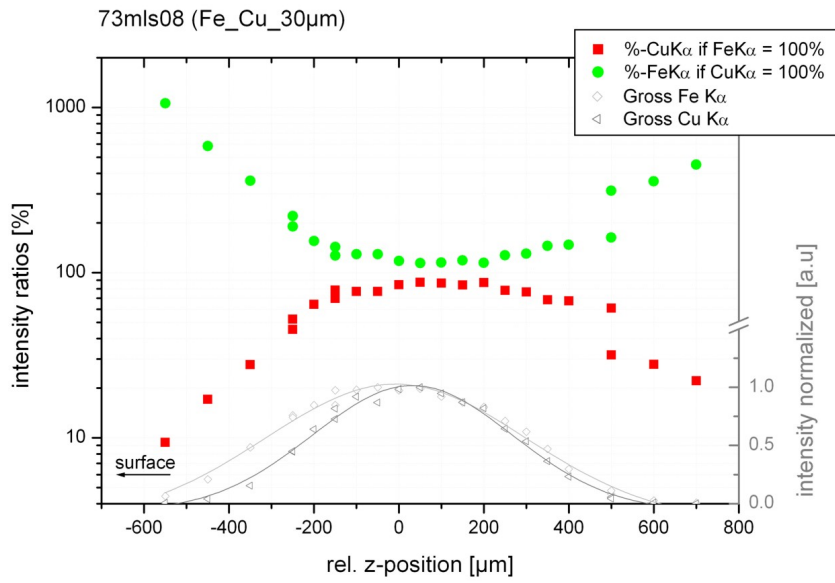


Figure 4.14: Scan of a Fe-Cu sandwich with a $30\mu\text{m}$ distance, performed with lens **73mls08** (gray scales), intensity gain of front and back layer (colored scales).

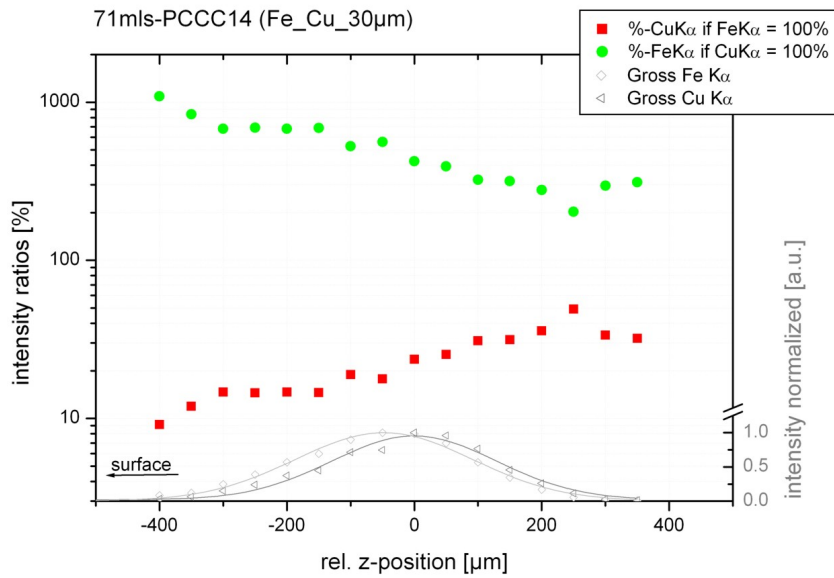


Figure 4.15: Scan of a Fe-Cu sandwich with a $30\mu\text{m}$ distance, performed with **Poly-CCC 71mls-PCCC14** (gray scales), intensity gain of front and back layer (colored scales).

Depth-resolution

By measuring sandwich samples the ability of depth resolving PIXE analysis was tested. Due to the use of thin foils, problems with absorption effects and stopping power of protons did not influence the results significantly. The plot in graphic 4.16 shows the applied value of the foil distance in comparison to the achieved center differences of the Gaussian fits in the depth scans. With considering the error bars the measured values overlap with the nominal ones. The accuracy of the adjusted foil position was estimated as a combination of the scale reading precision of the micrometer-counter by $\pm 1 \mu\text{m}$, the systematic error of the foil mount of $\pm 5 \mu\text{m}$ and a $\pm 1 \%$ inaccuracy of the micrometer-screw. The calculated weighed mean-deviation values with external error analysis are $(3.6 \pm 3.5) \mu\text{m}$, $(6.2 \pm 4.2) \mu\text{m}$ and $(6.0 \pm 3.2) \mu\text{m}$ for half-lens, lens and Poly-CCC respectively. The lens-structure shows the worst depth-resolution abilities. Note: For the mean value calculations of 22mkl-06 only the measured distances which did not show any systematical error (further explanation see Appendix A) were considered.

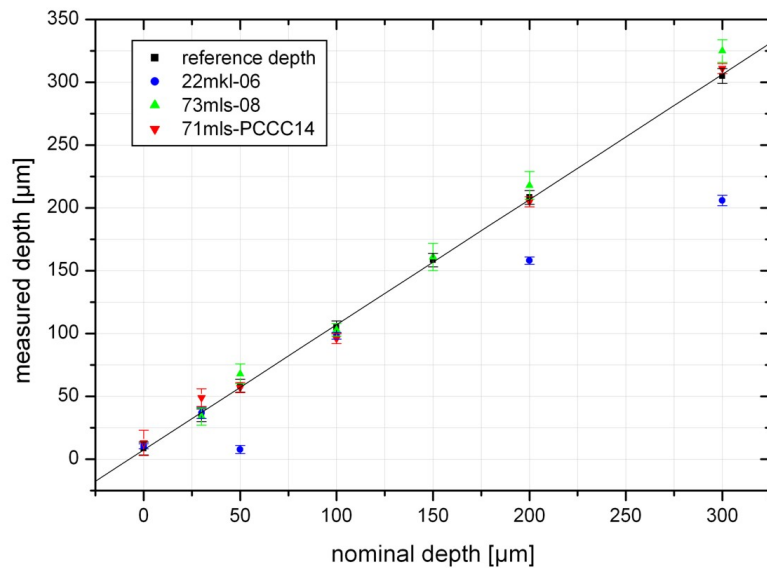


Figure 4.16: Comparison of nominal depth values to measured foil distances. The three strong deviating values of 22mkl-06 at 50, 200 and 300 μm are originating from a systematical error in the construction and are not used for further calculations.

4.1.3 A coin sample

To show the ability of depth resolved PIXE analysis, a non ideal sample was analyzed. The target is a 2-Cent-coin which consist of an iron core coated with copper. It is not known if the thickness of the coating is homogeneous, but apart from that fact the following result could be achieved: $(15.2 \pm 6.6) \mu\text{m}$ is the average thickness for the copper layer over all measurements, where the small half-lens 22mkl-06 showed the best resolution abilities and accuracy for discrimination of the two layers (fig. 4.17). The great error value in the center difference in the scan performed with lens 73mls-08 (fig. 4.18) originates from the use of the motorized manipulator instead of a more precise micrometer-screw. Due to measuring a thick sample, properties of the proton stopping power in the sample are gaining importance. A Gaussian shaped increasing slope is stopped abruptly followed by a steep decrease, which results in a non-symmetrical shaped curve. This phenomenon is clearly visible in the scan with the Poly-CCC (fig. 4.19). In this case the effect is so dominating, that by fitting the counting ratios with a Gaussian function it seems as if iron is the top layer instead of copper. The fit for Fe $K\alpha$ is strongly shifted to the left side. Only in the increasing slope the real order of the material is visible. The displacement of the two curves was determined at half maximum of height at the surface facing side of the scans.

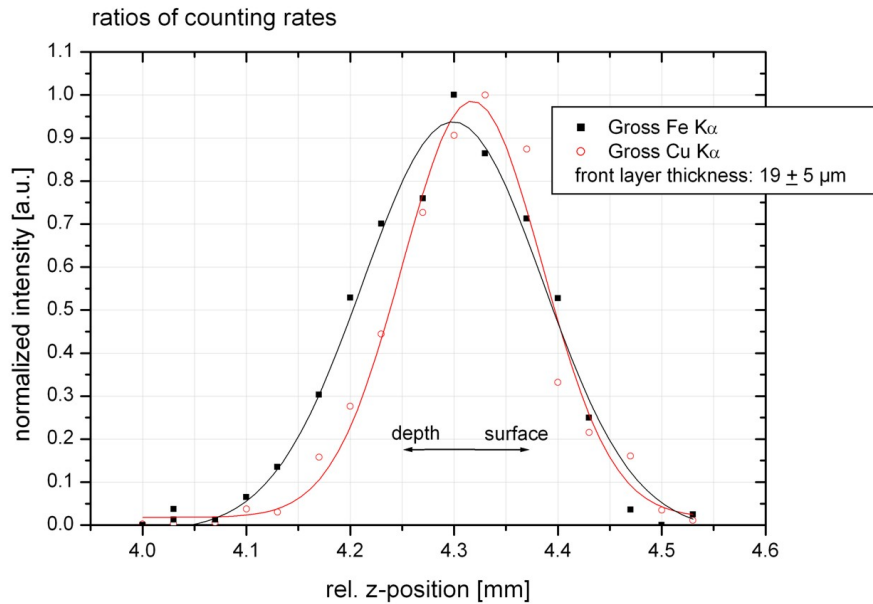


Figure 4.17: Scan of a 2 Cent coin with half lens 22mkl 06.

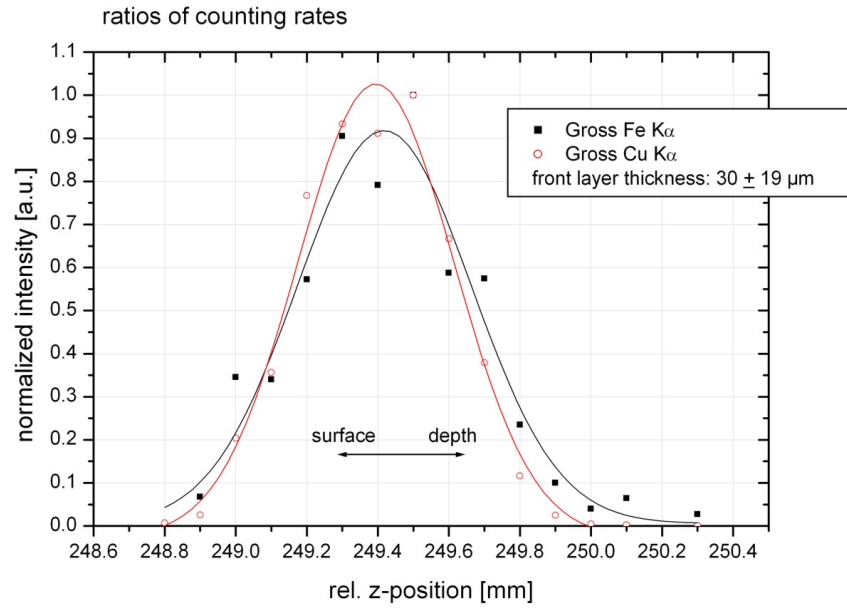


Figure 4.18: Scan of a 2 Cent coin with lens 73mls 08.

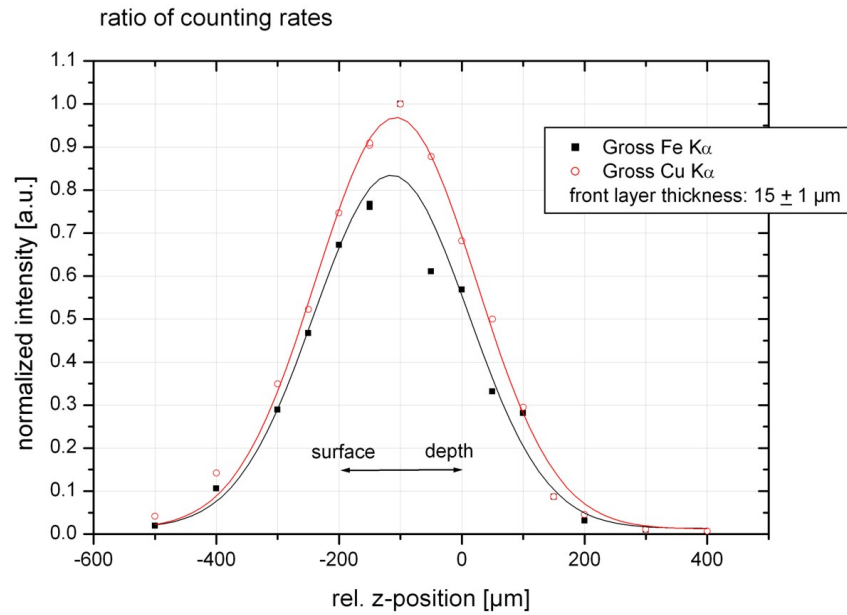


Figure 4.19: Scan of a 2 Cent coin with Poly-CCC 71mls.

5 Determination and verification of elemental concentrations

As an additional part of this thesis the accuracy of quantitative PIXE analysis with the recently installed setup at VERA was investigated. Therefore, well known samples (measured and evaluated at different laboratories) have been remeasured.

5.1 Description of the samples for verification

The samples are Roman coins from the time of Cesar Traian, coins from the Ottoman Empire and iridescent Art Nouveau glasses. They were provided by Prof. Manfred Schreiner, head of the Institute for Natural Sciences and Technology in the Arts, Academy of Fine Arts, Vienna. External PIXE is particularly suited to study such objects of art. Coins and glasses may become one of the future fields of application for PIXE at the VERA facility.

5.1.1 Traian coins

A selected set of denarii from the time of Caesar M. Ulpus Traianus were object of the investigation. In the twenty years of Caesar Traians reign (98-117 AD) the Imperium Romanum expended in a great region. Several important wars, like the two wars against the Dacia (101-102 AD and 105-107 AD) as well as the campaign in the east (until the Persian Gulf, 113-117 AD) were part of his aggressive, ideological regime [36]. The roman coinage, which was continuously over the whole time period of Caesar Traians reign is a major source of information. 71 silver denarii from different consulates were investigated with μ -RFA (micro X-ray fluorescence analysis) at the Academy of Fine Arts in Vienna. To avoid errors due to surface enrichment in silver, polished cross-sections of the coins were prepared. This procedure is necessary because of the considerable thickness of the enriched surface layer, which is in the range of several 100 μ m. In the scanning electron microscope picture (5.1) a lighter outer zone is visible. Typical cleaning processes of the coin surface would not be enough to remove the surface layer and expose the bulk for analysis. This holds true as well for the electron beam as for the proton beam. Previous results showed that all coins contain of an silver-copper alloy with traces of lead and gold. Coins up to the time of the second consulate show more or less the same silver content (87%) as those from Traians antecessor. In the coinage of the following consulates (III to VI) a decrease in silver to averaged 79% could be determined. This reduction in fineness

may be linked to the preparations for the Dacian wars.

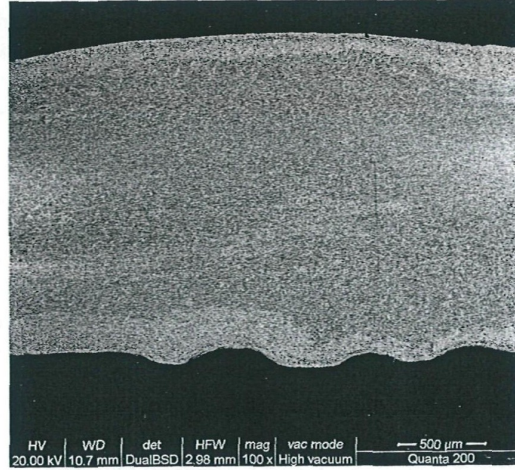


Figure 5.1: Scanning electron microscope picture of the cross-section of Coin # 41 [36].

In this thesis four Traian coin samples from the fifth consulate have been analyzed (see table 5.1).

Nr.	obvers-legend	revers-legend	revers-typ	dating	weight
34	IMP TRAIANO AVG GER DAC P M TR P COS V P P	S P Q R OPTIMO PRINCIPI	Annona stands to the left	ca. 106 -107 AD	2.92 g
35	IMP TRAIANO AVG GER DAC P M TR P COS V P P	S P Q R OPTIMO PRINCIPI	Felicitas stands to the left	ca. 106 -107 AD	3.18 g
40	IMP TRAIANO AVG GER DAC P M TR P	COS V P P S P Q R OPTIMO PRINC	tropaeum -108 AD	ca. 107	2.71 g
41	IMP TRAIANO AVG GER DAC P M TR P	COS V P P S P Q R OPTIMO PRINC	Dacia sits on weapon, DAC CAP	ca. 107 -108 AD	2.77 g

Table 5.1: Selected set of Traian coins.

5.1.2 Coins from the Ottoman Empire

Silver-copper coins from the time period of the Ottoman Empire referring to different sultans were analyzed. Except for their historical relevance no further information of the stated art historical question was accessible. Table 5.2 is a summary of the coin details. First measurements were performed with external PIXE at the Louvre laboratories in Paris [32].

number	site	sultan
31138	Amid	Murad III
31147	Amid	Murad III
31054	Ankara	Mehmed III
31137	Halep	Mehmed III
31133	Halep	Mehmed III
31128	Halep	Mehmed III
31121	Ohri	Mehmed III
31124	Ohri	Mehmed III

Table 5.2: Information of the coins from the time of the Ottoman Empire, reign of Murad III from 1574 - 1595 and of Mehmed III from 1595-1603 respectively.

5.1.3 Iridescent Art Nouveau glass

Around 1900 precious glass artefacts were produced by Tiffany (USA) and Loetz (Austria) (5.2). These specific kind of glasses show a iridescent effect on their surface. This phenomenon is known from a thin oil layer on water surfaces and is a combination of optical effects like light diffraction, dispersion and interference. In the case of Art Nouveau glasses this iridescent effects are produced by applying alcoholic solutions of stannous chloride or mixtures of metallic salt on the hot surface followed by a reheating process in a reducing atmosphere [23]. This procedure results in a very thin SnO_2 layer in the order of 50 nm in thickness [11]. In the case of Tiffany the bulk material of these samples is borosilicate glass with a high content of lead. On the contrary the bulk material of Loetz glasses consists of potash-lime-silica with a very low lead content. Additionally they are coated with a lead and silver glass layer of 100-300 μm thickness. Moreover, Loetz used the Papillion (butterfly) technique so that the surface appears as two different colored areas. The lighter ones are made by rolling the incomplete blown glass object over small, reach in silver and lead, glass splinters, followed by an additional reheating before treating the surface to achieve the iridescence effects. There is an additional layer within the composition of Loetz glasses. It is a transition area between the surface and the bulk. About 80% of the tin are located in this zone. Only 20% of Sn are in the most outer layer. These results are established by applying ion beam analysis methods (PIXE, PIGE & RBS) [11] as well as energy dispersive X-ray fluorescence (EDXRF) [12].

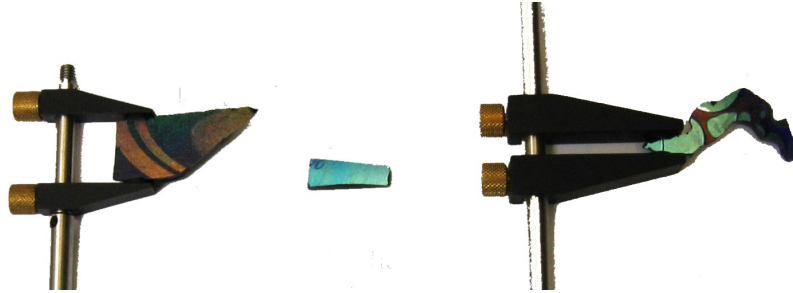


Figure 5.2: Iridescent glass samples (from left to right): Glas232 in holder (unknown origin), Tiffany T10, Loetz sample in holder.

5.2 GUPIXWIN

To perform quantification the software package GUPIXWIN was used. This is the Windows-XP version of the standard GUPIX program, which was developed by the PIXE group at the university of Guelph [25]. It is a non-linear-least-square fitting program for PIXE spectra and allows to derive element concentrations from the areas of X-ray peaks in the spectrum. Such an elaborate evaluation procedure is required for thick samples due to self absorption effects and the energy dependent production rates of X-rays. (For thin samples, quantitative analysis would be much simpler: Taking cross section of K-hole production and fluorescence yield into account, simple counts to concentration relation can be used.) To illustrate the influence of x-ray self absorption and proton energy loss a series of measurements on reference materials was not only correctly evaluated as thick samples but also intentionally wrong as thin samples. The strong deviation from the reference value is shown in figure 5.4 and 5.5 (red dots). To run a concentration calculation in GUPIXWIN all elements in the sample must be given as input. It calculates then in an iterating process the percentage of major elements. After the matrix composition is derived the trace elements can be evaluated. To avoid errors caused by proton dose measurements, GUPIXWIN offers the possibility to normalize concentration to 100%.

5.2.1 Detector efficiency

To fully characterize the setup for quantitative analysis the knowledge of the detector efficiency is of great importance. A typical efficiency curve consists of two parts, the geometric and the intrinsic one. The geometric part of the efficiency is calculated by GUPIXWIN from the various input parameters (e.g. distances, angles, detector surface area,..) and is considered energy independent. The second part, the intrinsic efficiency of the detector crystal, is the ratio of the full-energy peak intensity to the number of incident photons upon the crystal. It can be calculated with detailed knowledge of the detector internals (see formula 5.1)[14]. The intrinsic efficiency ϵ_i

contains all energy dependencies, e.g. with increasing X-ray energy the interaction depth of the photons moves further into the detector crystal, thus the effective solid angle is energy dependent.

$$\epsilon_i = \frac{\left(1 - e^{-\mu_{Si}D}\right) e^{-\sum_j \mu_j t_j} f_E}{(1 + z/d)^2} \quad (5.1)$$

where

$$z = \frac{1 - \left[e^{-\mu_{Si}D}(1 + \mu_{Si}D)\right]}{\mu_{Si}(1 - e^{-\mu_{Si}D})}$$

t_j defines the thickness of the various absorbing layers j (e.g. ice-layer, dead-layer,..), D is the thickness of the silicon crystal, d is the distance between the impact point on the target and the crystal surface, μ_j and μ_{Si} the linear absorption coefficient with respect to the material and f_E losses of events due to Si K X-Ray escape.

Measurements of the detector efficiency were performed with calibrated sources (e.g. ^{241}Am) for higher energies. A particular problem are the low energies from 5keV down. On the one hand no suitable calibration sources were available in this energy region and on the other hand the efficiency falls-off very steeply due to a combination of X-Ray attenuation and ionization charge loss in the frontal layers. Hence, for this thesis a theoretical intrinsic efficiency curve 5.3 is used for description of the detector setup for GUPIXWIN analysis. The linear absorption coefficients are taken from [10]. Further, the calculated values have been modified to be in good agreement with the measured Ag/Cu standards.

The final efficiency curve (see 5.3 dots) used for concentration analysis in GUPIXWIN was therefore adapted to achieve best results.

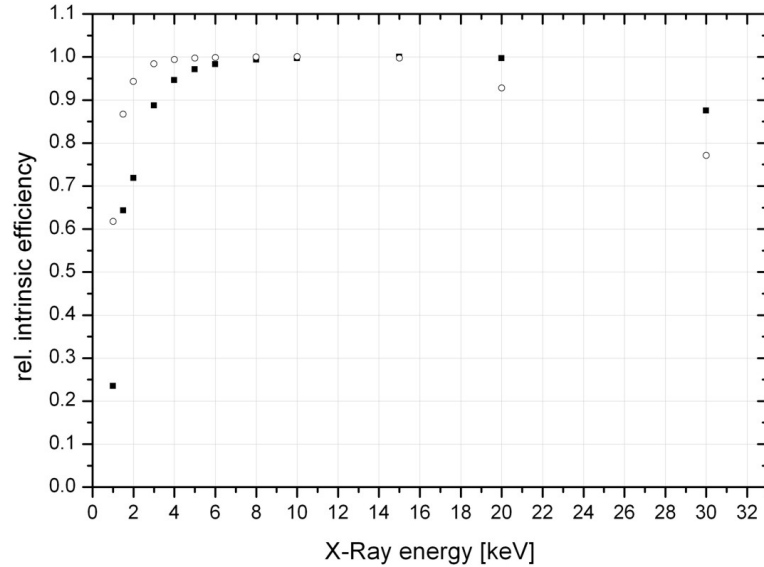


Figure 5.3: Intrinsic efficiency curve of our Si(Li) detector. The steep fall-off of the efficiency in the low energy region is due to absorbers, the decrease at high energy is related to the detector crystal thickness.

5.3 Results

5.3.1 Standards

To calibrate the system and software, standards with known element concentrations were analyzed. For best results a set of standards referring to a specific sample and its content has to be measured during an experimental run. In the case of the Traian and the Ottoman coins a set of silver-copper standards, named ÖGUSSA-Standards, each with a different known composition was used. Figure 5.4 and 5.5 show the result of the calibration procedure, performed in the iterative matrix element solution mode of GUPIXWIN with the option for normalized concentrations.

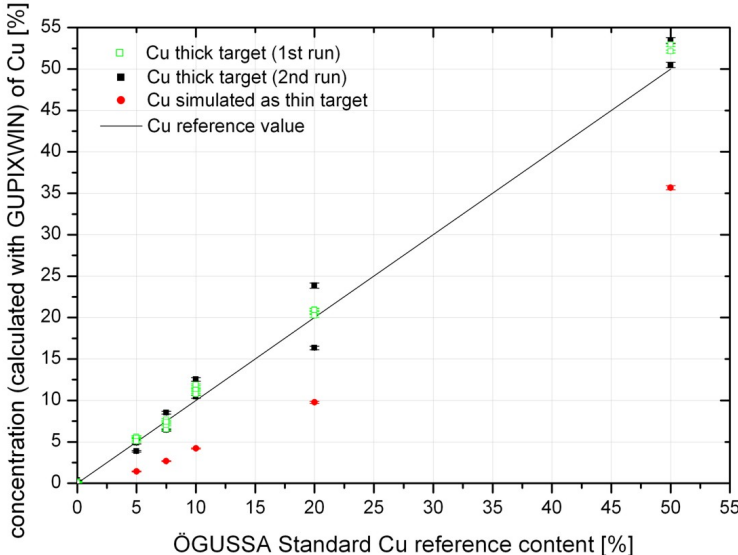


Figure 5.4: Cu content of ÖGUSSA Standards.

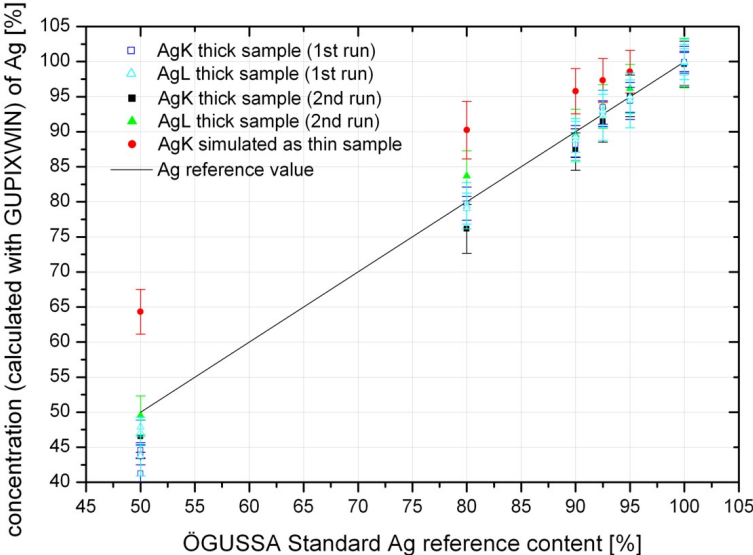


Figure 5.5: Ag content of ÖGUSSA Standards.

The quiet big offset of the 50:50 % Ag to Cu standard was remeasured with another material analysis method and performed of Mag. Marta Rodrigues from the Academy of Fine Arts Vienna. The EDX (Energy dispersive X-ray) analysis resulted in 54 % of Cu and 46 % of Ag. Both measurements are in good agreement to each other.

5.3.2 Traian coins

The PIXE results are evaluated with a live-time of 300 s and a mean proton current of 20 nA. Each result is the weighted average of three different measuring spots, distributed over the whole cross-section of a coin (exception was the outer silver enriched area). In the GUPIXWIN analysis the matrix components Ag, Cu, Au and Pb were treated as 100% for each individual measured spectra, to insure the independence of the proton-current instabilities. The results of the measurement series at VERA are listed in table 5.3 (see also figure 5.6). In addition the results achieved with μ -XRF, performed earlier at the Academy of Fine Arts in Vienna, are given.

coin #	V Ag	A Ag	V Cu	A Cu
34	78.2 ± 1.3	80.1 ± 0.8	20.3 ± 1.4	19.7 ± 0.8
35	79.1 ± 1.9	79.8 ± 0.3	19.7 ± 1.7	20 ± 0.0
40	83.7 ± 5.3	82.4 ± 3.8	12.9 ± 4.7	17.3 ± 3.6
41	90.9 ± 1.5	91.9 ± 1.2	7.4 ± 1.0	7.7 ± 1.3
coin #	V Pb	A Pb	V Au	A Au
34	1.4 ± 0.1	0.33 ± 0.02	-	-
35	1.1 ± 0.2	0.28 ± 0.01	-	0.04 ± 0.01
40	1.3 ± 0.1	0.24 ± 0.01	0.4 ± 0.1	0.05 ± 0.01
41	1.1 ± 0.4	0.32 ± 0.06	0.3 ± 0.1	0.06 ± 0.01

Table 5.3: Element concentrations of Traian coins, comparison between results achieved at VERA and measurements performed at the Academy of Fine Arts Vienna, V = measured at VERA with PIXE, A = measured at Academy of Fine Arts Vienna with XRF, all values are in %. The symbol - indicates that this element could not be found in the measured spectra.

Firstly, those results give information about the homogeneity of the silver-copper-compound. Only coin number 40 shows a larger error, which implicates that in this case the elements are quite inhomogeneously spread. Moreover, comparing the results of PIXE and XRF, again coin 40 shows the greatest deviation. By using weighted average analysis this inhomogeneity does not affect the mean absolute deviation significantly. Calculations for the absolute deviation result in $(1.31 \pm 0.25)\%$, $(0.5 \pm 1.1)\%$, $(0.12 \pm 0.10)\%$ and $(0.85 \pm 0.08)\%$ for Ag, Cu, Au and Pb respectively. The relative deviations are the following: Ag $(1.5 \pm 0.3)\%$, Cu $(3.1 \pm 6.4)\%$. The elements that are not prominently present in the matrix, Au and Pb, are not considered here. In relation to the refernece values, calculated in percentage of the given value, they show enourmus differences. Moreover these values are always higher than

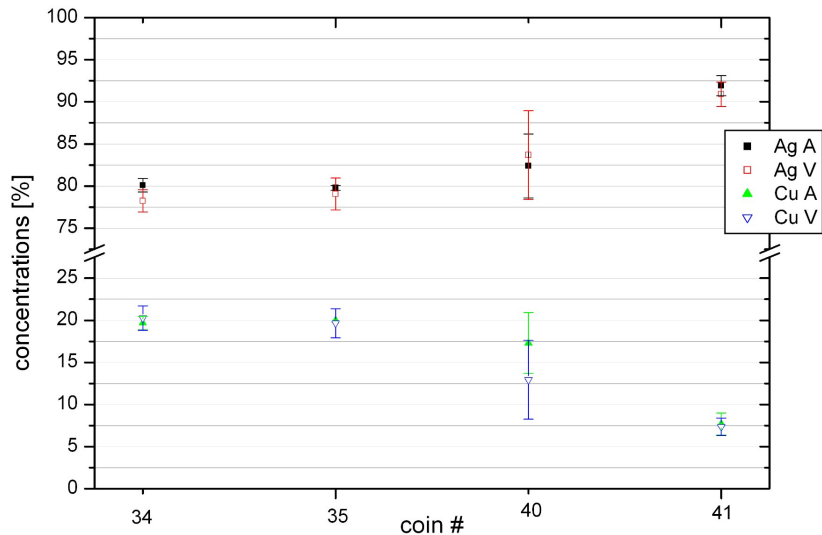


Figure 5.6: Comparison of Ag and Cu content in the Traian coins. V = PIXE results from VERA, A = XRF results from the Academy of Fine Arts.

the one measure with XRF (originating from peak areas smaller than necessary for GUPIXWIN concentration analysis, furthermore no standards especially for those elements were measured). In comparison, the absolute deviations in concentrations of Ag and Cu are typically within the area of measuring uncertainties without systematical measuring errors.

In addition the silver enriched outer area was investigated by performing line-scans of the cross-section of coin number 34 (fig. 5.7) and 41 (fig. 5.8).

Please note that all Cu-Ag spectra have been analyzed twice with the GUPIXWIN software. One time with using the L-lines of silver and the other time using the higher energetic K-lines.

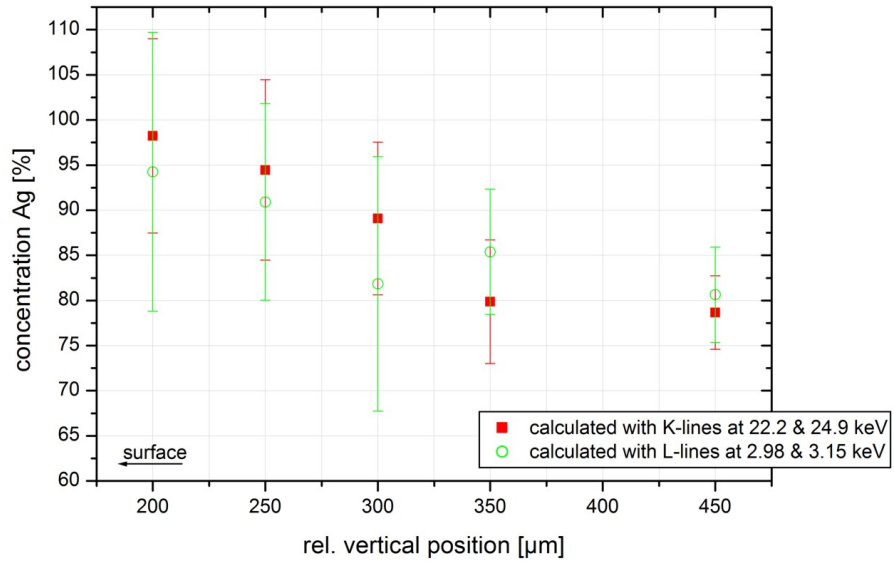


Figure 5.7: Cross-section line-scans of Traian coin no. 34, the matrix elements Ag & Cu are assumed to be together a 100% of the content.

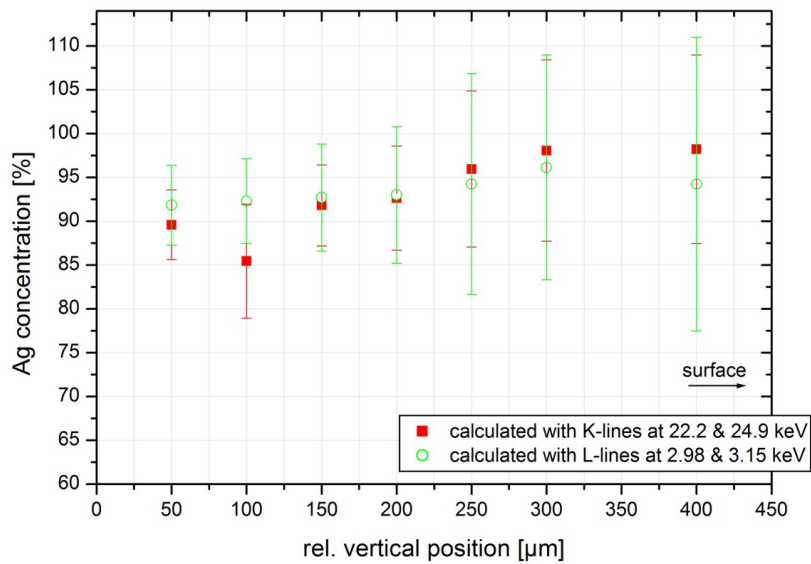


Figure 5.8: Cross-section line-scans of Traian coin no. 41, the matrix elements Ag & Cu are assumed to be together a 100% of the content.

5.3.3 Ottoman Empire coins

In table 5.4 and figure 5.9 the results of PIXE at VERA in comparison to the data achieved at the Louvre laboratories in Paris are given. Following, the deviations of the two measurement series are: Ag ($2.1 \pm 0.4\%$), Cu ($1.0 \pm 0.2\%$), Au ($0.18 \pm 0.09\%$) and Pb ($0.5 \pm 0.3\%$) and relative to each reference value: Ag ($2.2 \pm 0.5\%$), Cu ($20 \pm 3\%$), Au ($45 \pm 45\%$) and Pb ($40 \pm 54\%$) respectively. Although the original concentration values seem to be more spread around the reference value than the relative variations indicate, the weighted average calculation implies that the value with the smallest deviation also shows the smallest error.

coin #	V Ag	L Ag	V Cu	L Cu	V Pb	L Pb	V Au	L Au
31138	95.3 ± 0.5	94.8	2.8 ± 0.1	3.83	1.5 ± 0.2	0.98	0.7 ± 0.1	0.25
31147	93.4 ± 0.5	92.07	4.7 ± 0.3	6.2	1.9 ± 0.3	1.47	-	0.19
31054	95.0 ± 0.4	94.81	3.1 ± 0.1	3.91	1.4 ± 0.3	0.73	0.5 ± 0.1	0.46
31050	94.5 ± 0.7	95.03	3.3 ± 0.3	3.98	1.9 ± 0.1	0.65	0.8 ± 0.1	0.19
31137	93.1 ± 0.1	95.04	3.7 ± 0.3	4.0	2.3 ± 0.25	1.55	0.95 ± 0.1	0.31
31133	90.6 ± 0.2	94.2	5.9 ± 0.3	5.59	3.5 ± 0.2	0.63	-	0.16
31128	93.2 ± 0.5	94.09	4.5 ± 0.4	4.9	1.9 ± 0.1	0.66	0.7 ± 0.1	0.22
31121	94.1 ± 0.8	92.47	5.8 ± 0.8	6.48	-	0.44	-	0.3
31124	86.4 ± 0.3	84.87	11.2 ± 0.2	13.21	1.7 ± 0.1	1.27	0.7 ± 0.1	0.39

Table 5.4: Element concentrations of the Ottoman Empire coins, comparison of the results achieved at VERA and the measurements performed at the Louvre laboratories in Paris, V = measured at VERA, L = measured at the Louvre, all values in %.

The symbol - indicates that this element could not be found in the measured spectra.

A negative aspect of the recently performed PIXE measurements is the low detection probability for trace elements in the ppm region. Elements, which could be measured with the PIXE-setup at the Louvre laboratory, such as Bi, Zn, Sb, As, Fe, and Sn could not sufficiently detected for concentration analysis. Hence, an acquisition time of 300 seconds was too short. Moreover, the large error bars are due to proton-current instabilities.

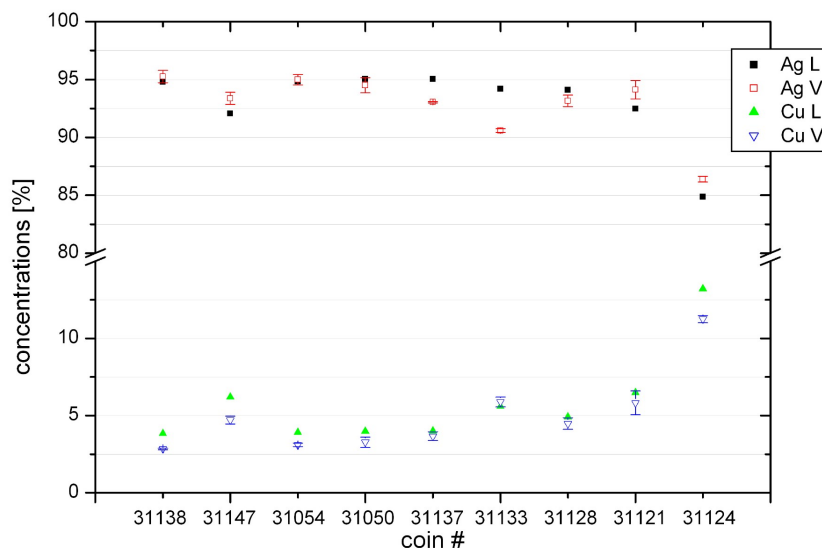


Figure 5.9: Comparison of Ag and Cu content in the Ottoman coins. V = PIXE results from VERA, L = PIXE results from Louvre.

5.3.4 Iridescent glass samples

For the iridescent glass samples typical concentration analysis, of the in the spectra visible elements, has been evaluated. The results are given in the tables 5.5, 5.6 and 5.7. For the calculations also invisible elements have been considered. GUPIXWIN offers the possibility for including elements which appear in molecular compounds. Thus, the following compounds are used: K_2O , MnO, FeO, Cu_2O , ZnO, SnO_2 , CoO, PbO, CaO, Cr_2O_3 . Still, there is one main matrix element missing, Si, which cannot be detected because of the detection limit for low energy X-rays in an external PIXE-setup. Therefore, the here given percentage values are only relative to each other and are not absolute. With these results some simple facts could be shown. In the case of the Loetz glass the bulk material shows a very low Pb content compared to the Tiffany sample, where Pb is the most prominent element. Here, only the surface region shows a lower value. Inversely behaves the surface of Loetz, where the light colored part has a strongly increased Pb content in comparison to the bulk material (see figure 5.10). Moreover the light-blue color has a decreased Ca level and shows as single layer Ag concentrations. The dark bits at the front side represents almost pure bulk material, which could be proved by the similar results of measuring points at the front-side-dark and the back-side. Furthermore no Sn could be found in the corresponding spectra. For both glass samples, Loetz and Tiffany, Sn is only present at the front side. It indicates to be responsible for the iridescent effect layer. All

this properties of iridescent art nouveau glasses are in accordance with the reference papers (e.g [23]).

To gather information about the thickness of the front layer, measurements with a polycapillary optic were performed. The outcome of this experiments is described in the section below (section 5.4).

Sample Glass 232 was firstly measured at the external PIXE facility of VERA. The following properties of this samples could be determined. The three different colors of the surface show distinctive element concentrations and combinations. The brown layer includes no Cr, but a higher Fe and Cu content as well as a low Zn concentration seems to be responsible for the color. The results of the blue and green part exhibit a slightly higher Fe content than the bulk material.

	K [%]	Cr [%]	Mn [%]	Fe [%]
front brown	3.8 ± 0.2	-	0.33 ± 0.02	6.43 ± 0.09
front blue	4.4 ± 0.3	0.52 ± 0.03	0.83 ± 0.04	1.64 ± 0.05
front green	4.0 ± 0.3	0.36 ± 0.02	1.01 ± 0.04	1.99 ± 0.06
back	5.9 ± 0.3	0.61 ± 0.04	1.01 ± 0.05	0.60 ± 0.04
	Cu [%]	Zn [%]	Sn [%]	Pb [%]
front brown	1.44 ± 0.03	0.14 ± 0.01	17.2 ± 0.7	58.6 ± 0.5
front blue	0.10 ± 0.01	-	21.4 ± 0.8	58.9 ± 0.6
front green	0.12 ± 0.01	-	23.8 ± 0.9	56.1 ± 0.6
back	0.10 ± 0.01	-	13.3 ± 0.8	67.7 ± 0.7

Table 5.5: Element concentrations in **Glass 232** for different measuring points.

	K [%]	Ca [%]	Fe [%]	Co [%]
front light	23.6 ± 0.6	6.2 ± 0.4	0.20 ± 0.02	0.18 ± 0.03
front dark	32.6 ± 0.6	27.0 ± 0.6	0.34 ± 0.03	0.66 ± 0.05
back	31.7 ± 0.6	19.5 ± 0.5	0.21 ± 0.03	0.42 ± 0.04
	Ag [%]	Sn [%]	Pb [%]	Cr [%]
front light	9.7 ± 0.8	14.6 ± 1.3	31.1 ± 0.6	-
front dark	-	-	6.6 ± 0.3	0.32 ± 0.03
back	-	-	3.6 ± 0.2	-

Table 5.6: Element concentrations in **Loetz Glass sample** for different measuring points.

5 Determination and verification of elemental concentrations

	K [%]	Mn [%]	Co [%]	Cu [%]
front pos.1	4.8 ± 0.2	0.56 ± 0.02	0.72 ± 0.02	0.05 ± 0.01
front pos.2	4.2 ± 0.2	0.50 ± 0.02	0.67 ± 0.02	0.08 ± 0.01
surface	9.1 ± 0.2	0.77 ± 0.02	0.84 ± 0.02	0.05 ± 0.01
back	5.9 ± 0.31	0.74 ± 0.04	0.91 ± 0.04	0.06 ± 0.01

	Zn [%]	Ag [%]	Sn [%]	Pb [%]
front pos.1	0.04 ± 0.01	10.2 ± 0.7	10.4 ± 0.5	63.4 ± 0.5
front pos.2	0.04 ± 0.01	10.6 ± 0.7	9.5 ± 0.5	64.9 ± 0.5
surface	0.05 ± 0.01	9.6 ± 0.5	14.3 ± 0.5	54.2 ± 0.4
back	0.07 ± 0.01	10.3 ± 1.0	-	73.8 ± 0.7

Table 5.7: Element concentrations in **Tiffany Glass sample T10** for different measuring points, front pos.1 and 2 were excited with an angle normal to the target surface, at the position with the description "surface" the sample was turned by almost 90 degrees to produce an grazing incidence angle.

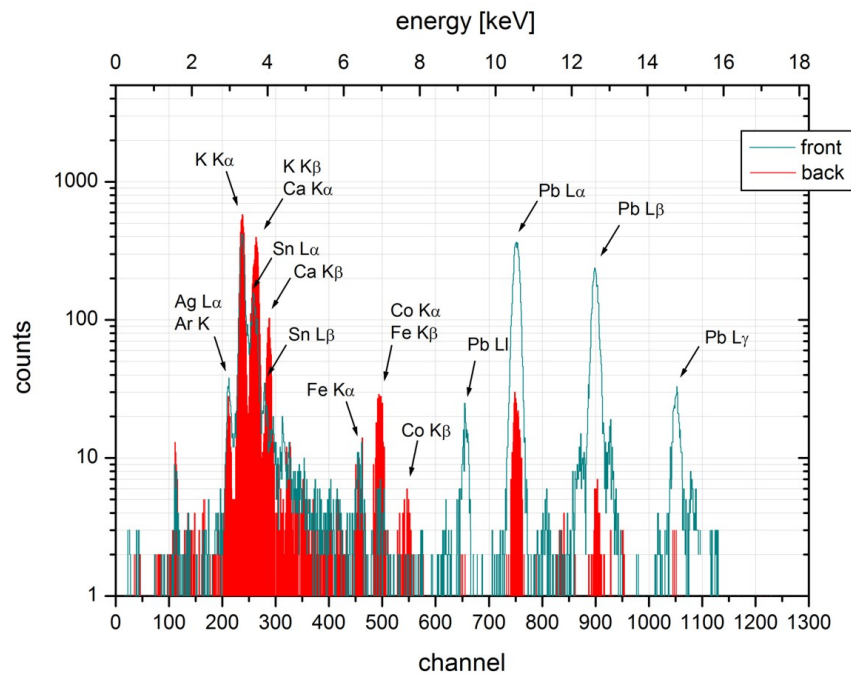


Figure 5.10: Comparison of spectra taken from the front (light spot) side and back side of the Loetz glass sample.

5.4 Possibilities with the use of Polycapillaries

Analyzing precious art object with polycapillary optics introduces a series of advantages. First of all, layered objects would not need to be prepared. If the front layer thickness is less than the penetration maximum of the incident protons, this method could avoid the need of cross-sections. Furthermore, because no additional filter in front of the detector is necessary, lower X-ray energies can be detected. Hence, lighter elements can be measured (see 5.12). This is also due to the greater sensitivity of polycapillaries in the low energy region.

But, first measurements did show difficulties, which are discussed in the sections below.

5.4.1 Determination of concentrations

The evaluation of concentrations and the simulation of experimental data respectively, from measurements gained with the use of polycapillary optics is a rather complex undertaking. The concept gets even more sophisticated if the elements are mixed and present in more than one layer, or a gradient in concentration exists. First approaches in simulating experimental gained data were carried out with the use of additional element analysis methods [19]. Furthermore Sokaras et al. [33] presented recently, first results on a theoretical description of 3D Micro-PIXE intensities for layered materials. The system that has to be described consists of an analytical description of the detection volume, including the beam profile and the spatial extensions of the focal "tube" of the polycapillary optic depending on the energy. Further, all known processes that are connected with the X-ray production and detection in PIXE-analysis, such as ionization cross-sections, stopping power, fluorescence yields and self-attenuation, have to be implemented by a convolution with the sensitivity function.

5.4.2 Measurements and Results

Despite the fact that the calculation of concentrations are not included yet, some measurements with the above used samples have been performed to gain knowledge about the possibilities and limits of the method.

Coin samples

The linescan for the cross-section of the Traian coin number 34 was remeasured with the use of the Poly-CCC in front of the Si(Li) detector. The plot 5.11 shows the peak intensity relations between Ag and Cu in a scan over the whole cross section area. An increase in the silver concentration in the regions of the surfaces is visible.

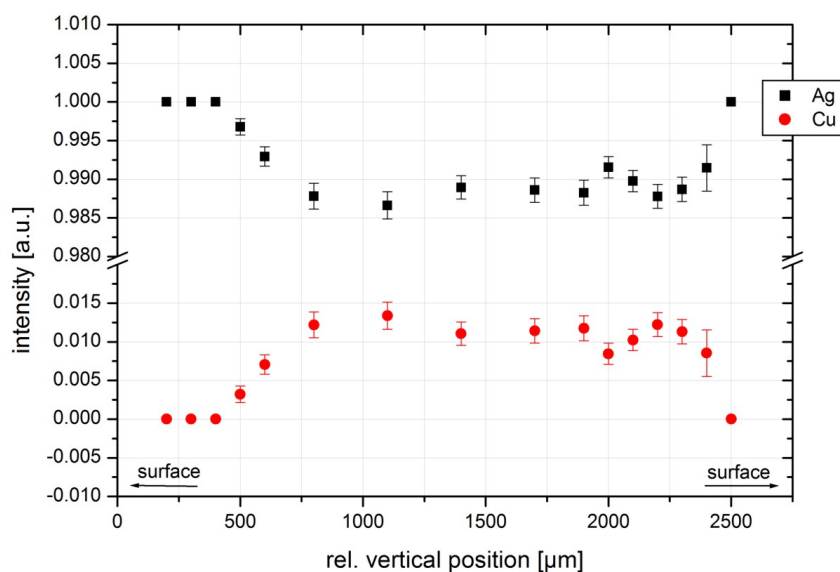


Figure 5.11: Line-scan of the cross-section polish of Traian coin number 34, performed with the Poly-CCC.

Iridescent Glasses

With the use of a Poly-CCC the elements of a surface layer are privileged against the bulk material. This circumstance can be used for analyzing the front layer of iridescent glass samples. In figure 5.12 the spectra gained with and without a polycapillary optic in the detection channel are compared for the Tiffany sample T10, measured from the front side. The both spectra complement one another with one spectrum covering the middle to the high energy range and the other showing the best results in the low energy region. The Poly-CCC is extremely sensitive for low energy X-rays and is therefore suited for detecting elements in the range of $Z = 14-20$, but also higher Z with L or M lines in that same energy region, e.g. Ag L, Sn L, Pb M,... Concluding, only elements with a middle Z , that are only present with less than one percent in the content of the target or are even only trace elements, are difficult to

detect with the use of the Poly-CCC.

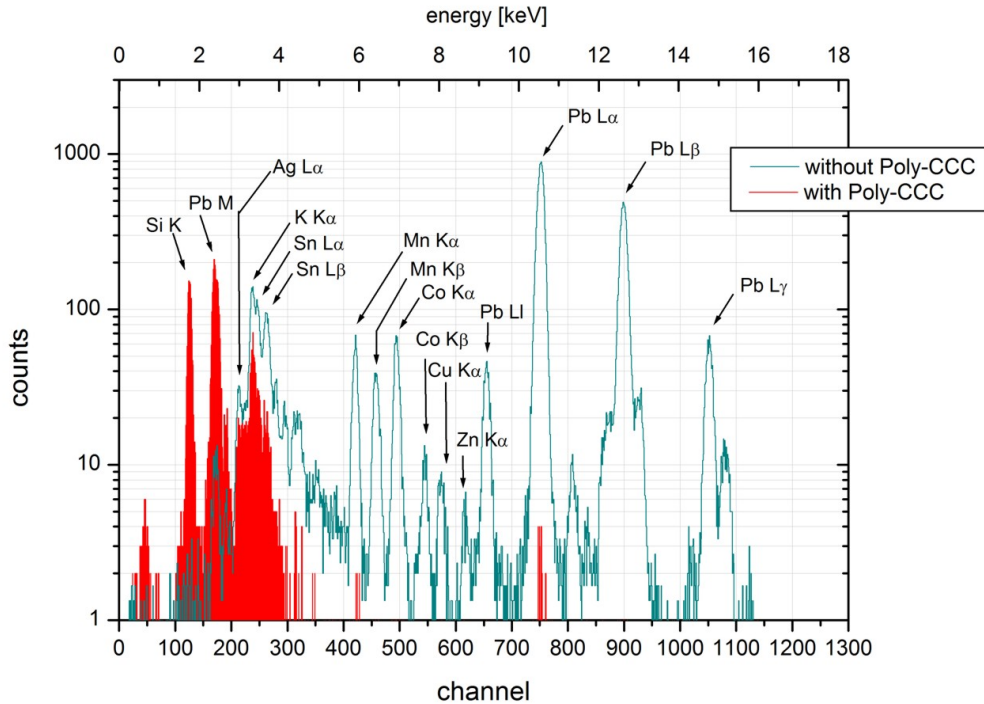


Figure 5.12: Spectra taken from the surface side of the Tiffany sample T10 in comparison with the same measurement performed with the Poly-CCC in front of the Si(Li).

In addition, to test depth resolving abilities of polycapillaries a depth profiling scan of the Loetz glass sample was carried out (see figure 5.13). As already mentioned above, the surface layer is privileged in those spectra. Therefore, comparing the measured Si, which refers to the bulk material to the other visible component in the spectrum, a difference in the localization in the target can be observed. In agreement with the measurement of the back and front side of the Loetz glass - the Ag part corresponds to a layer on the surface. Also the Pb content is highly increased in the front layer and therefore the center of the Gaussian fit is situated before the Si maximum. The sequence of layered elements could be evaluated.

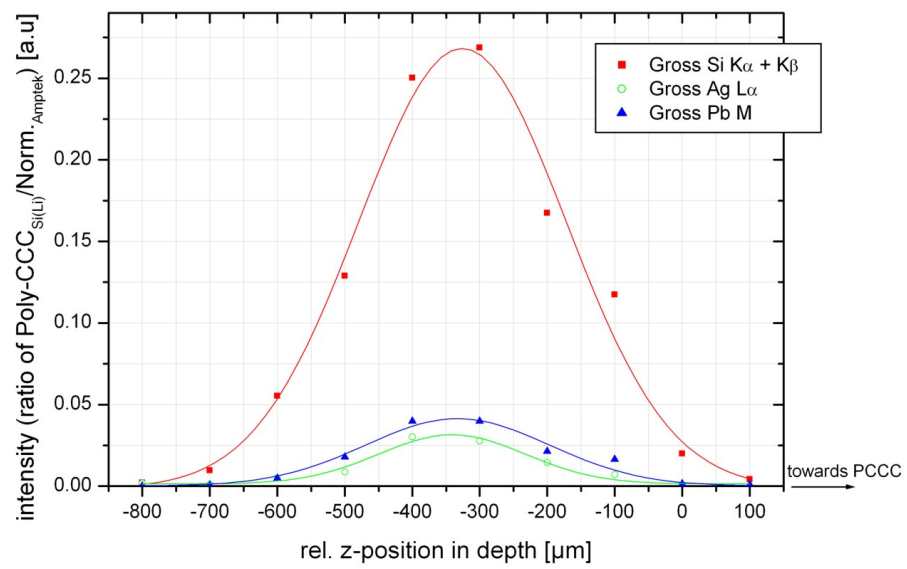


Figure 5.13: Depth scan of Loetz Glass sample measured at a light colored surface spot.

6 Conclusion and Outlook

PIXE suffers from a lack of depth-resolved quantification. This may be overcome by additional measurements either with the sample mounted in different geometries or with the use of different proton energies (so-called differential PIXE). In any case such a procedure increases the irradiation dose on the sample, which is always not practicable for precious objects. When depth information is indispensable, another ion beam technique, Rutherford back scattering (RBS), may be employed in favorite cases (heavy elements in a light matrix). The use of polycapillary optics in the detection channel of a PIXE-setup offers another and rather recent possibility for depth-resolved elemental analysis. It adopts the idea of confocal micro-XRF [16]. Instead of the exciting X-ray beam the proton beam is used. Depth information comes from mechanically moving the sample through a small detection volume. At VERA the initial idea came from the wish to separate X-ray signals from the drawing surface and the preparation layer or the support material [20]. In the course of the present thesis polycapillaries turned out to be useful not only in this case but more generally for layered structures with very well defined interfaces. Ideally suited are samples with individual elements only present in one specific, separated layer. This has been verified with artificially prepared foil sandwiches (see below). If samples are infinitely thick, polycapillaries help to provide qualitative depth information. For quantitative information in thick samples a fully developed data simulation is required which must be supported by excessive knowledge of experimental parameters.

In this work three different types of polycapillary optics have been characterized to gain knowledge about the detailed behavior of the detection volume under the experimental conditions at VERA (in particular the proton beam profile and the detection setup). For this purpose an artificial foil sandwich, consisting of single element foils, was developed. The size of the sensitive volume as function of X-ray energy was determined. The FWHM of the depth scans vary for the half-lens 22 mkl06 between approx. 219 and 204 μm (4.5 to 9 keV), for the lens 73 mls08 between approx. 961 and 393 μm (4.5 to 11.5 keV) and for the Poly-CCC 71mls-PCCC14 between approx. 377 and 180 μm (2 to 11.5 keV), respectively. It should be noted that the polycapillaries were not only different in shape but also in internal construction (different number and different size of individual capillaries). Values of transmission in the energy region 6.5 - 9 keV relative to the simultaneously measured data in a normalizing detector (Amptek; solid angle 0.08 sr), go from 4.4 to 2.4 % in the case of the half-lens, from 25.2 to 29.5 % for the lens and from 42.0 to 16.3 % for the Poly-CCC, respectively. Clearly, the transmission and the size of the sensitive volume

are interrelated. The ability to gain depth information better than the values above depends on the possibility to perform centroid analysis of the depth profile scans. Optimally, depth resolution can be as good as some μm . It is easy to conceive that the ability to enhance the signals from the surface relative to the bulk can always be realized by locating the sample surface at the margin of the detection volume. Thus, polycapillaries with high transmission, i.e. Poly-CCC are perfectly suited for PIXE analysis of drawings.

Future challenges are the development of simulations to evaluate infinitely thick samples and to deconvolute layered targets with mixed elements (e.g. an element is present in more than one layer). There is also room for improvement for basic PIXE analysis at VERA, especially stabilizing the position of the incident proton beam and measuring the extracted proton fluence would be of great importance. When in the course of this thesis the setup at VERA was assessed for consistency with results measured at other facilities, no systematic deviation was found. However, for major elements the error in concentration may be up to 2 % mainly because of the above reasons.

A Appendix

A.1 Depth scans of foil sandwiches

In this part depth scans performed with different polycapillary optics are listed by foil composition and inter-foil separation to characterize the features of the individual glass optics. The number in brackets in each plot title describes the thickness of the foil. The first entry corresponds to the front foil. The relative z -position equals the position of the sandwich relative to the proton exit window. The z -movement is in the direction of the proton beam. The position $z=0$ in each plot may not be taken absolute because of uncertainties during mounting and demounting of the various foils. However, the zero position is always close to the surface due to the positioning procedure of the polycapillary optics.

A.1.1 Cu-Ti

The first foil (the one closer to the nozzle) is a $7\ \mu\text{m}$ thick copper foil. The second is a $10\ \mu\text{m}$ thick titanium foil. The distances between these foils vary from $0\ \mu\text{m}$ to $200\ \mu\text{m}$.

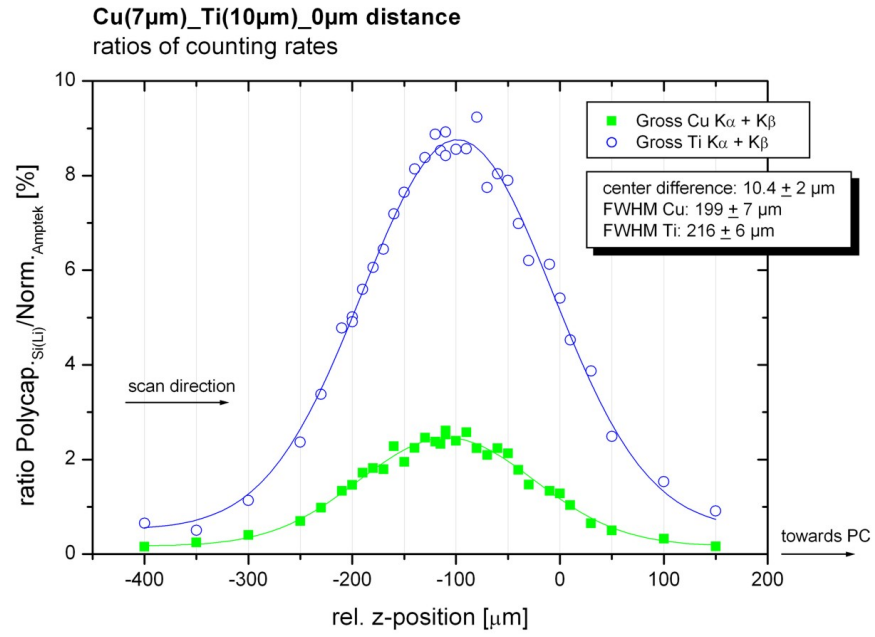


Figure A.1: Depth scan of Cu-Ti sandwich measured with **half-lens 22mk106**. The green rectangles indicate the Gross counts from Cu K α + Cu K β . The FWHM and the difference of the center values are given in the insert.

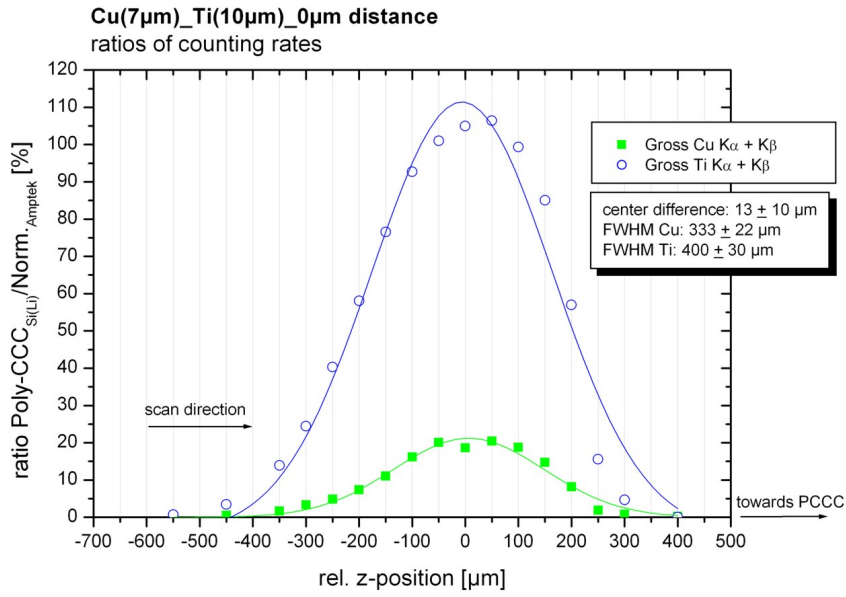


Figure A.2: Depth scan of Cu-Ti sandwich measured with **Poly-CCC 71mls**.

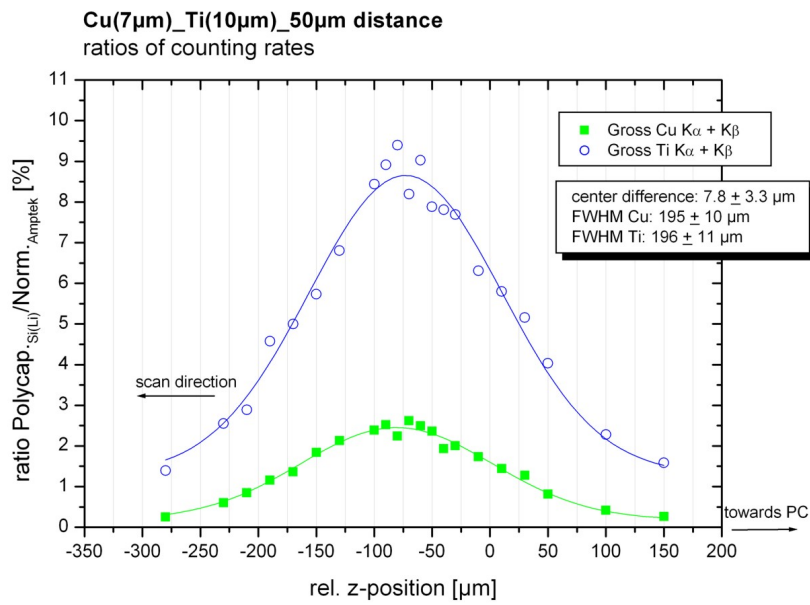


Figure A.3: Depth scan of Cu-Ti sandwich measured with **half-lens 22mk106**.

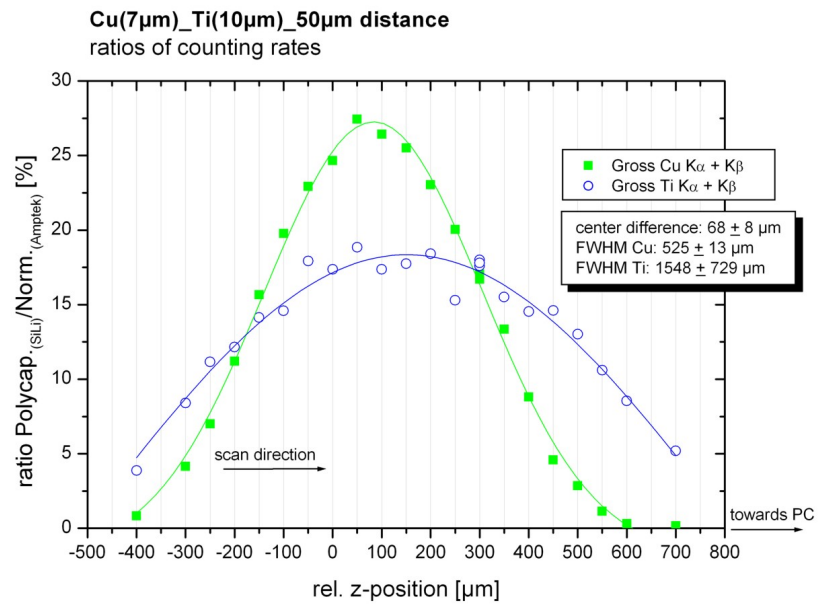


Figure A.4: Depth scan of Cu-Ti sandwich measured with lens 73mls08.

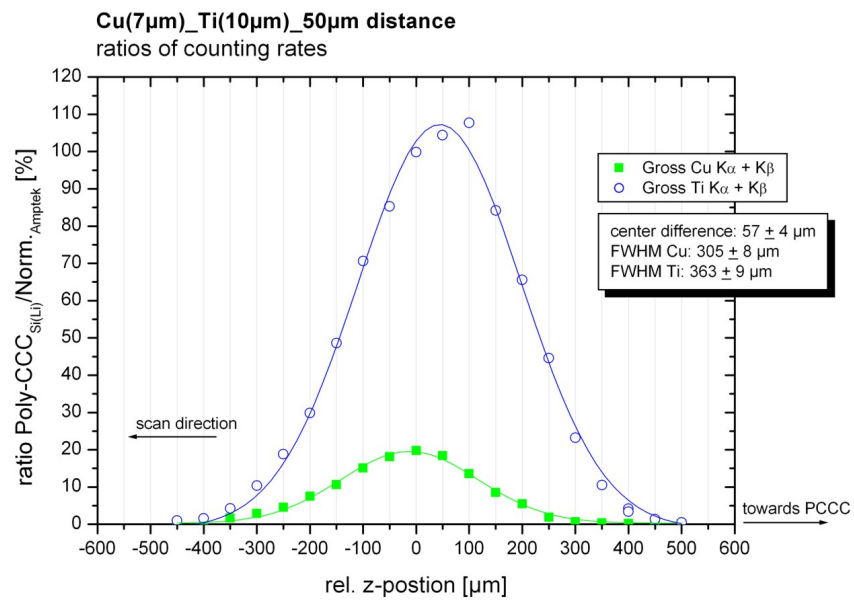


Figure A.5: Depth scan of Cu-Ti sandwich measured with Poly-CCC 71mls.

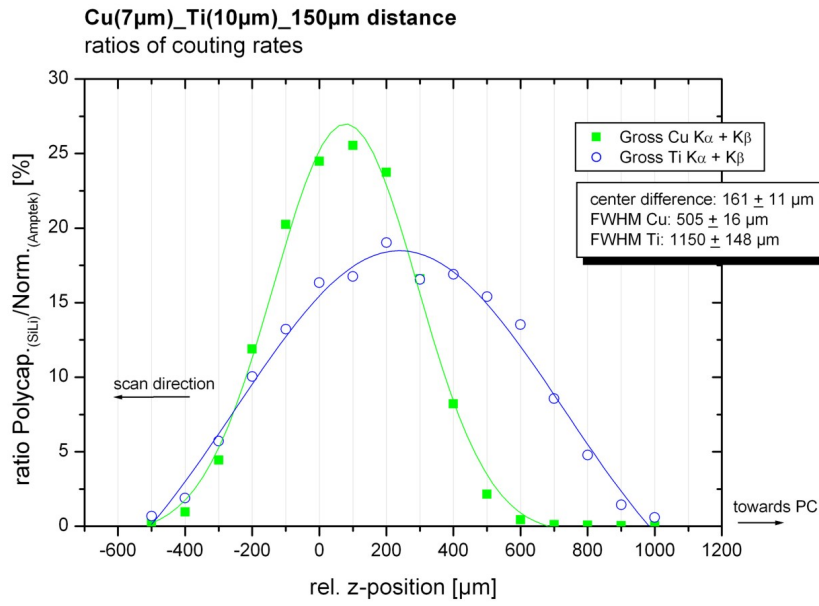


Figure A.6: Depth scan of Cu-Ti sandwich measured with lens 73mls08.

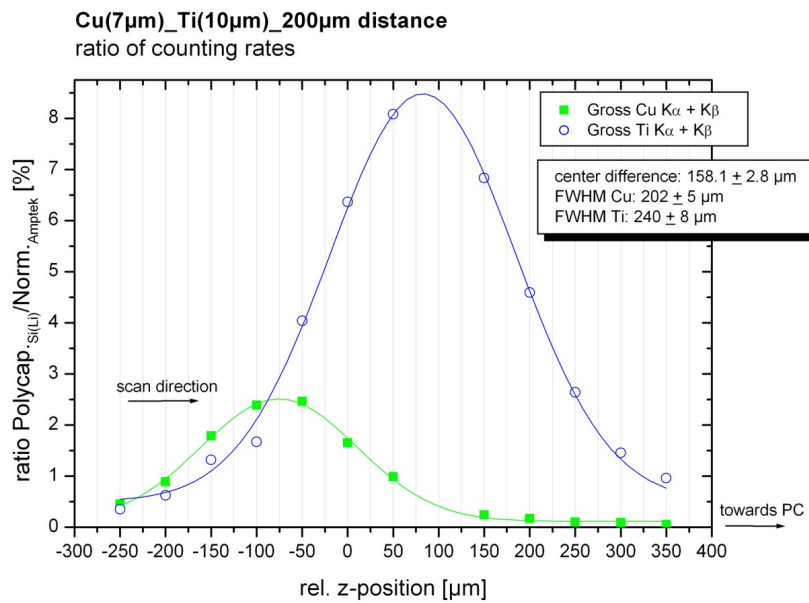


Figure A.7: Depth scan of Cu-Ti sandwich measured with half-lens 22mkl06.

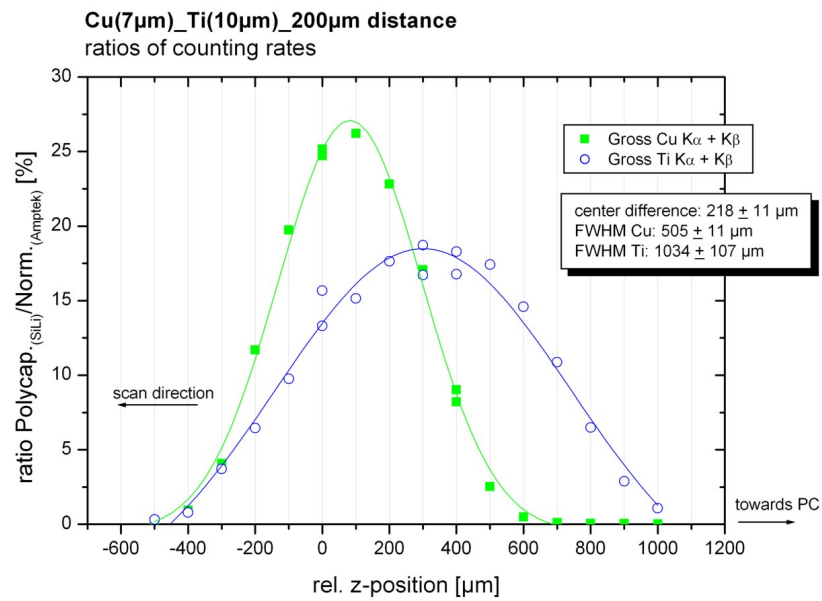


Figure A.8: Depth scan of Cu-Ti sandwich measured with lens 73mls08.

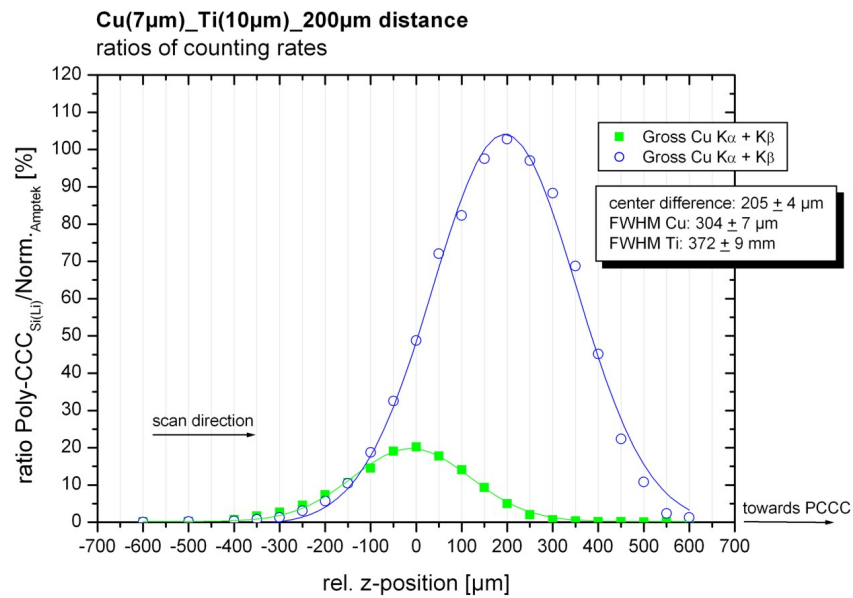


Figure A.9: Depth scan of Cu-Ti sandwich measured with Poly-CCC 71mls.

A.1.2 Fe-Cu

The first foil (the one closer to the nozzle) is a 3 μm thick iron foil. The second is a 7 μm thick copper foil. The distances between these foils vary from 30 μm to 300 μm .

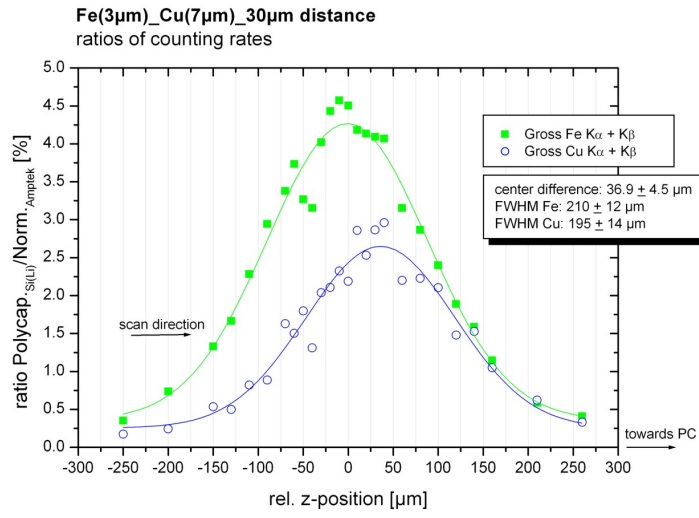


Figure A.10: Depth scan of Fe-Cu sandwich measured with half-lens 22mkl06.

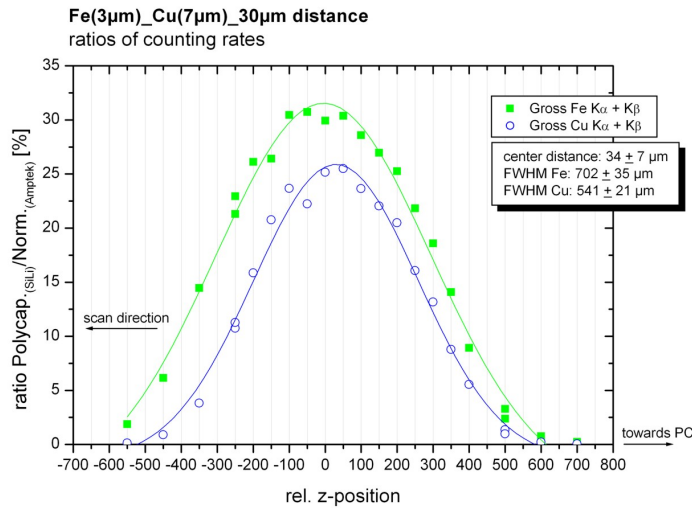


Figure A.11: Depth scan of Fe-Cu sandwich measured with half-lens 73mls08.

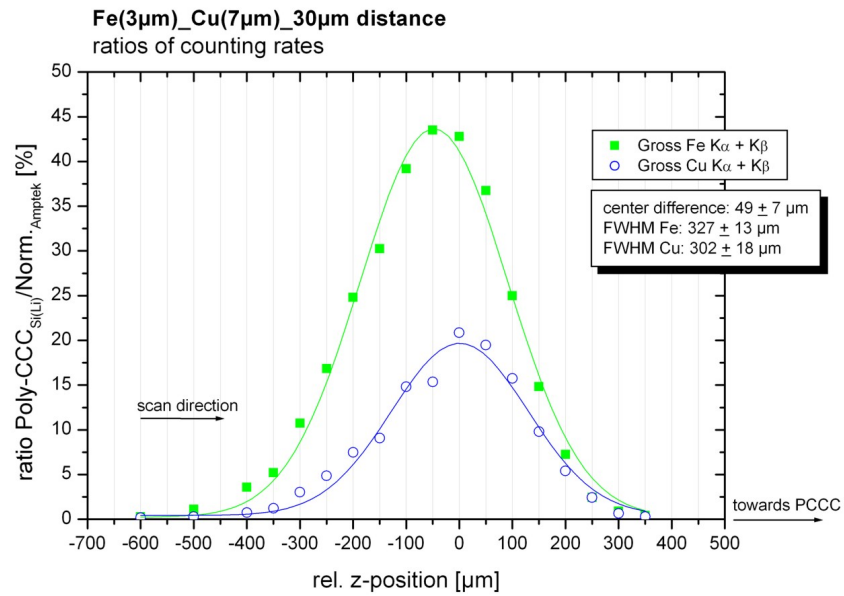


Figure A.12: Depth scan of Fe-Cu sandwich measured with **Poly-CCC 71mls**.

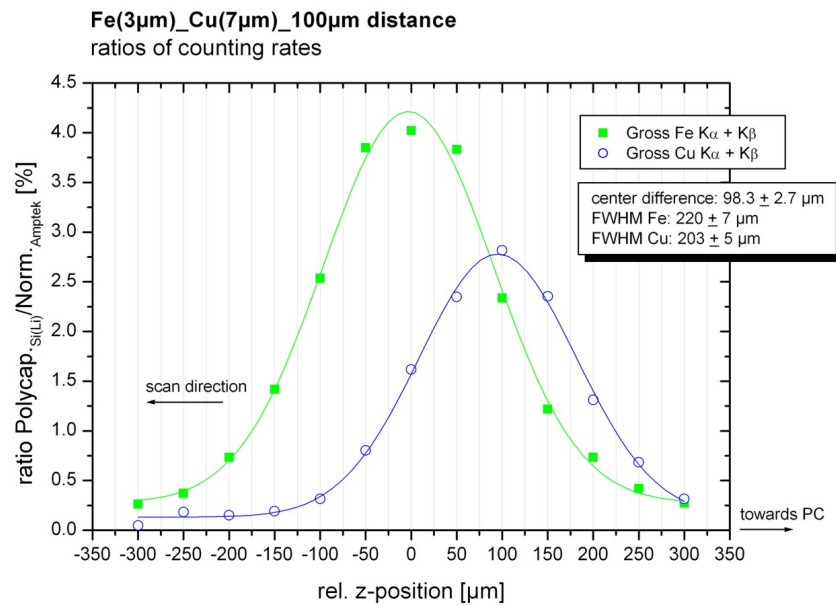


Figure A.13: Depth scan of Fe-Cu sandwich measured with **half-lens 22mk106**.

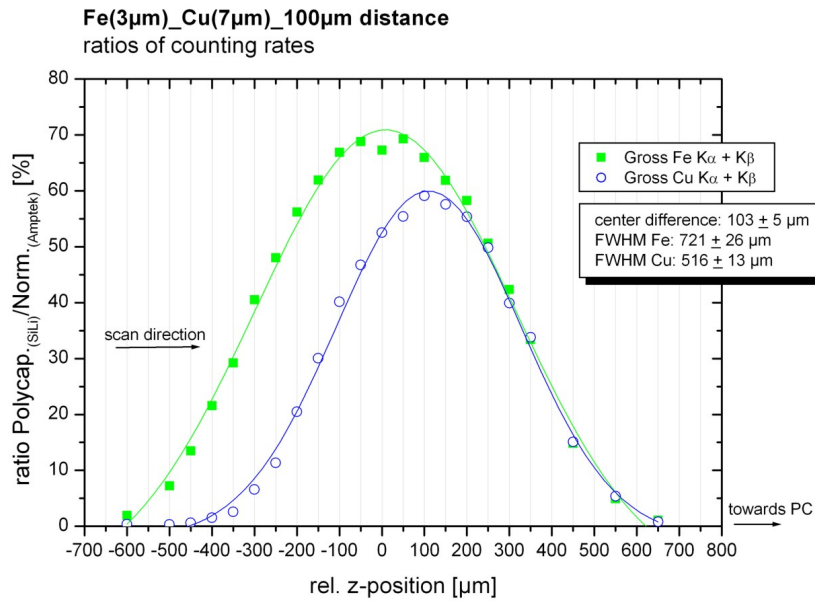


Figure A.14: Depth scan of Fe-Cu sandwich measured with lens 73mls08.

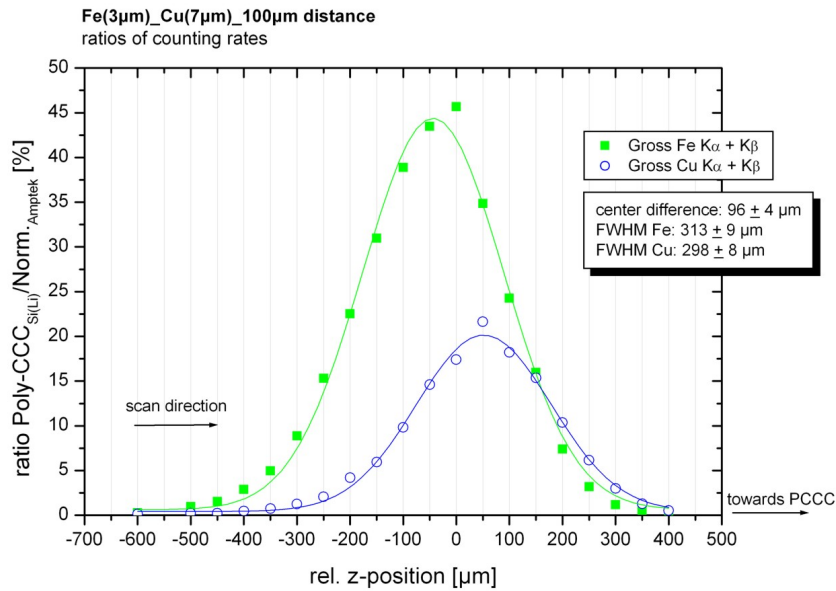


Figure A.15: Depth scan of Fe-Cu sandwich measured with Poly-CCC 71mls.

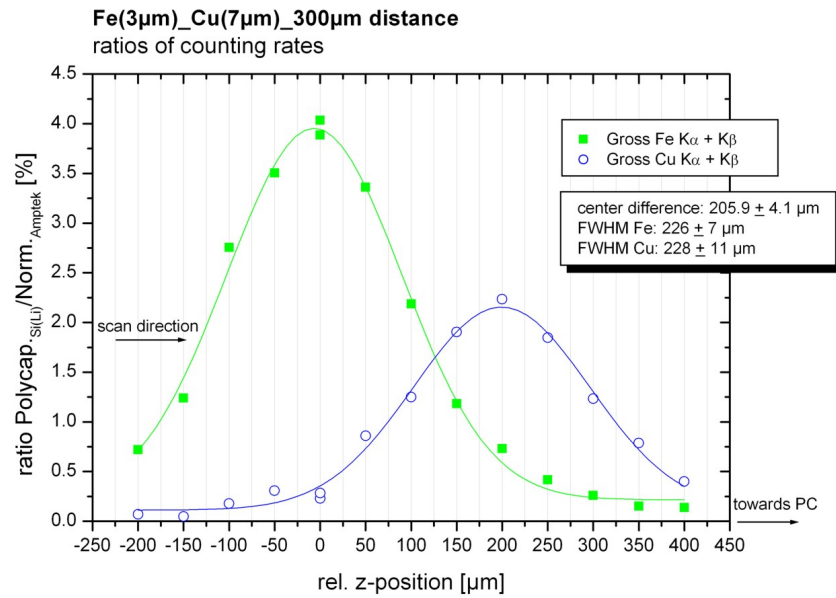


Figure A.16: Depth scan of Fe-Cu sandwich measured with **half-lens 22mkl06**.

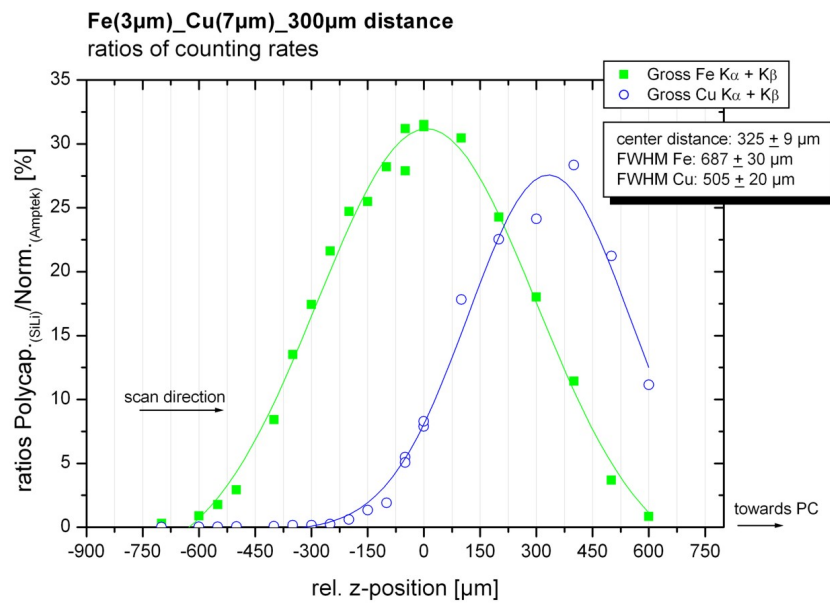


Figure A.17: Depth scan of Fe-Cu sandwich measured with **lens 73mls08**.

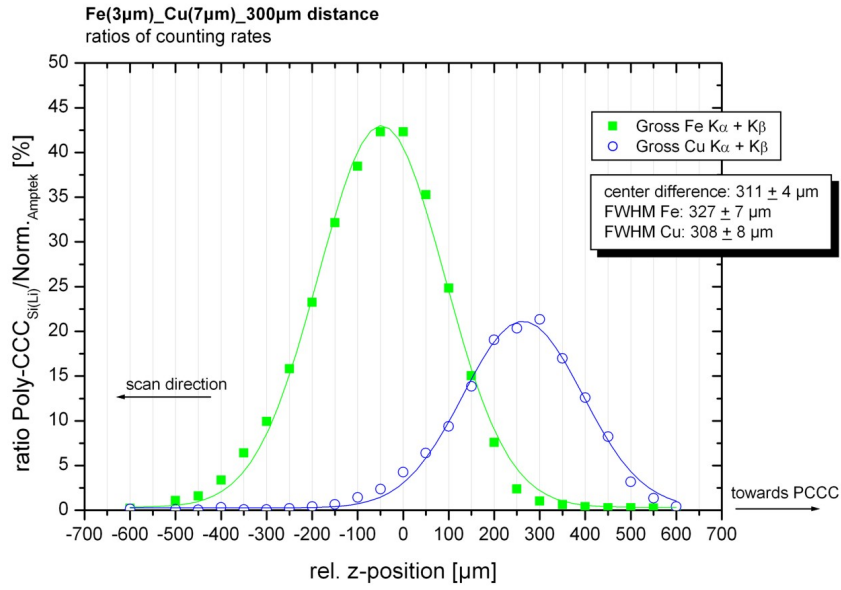


Figure A.18: Depth scan of Fe-Cu sandwich measured with Poly-CCC 71mls.

A.1.3 Fe-Au

Here both possible combination of the foils are presented. In the first case the front foil is 3 μm thick iron followed by a $\approx 20 \mu\text{m}$ thick gold foil. In the second case the first foil is a beaten gold layer of $\approx 4 \mu\text{m}$ and the back one is a 3 μm thick iron foil. The distances between these foils vary from 0 μm to 100 μm .

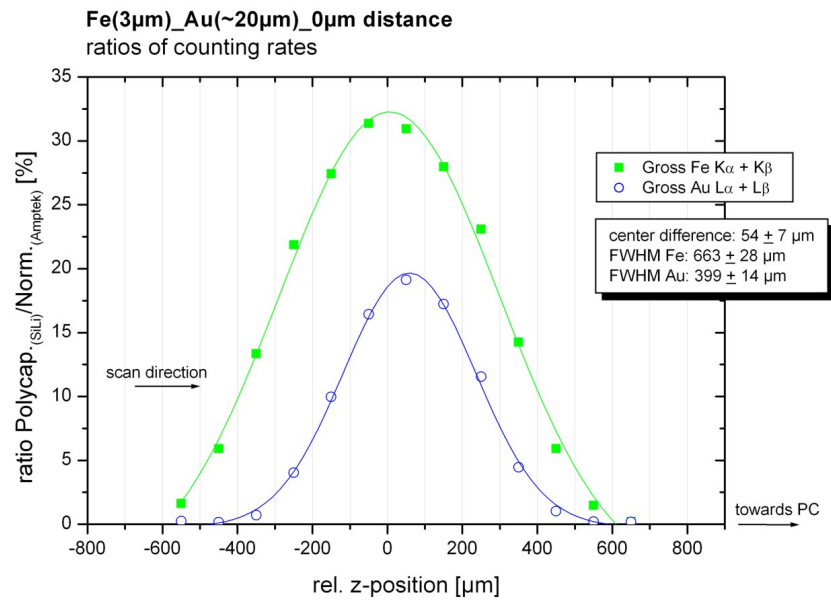


Figure A.19: Depth scan of Fe-Au sandwich measured with lens 73mls08.

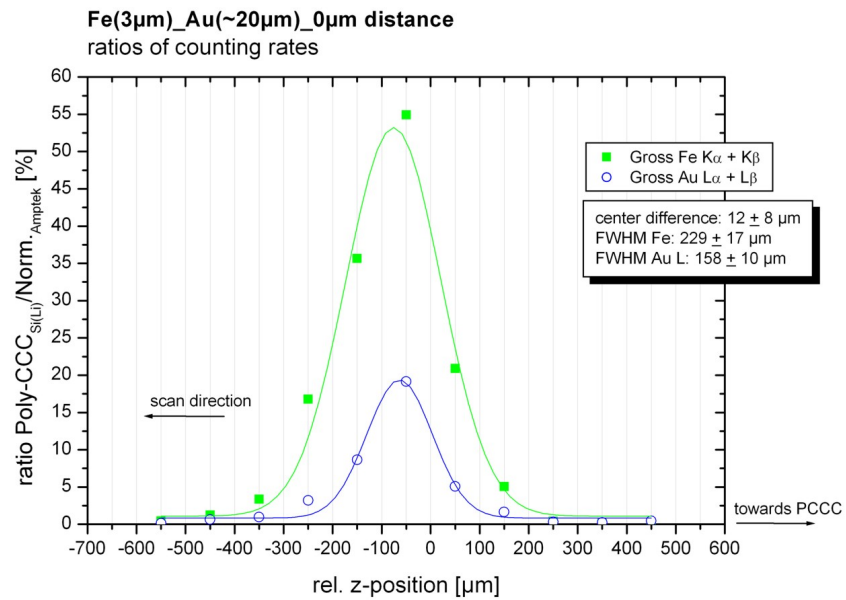


Figure A.20: Depth scan of Fe-Au sandwich measured with Poly-CCC 71mls.

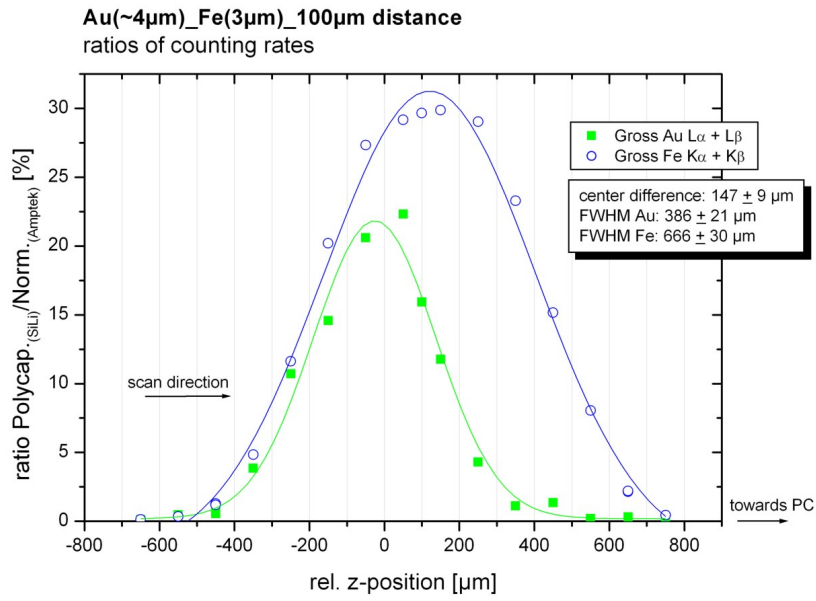


Figure A.21: Depth scan of Au-Fe sandwich measured with lens 73mls08.

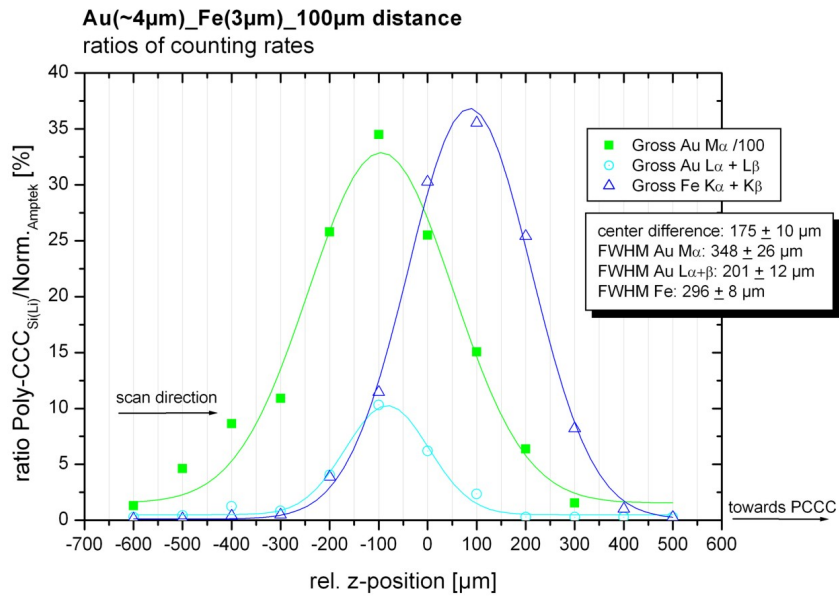


Figure A.22: Depth scan of Au-Fe sandwich measured with Poly-CCC 71mls.

A.1.4 Ti-Fe

The first foil (the one closer to the nozzle) is a 10 μm thick titanium foil. The second is a 3 μm thick iron foil. The distance between these foils equals 0 μm .

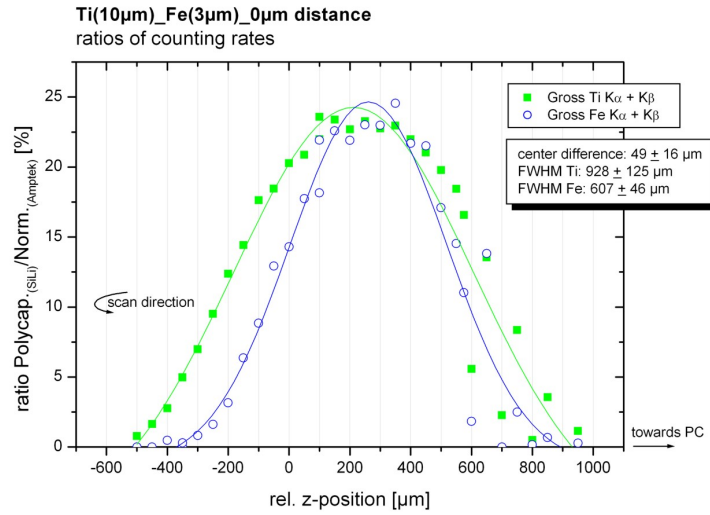


Figure A.23: Depth scan of Ti-Fe sandwich measured with lens 73mls08.

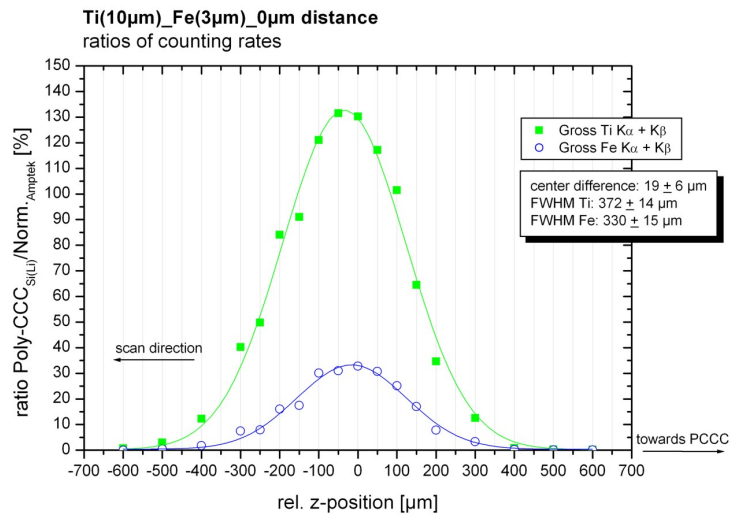


Figure A.24: Depth scan of Ti-Fe sandwich measured with Poly-CCC 71mls.

Notes:

The visible offset of the Gaussian-curve-centers in the scans with zero distance between the foils (A.1, A.2, A.19, A.20, A.24, A.23) is due to non-negligible foil thickness. This effect is strongly pronounced in the case of the Fe-Au sample, because of the 20 μm thick gold layer.

Some plots with polycapillary half-lens 22mkl 06 show a discrepancy in the measured foil separation as compared to the reference value. In particular this is the case in plot A.3, A.7 and A.16. This behavior is due to the insufficient stiffness of the foil holder during the early times of the experimental work. Therefore, the holder of the second foil, when moved to the position of zero distance, imposed pressure on the first holder. When moving the second backwards again, the first relaxed and moved back to its former place. This led to a smaller distance than expected. For the scans with the Fe-Cu-sandwich A.10 and A.13 this uncertainty was discovered and could be corrected. For the measurements to follow the mounting of the front foil has been improved and the uncertainty eliminated.

B Appendix

B.1 Guiding protons through polycapillary optics

This appendix is not directly related to the topic of the thesis. It describes a project of my own executed with Roman Schütz from the Institute of optics and atomic physics, TU Berlin. It was accomplished at the Vienna Environmental Research Accelerator in August 2008.

B.1.1 Introduction and theoretical considerations

Glass-polycapillary are established in channeling and focusing X-rays. Due to external total reflection a large percentage of incoming X-rays can be lead through the capillary-optics as discussed in chapter 2 of this thesis. These optics are also used as filter for protons prior to entering the detector, particularly when using lens or half-lens structures. Therefore it is assumed that back scattered protons from the target cannot penetrate through the glass-structure. Specifically, even if scattered and reflection processes are neglected, protons are stopped in the walls of the glass capillaries.

Similar experiments involving neutrons have already been conducted [21]. Polycapillary optics have shown high efficiency in controlling thermal neutron radiation. As far as we aware no experimental research focusing on proton behavior in polycapillary-optics has been performed prior to the present date.

The aim of this experiment was to investigate scattering, reflection and total reflection abilities of protons channeled through polycapillary glass optic structures. As a first step it had to be shown that a proton could pass through a capillary without making contact with the walls.

Bernd Aschenbach [2] describes the observation of totally reflected protons with energies of order MeV in his article. Furthermore a theoretical description and calculation of the critical angle of total reflection α for protons is given (see formula B.1) where by μ is the index of refraction, Z the atomic number and V_p the potential of the interacting proton referring to its kinetic energy). Theoretically the angle is of the same order (≈ 1 mrad) as the angles with regard to X-rays. The appearance of proton reflections is possible because of the ability of charged particles to scatter on the inner potential of a material V_0 . The expected total reflexion angle for 3 MeV protons is therefore found to be at approximately $0.1^\circ \cong 1.7$ mrad, which equals the critical angle for characteristic Mo $K\alpha$ X-rays at 17.04 keV ($\cong 1.8$ mrad).

Hence, if the theoretical ansatz is valid and the assumption that the potential of the air-glass transition can be assumed to be similar to that of vacuum-matter transition, $V_0 = 5 - 15V$, then the necessary angles for reflection are in the same region polycapillaries are optimized at.

$$\alpha = \sqrt{2(1 - \mu)} \quad \mu = \sqrt{1 - Z \frac{V_0}{V_p}} \quad (\text{B.1})$$

A factor that prohibits the observed total reflection of protons is the surface roughness of the glass-capillary, which is in the order of $\sigma = 5 \text{ \AA}$. This roughness, although tiny, acts a a great source of unevenness for protons and results in a large scattering angle distribution. The number of protons that are scattered in a forward direction will be drastically reduced.

B.1.2 Measurements and Results

The experiment was carried out at the external PIXE-beam-line at VERA. The beamline-assembly was tuned for 3 MeV protons and utulized a proton current in the order of nA. Hence, around 10^{10} protons per second in air can be estimated to reach the capillary.

Two different types of polycapillary-optics were investigated (see table B.1 and figure B.1). Each of them were situated in the proton beam after the exit window of the nozzle. The mount was constructed such that the capillary could be adjusted 2-dimensionally by changing its tilt angle. For counting the protons a surface-barrier-detector is positioned behind the capillary also in line with the beam direction. The detector is covered with aluminum-foil to avoid background noise induced by incident light. Between the detector and the optic there is a horizontal movable foil, thick enough that protons cannot pass through. It is used in the following for accomplishing the edge scans. A second detector (Si(Li)) points at the area where the protons exit the nozzle and enter the glass-structure. The detected X-ray signal, mostly $K\alpha$ Ar from air but also from the glass material of the capillary itself, is used to normalize the counted proton number. Figure B.2 shows the above described setup.

	51mkl 02 half lens	mkl-84 parallel structure
length	24.6 mm	21.9 mm
diameter parallel side	4.1 mm	5.1 mm
diameter focus side	1.9mm	-
focal length	10 mm	∞

Table B.1: Dimensions of the polycapillary-optics.

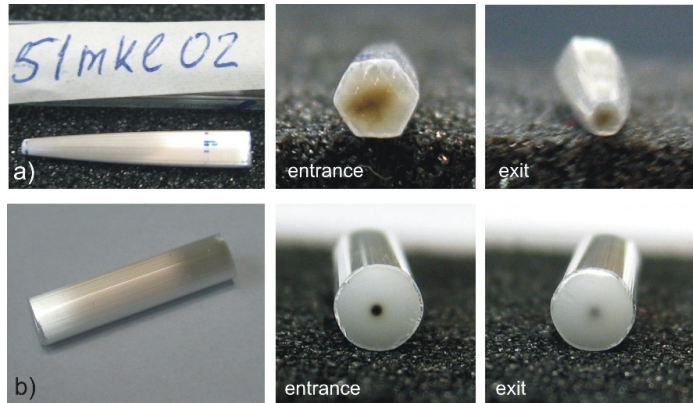


Figure B.1: Photographs of the polycapillary-optics, a) half lens 51mkl 02 , b) parallel structure mkl-84

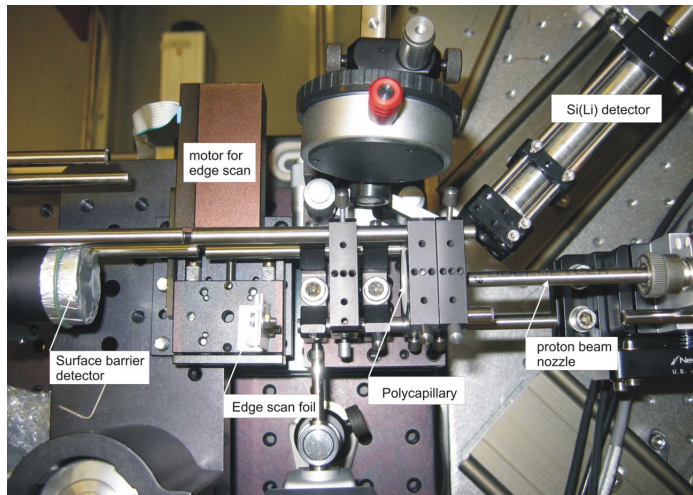


Figure B.2: Setup of proton channeling experiment

Parallel structure mkl-84

For this measurement series the nozzle was swapped to one with a $500 \mu\text{m}$ collimator at the end to provide a higher counting rate and a bigger illuminated spot at the polycapillary entrance.

Before inserting the polycapillary the position of the proton-detector, at which the lowest number of detected protons occurs before being zero was determined. This insures that only unscattered protons are detected. By measuring with inserted polycapillary (after optimizing procedure) at the same detector-nozzle distance the highest proton energy can be compared (see fig. B.3). If the counts reached the same channel number, then the existence of direct protons could be proved. Having a closer look at the two combined spectra it can be seen that the protons that go

through are lower in their energy. But, taking into account that the measured overall suppression of the protons with a capillary present is a factor of 10^6 particle/s, the probability of detecting protons in a high energy channel is very low.

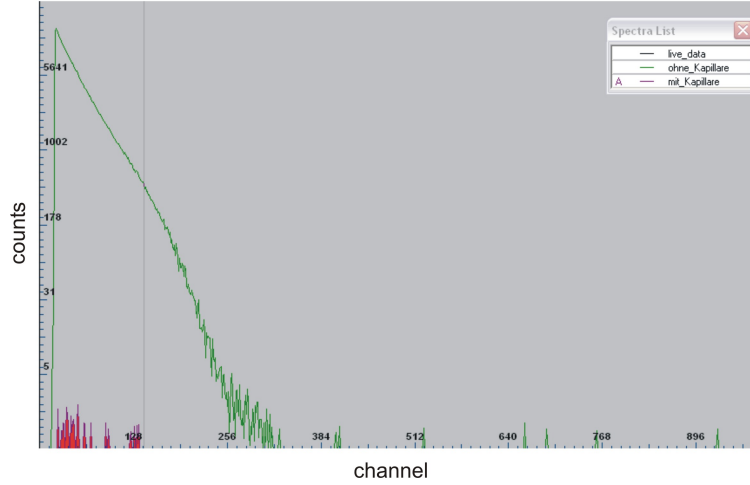


Figure B.3: Detected protons with and without polycapillary at detector position 12.4 cm.

At a distance (proton detector - nozzle) with a reasonably proton counting-rate in the surface-barrier-detector the capillary was adjusted through tilt-angle-scans in two directions (see fig. B.4). After optimizing the position the surface-barrier-detector was moved step by step closer to the capillary and nozzle. The detected counting-rates and selected spectra are given in figure B.5 and B.6. This measurement series was restricted by the maximal allowed counting-rate of 10 000 counts/s.

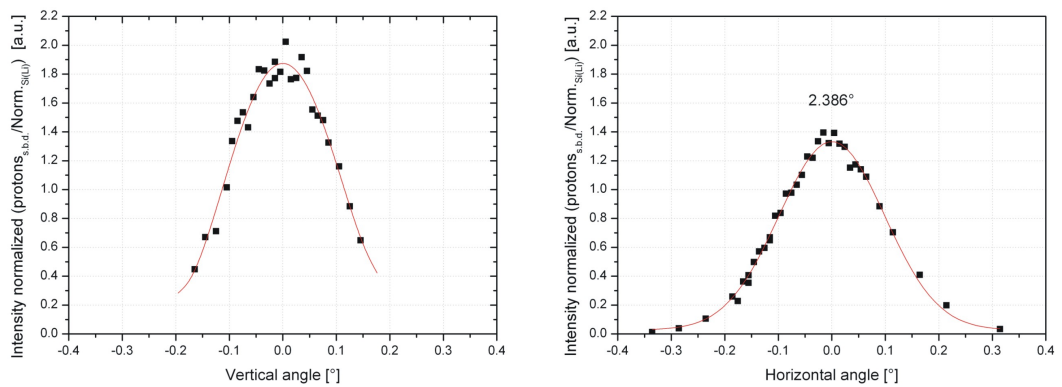


Figure B.4: Angle-adjustment of polycapillary parallel structure mk1-84.

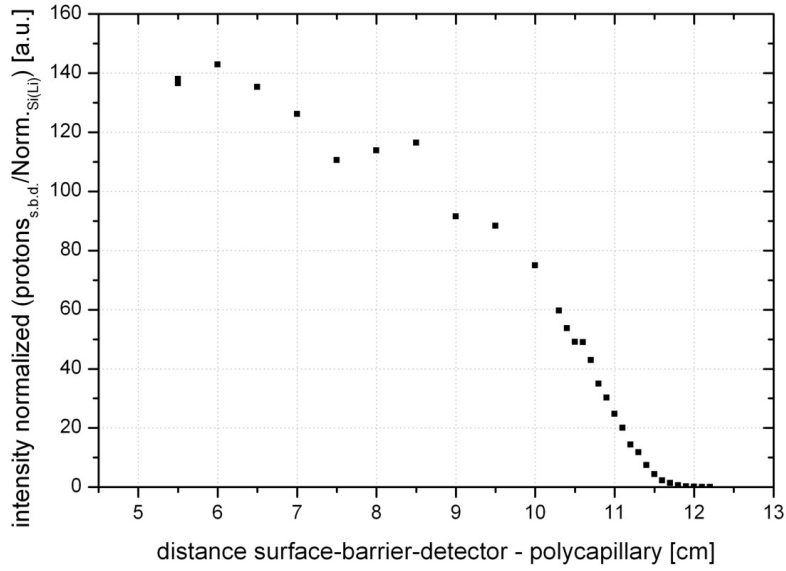


Figure B.5: Distance change between surface-barrier-detector and polycapillary exit.

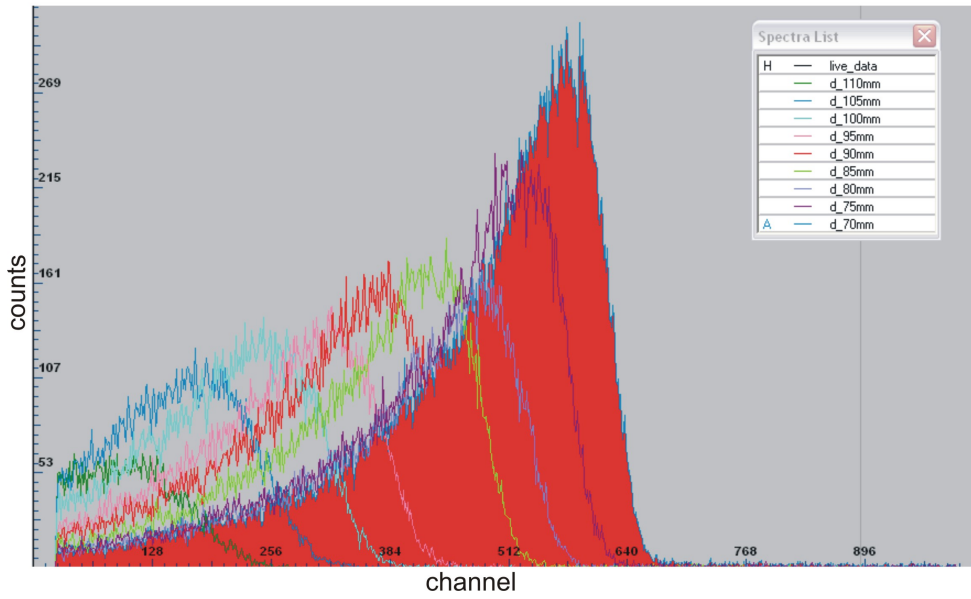


Figure B.6: Counted proton dependent on detector distance: selected spectra referring to figure B.5.

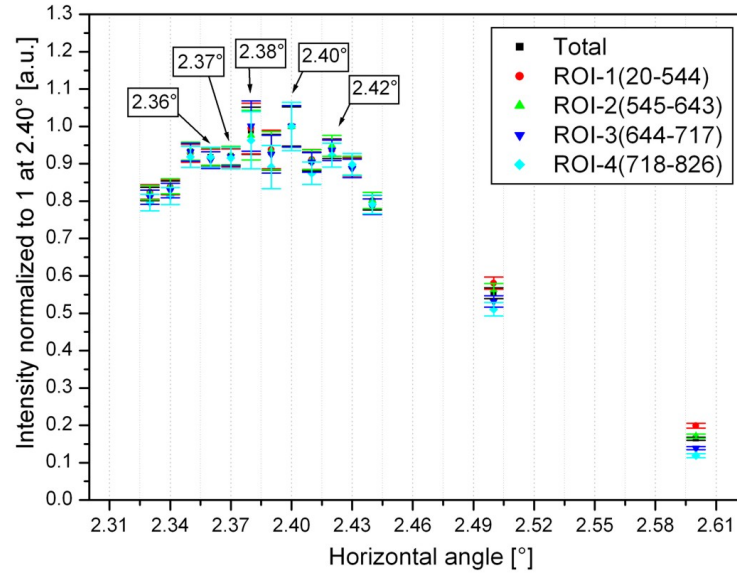


Figure B.7: Angle dependence of detected protons at the range of highest intensity, analyzed for different proton energies. The labeled points denote the angles where additional edge-scans were performed.

At the smallest distance possible another horizontal angle-scan with a step-size of 0.01° was performed (fig. B.7). A plateau appears in the normalized intensity dependent on the angle. It is approximately 0.08° expended. Referring to theoretical calculations half of the capillary tilt-angle, through which direct protons can still pass, equals 0.044° . At five labeled measuring points the proton-beam was characterized with an edge-scan by moving an impenetrable foil horizontal through the beam (see figure B.8, B.9, B.10, B.11 and B.12). No obvious change in the position of the beam by changing the angle of the capillary, which would prove the occurrence of total reflected protons, occurred. Furthermore, the horizontal beam divergence by tilting the polycapillary by an angle of 0.02° would be $\approx 52 \mu\text{m}$. This value is beyond the accuracy of the measurement (step-size of $\approx 500 \mu\text{m}$). The edge-scan at 2.36° (fig. B.8), which was carried out twice, demonstrates this clearly with an offset of about $200 \mu\text{m}$ between those ideally equal scans. However, the curves of the derivation plots, which represent the actual beam profile, seem to consist of two superimposed peaks. They could originate from a splitting of the beam into two parts, one that represents the direct protons and the other the particles that are scattered and reflected respectively (fig. B.13). Looking at the plot of the edge-scan at 2.36° (fig. B.8) it is visible that the left side of the derivative intensity is stronger. On the other hand the edge-scan at 2.42° (fig. B.12) shows the opposite behavior. As for the scans with angles in between, a tendency of the two peaks moving more

and more to each other until both superimpose completely at half way and move again apart, exists. The estimated distance between the two peaks at angle 2.36° is approximately $100 \mu\text{m}$. Assuming angle 2.39° as the capillary position parallel to the incident proton-beam, then the absolute tilt angle would equal 0.03° . This again would result in a theoretical dislocation of the total reflected beam from the direct beam of $\approx 77 \mu\text{m}$ at the measuring point.

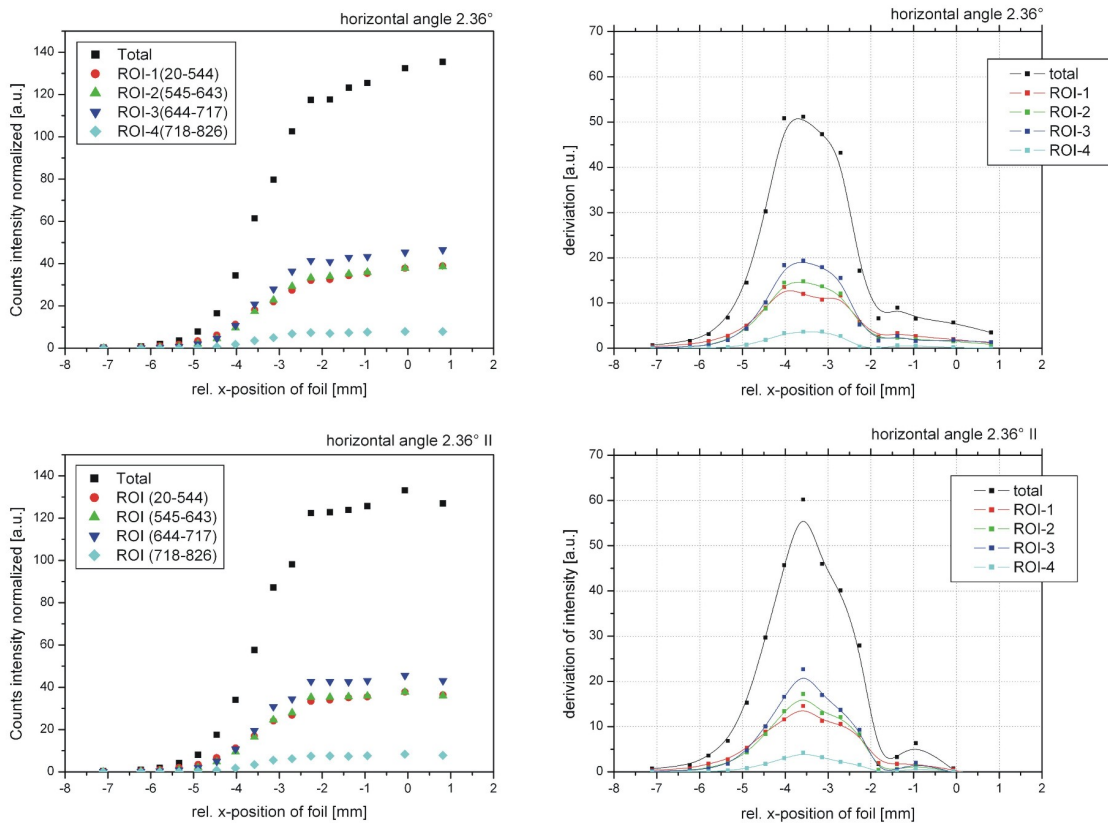


Figure B.8: Edge-scan at horizontal tilt-angle 2.36° , left side: original measured data, right side: derivation of the intensity.

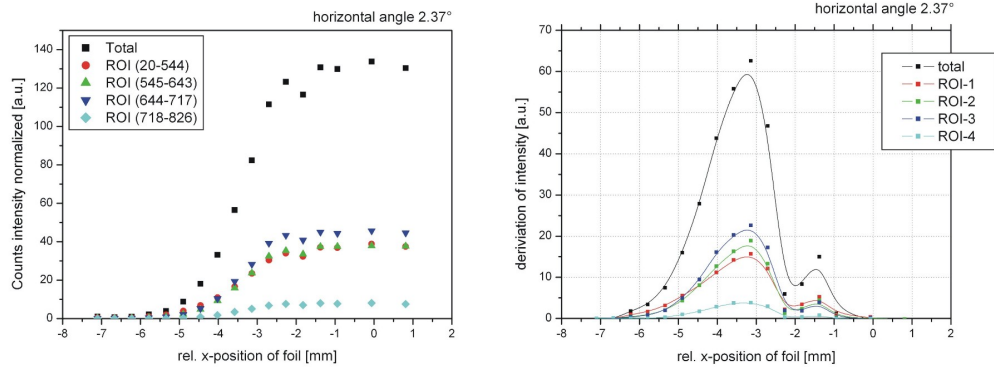


Figure B.9: Edge-scan at horizontal tilt angel 2.37°.

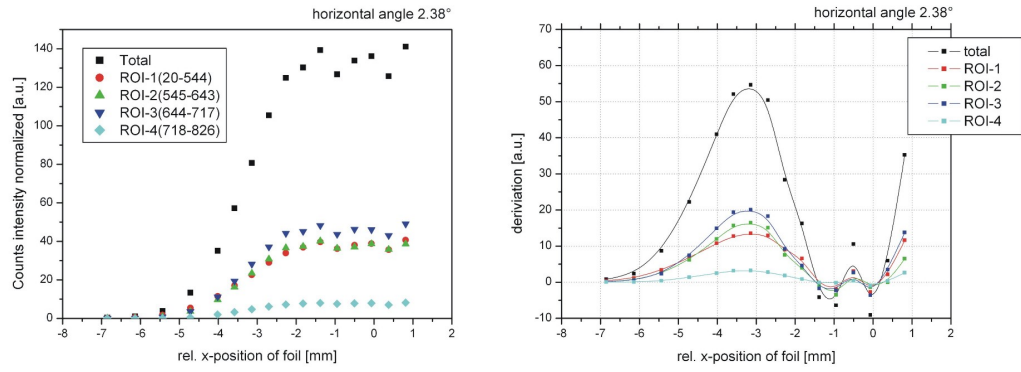


Figure B.10: Edge-scan at horizontal tilt angle 2.38°.

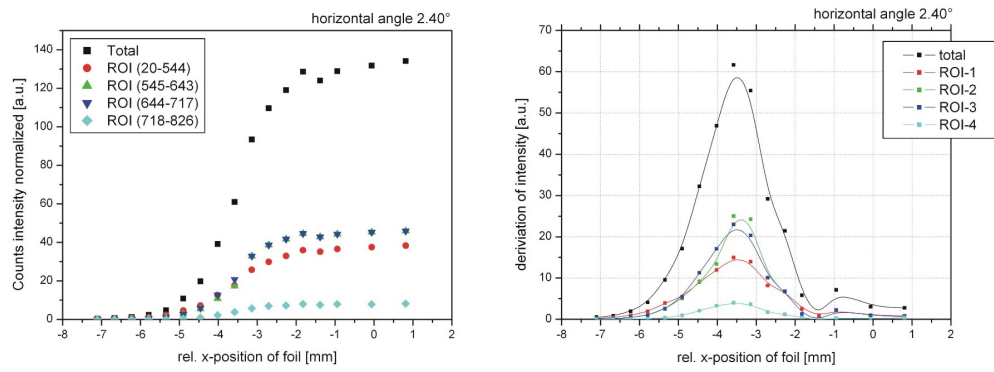


Figure B.11: Edge-scan at horizontal tilt angle 2.40°.

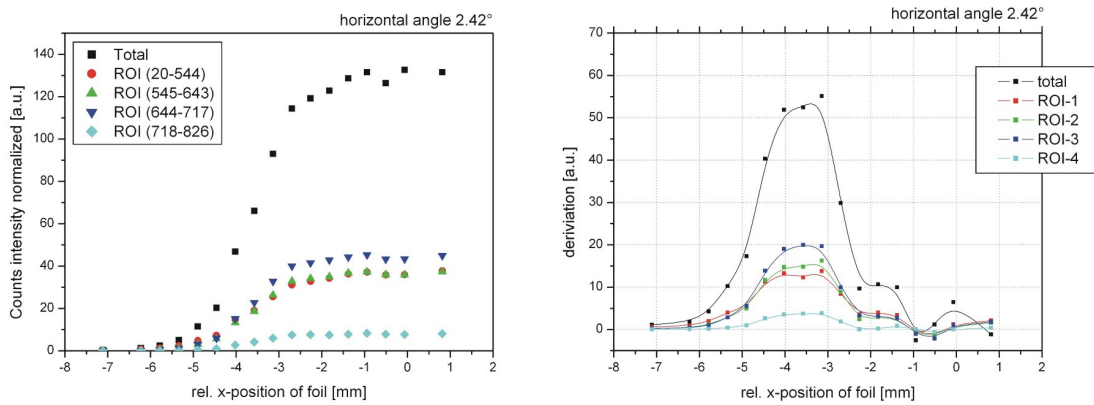


Figure B.12: Edge-scan at horizontal tilt angle 2.42° .

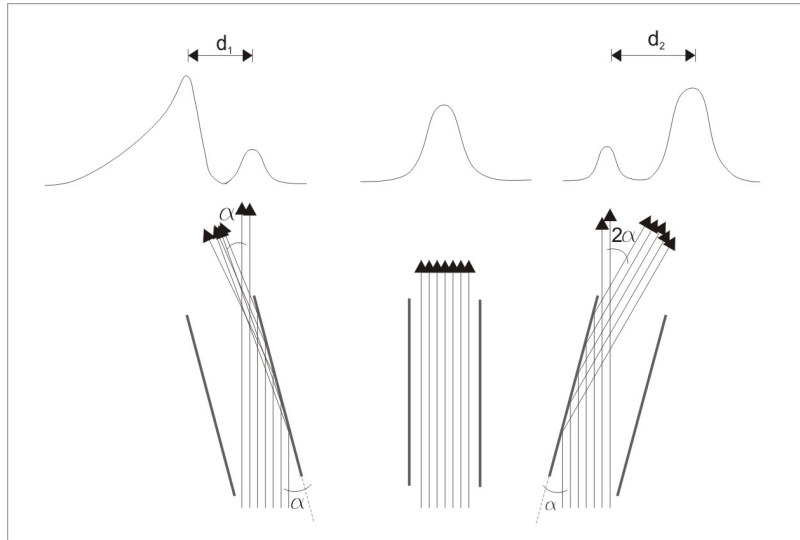


Figure B.13: Proton paths in the case of scattering (left) and of reflection (right) respectively.

Half lens structure 51mkl-02

Before starting the investigations with the parallel structure mkl-84 proton experiments with the half lens optic 51mkl-02 were performed. Due to mounting problems of the capillary (use of a motorized angle regulation) only a horizontal scan, to achieve the optimized position, could be accomplished (see figure B.14). Moreover, the center of rotation was too far away from the proton exit window. Hence, with every step of the horizontal angle motor the entrance side of the capillary had to be corrected in its position. This resulted in the large discoloration spot at the glass-optics entrance side (see figure B.1). Furthermore, not only the rotation center, but the capillary

itself was also some centimeter away from the exit window. Consequently the maximum achieved counting rate with this setup was only ≈ 600 counts/s. This is also due to the large proton beam extension after the great path length in air.

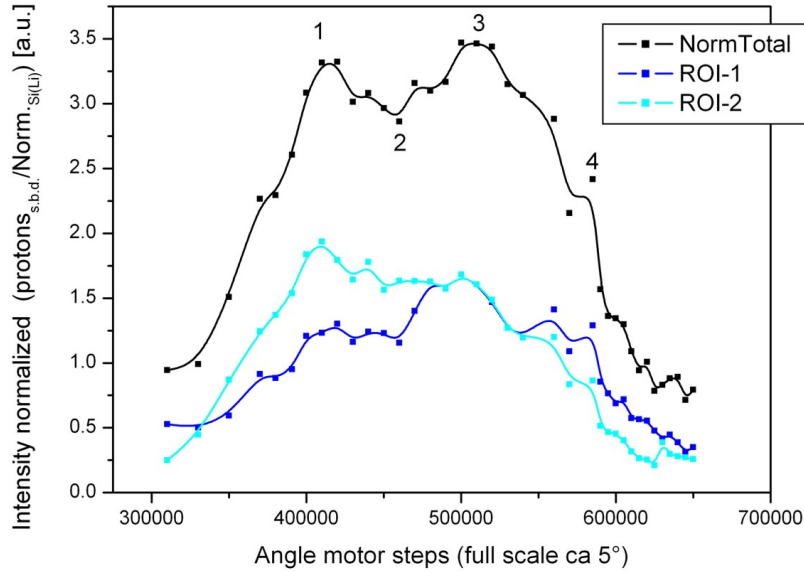


Figure B.14: Horizontal-angle-adjustment-scan of polycapillary halfpenn 51mkl 02

B.1.3 Conclusion and Outlook

This experiment could show that protons in the MeV range can penetrate through glass-capillary-optics. Next to the detected counting rate itself, the discoloration, not only at the entrance side but at the exit side of the capillary as well (see figure B.1), is evidence for the passing through of protons. There is a loss in intensity, but it can be confined to be less than 10^{-6} and it should be possible to improve this limit with a better alignment. Furthermore the behavior of the protons by tilting the capillary indicates that there are at least scattered protons. It suggests also the existence of reflections. Hence, more intensive investigation could be from great interest. Especially more precise measurements with focusing optics would be one of the next steps in this research.

Bibliography

- [1] V. Arkadiev, A. Bzhaumikhov, H.-E. Gorny, H.-E. Langhoff, and J. Schmalz. Capillary-based X-ray filters. *Proc. SPIE*, 2859,220, 1996. 19
- [2] B. Aschenbach. Grazing Incidence Refection and Scattering of MeV Protons. *Max-Planck Institut für extraterrestrische Physik*, 2007. 83
- [3] A. A. Bzhaumikhov, N. Langhoff, J. Schmalz, R. Wedell, V. I. Beloglazov, and N. Lebedev. Polycapillary Conic Collimator for Micro-XRF. In *SPIE Conference on X-Ray Optics, Instruments and Misions*, 1998. 18
- [4] T. Calligaro, J.-C. Dran, J. Salomon, and P. Walter. Review of accelerator gadgets for art and archaeology. *Nuclear Instruments and Methods in Physics Research B*, 226:29–37, 2004. 3
- [5] A. H. Compton. Total reflection of X-rays from glass and silver. *Physical Review*, 20:84, 1922. 14
- [6] A. H. Compton and S. K. Allison. *X-Rays in Theory and Experiment, second edition*. D. Van Nostrand, New York, 1935. 15
- [7] G. Demortier and J. Ruvalcaba-Sil. Differential PIXE analysis of Mesoamerican jewelry items. *Nuclear Instruments and Methods in Physics Research B*, 118:352–358, 1996. 1
- [8] Guelph Pixe Group. URL <http://pixe.physics.uoguelph.ca/xray/lineshape/>, 2008. 9
- [9] B. L. Henke, E. Gullikson, and J. C. Davis. X-ray Interactions: Photoabsorption, scattering, transmission and reflection at $E = 50\text{-}30000$ eV, $Z=1\text{-}92$. *Atomic Data and Nuclear Data Tables*, 54 (2), 1993. 16
- [10] J. Hubbel and S. M. Seltzer. Tables of X-Ray Mass Attenuation Coefficients and Mass Energy-Absorption Coefficients from 1 keV to 20 MeV for Elements $Z = 1$ to 92 and 48 Additional Substances of Dosimetric Interest. *NIST, Reference Data*, 5632, 1996. 51
- [11] D. Jembrih, C. Neelmeijer, M. Schreiner, M. Mäder, M. Ebel, R. Svagera, and M. Peev. Iridescent Art Nouveau glass - IBA and XPS for the characterisation of thin iridescent layers. *Nuclear Instruments and Methods in Physics Research B*, 181:698–702, 2001. 49

- [12] D. Jembrih-Simbuenger, C. Neelmeijer, M. Maeder, and M. Schreiner. X-ray fluorescence and ion beam analysis of iridescent Art Nouveau glass authenticity and technology. *Nuclear Instruments and Methods in Physics Research B*, 226:119–125, 2004. 49
- [13] S. Johansson and J. Campbell. *PIXE, A Novel Technique for Element Analysis*. John Wiley and Sons, 1988. 3, 11, 99
- [14] S. A. E. Johansson, J. L. Campbell, and K. G. Malmqvist. *Particle-Induced X-Ray Emission Spectrometry (PIXE)*, volume 133 of *A Series of Monographs on Analytical Chemistry and Its Applications*. John Wiley and Sons, chemical analysis edition, 1995. 10, 50, 99
- [15] T. B. Johansson, A. K. R., and S. A. E. Johansson. *Nucl. Instr. Meth.*, 84:141, 1970. 3
- [16] B. Kanngießer, A. Karydas, R. Schütz, D. Sokaras, I. Reiche, S. Röhrs, L. Pichon, and J. Salomon. 3D Micro-PIXE at atmospheric pressure: A new tool for the investigation of art and archaeological objects. *Nucl. Instr. and Meth. B* (2007), doi:10.1016/j.nimb.2007.09.019, 2007. 65
- [17] B. Kanngießer, W. Malzer, A. Fuentes Rodriguez, and I. Reiche. Three-dimensional micro-XRF investigations of paint layers with a tabletop setup. *Spectrochimica Acta Part B*, 60:41–47, 2005. 18, 31
- [18] B. Kanngießer, W. Malzer, and I. Reiche. A new 3D micro X-ray fluorescence analysis set-up First archaeometric applications. *Nuclear Instruments and Methods in Physics Research B*, 211/2:259–264, 2003. 1, 12
- [19] A. G. Karydas, D. Sokaras, C. Zarkadas, N. Grlj, P. Pelicon, M. Zitnik, R. Schütz, W. Malzer, and B. Kanngießer. 3D Micro PIXE - a new technique for depth resolved element analysis. *J. Anal. At. Spectrom.*, 2007, 2007. 1, 61
- [20] P. Kröpfel. *The Silverpoint Drawings of Albrecht Dürer: A Proton Induced X-Ray Emission Analysis (PIXE) with an External Proton Beam at VERA*. PhD thesis, University of Vienna, 2007. 1, 21, 65
- [21] M. A. Kumakhov. Neutron capillary optics: status and perspectives. *Nuclear Instruments and Methods in Physics Research A*, 529:69–72, 2004. 1, 83
- [22] W. Kutschera, P. Collon, H. Friedmann, R. Golser, P. Hille, A. Priller, W. Rom, P. Steier, S. Tagesen, A. Wallner, E. Wild, and G. Winkler. Vera: A new AMS facility in vienna. *Nucl. Instr. and Meth. B*, 123:47–50, 1997. 21
- [23] M. Maeder, D. Jembrih-Simbuenger, C. Neelmeijer, and M. Schreiner. IBA of iridescent Art Nouveau glass comparative studies. *Nuclear Instruments and Methods in Physics Research B*, 239:107–113, 2005. 49, 59

-
- [24] W. Malzer and B. Kanngießer. A model for the confocal volume of 3D micro X-ray fluorescence spectrometer. *Spectrochimica Acta Part B*, 60:1334–1341, 2005. 12
- [25] J. Maxwell, A. Weatherstone, M. Vormwald, and I. Campbell. *GUPIXWIN Manual*. University of Guelph, 2005. 50
- [26] P. Milota, I. Reiche, A. Duval, O. Forstner, H. Guicharnaud, W. Kutschera, S. Merchel, A. Priller, M. Schreiner, P. Steier, E. Thobois, A. Wallner, B. Wünschek, and R. Golser. PIXE measurements of Renaissance silverpoint drawings at VERA. *Nuclear Instruments and Methods in Physics Research B*, 266:2279–2285, 2008. 21
- [27] R. Mroccka, G. Zukocinski, and A. Kuczumow. Investigations of different trajectories of X-rays in capillaries. *Journal of Alloys and Compounds*, 362:88–95, 2004. 17
- [28] I. Orlic, S. Zhou, J. L. Sanchez, F. Watt, and S. M. Tang. Virtual PIXE and RBS laboratory. *Nuclear Instruments and Methods in Physics Research B*, 150:83–89, 1999. 7, 99
- [29] L. Parrat. Surface studies of solids by total reflection of X-rays. *Phys. Rev.*, 95(2):359–369, 1954. 16
- [30] Polycapillary X-ray optics Institute for Scientific Instruments. URL <http://www.ifg-adlershof.de/capillary-optics.htm>, 2008. 14, 99
- [31] A. Priller, R. Golser, P. Hille, W. Kutschera, W. Rom, P. Steier, A. Wallner, and E. Wild. First performance test of VERA. *Nuclear Instruments and Methods in Physics Research B*, 123:193–198, 1997. 21
- [32] M. Rodrigues, M. Schreiner, M. Mäder, M. Melcher, M. Guerr, J. Salomon, M. Radtke, M. Alram, and N. Schindel. The Hoard of Becin - Non-destructive analyses of the silver coins. In *37th International Symposium on Archaeometry, 12-16 May, Siena, Italy*, 2008. 49
- [33] D. Sokaras, A. Karydas, W. Malzer, and B. Kanngießer. Theoretical description of 3D Micro-PIXE intensities. Case 1: Layered materials. In *European Conference on X-Ray Spectrometry*, 2008. 61
- [34] E. Steinbauer. RBS V3.21 Ion scattering calculation. University of Linz. 42
- [35] A. Thompson. X-Ray Data Booklet, Center for X-Ray optics advanced light source, 2001. 5
- [36] K. Uhler, B. Woytek, M. Schreiner, M. Alram, and M. Gießer. *Technologische Studien 4/2007 Konservierung, Restaurierung, Forschung, Technologie*, chapter Metallanalytische Forschungen zur Denarprägung Kaiser Traians (98-117 n.Chr.), pages 69–101. Kunsthistorisches Museum, 2004. 47, 48, 101

- [37] Universität Bonn Helmholtz , Institut für Strahlen- und Kernphysik. URL <http://www.iskp.uni-bonn.de/gruppen/mommsen/promoanno/node1.html>, 2008. 14
- [38] H. R. Verma. *Atomic and Nuclear Analytical Methods*. Springer-Verlag Berlin-Heidelberg, 2007. 5, 99

List of Tables

2.1	Dimensions of polycapillaries	13
3.1	Dimensions of the H^+ -beam in 1cm distance, measured with a 20 μm -wire.	30
4.1	Metal foils for the depth scans.	32
4.2	Maximum transmission of polycapillaries during the alignment procedure.	34
4.3	FWHM in μm of the detection volume for the three types of polycapillary with respect to the X-ray energy.	37
4.4	FWHM and max. intensities referring to different distances of Polycapillary and target.	39
5.1	Selected set of Traian coins.	48
5.2	Information of the coins from the time of the Ottoman Empire, reign of Murad III from 1574 - 1595 and of Mehmed III from 1595-1603 respectively.	49
5.3	Element concentrations of Traian coins, comparison between results achieved at VERA and measurements performed at the Academy of Fine Arts Vienna, V = measured at VERA with PIXE, A = measured at Academy of Fine Arts Vienna with XRF, all values are in %. The symbol - indicates that this element could not be found in the measured spectra.	54
5.4	Element concentrations of the Ottoman Empire coins, comparison of the results achieved at VERA and the measurements performed at the Louvre laboratories in Paris, V = measured at VERA, L = measured at the Louvre, all values in %. The symbol - indicates that this element could not be found in the measured spectra.	57
5.5	Element concentrations in Glass 232 for different measuring points.	59
5.6	Element concentrations in Loetz Glass sample for different measuring points.	59
5.7	Element concentrations in Tiffany Glass sample T10 for different measuring points, front pos.1 and 2 were excited with an angle normal to the target surface, at the position with the description "surface" the sample was turned by almost 90 degrees to produce an grazing incidence angle.	60

List of Tables

B.1 Dimensions of the polycapillary-optics. 84

List of Figures

2.1	a)Sketch of characteristic X-ray production incident. b)De-excitation through Auger electron emission.	4
2.2	Notation of characteristic X-ray transitions including related energy levels, quantum numbers and electron occupation, [38].	5
2.3	Fluorescence yield as a function of the atomic number Z	6
2.4	Ionization cross section through proton bombarding for different elements (data taken from VIBA-LAB [28]).	7
2.5	Penetration depth and angular distribution due to scattering processes of protons in air and Fe.	8
2.6	X-ray mass attenuation coefficient for element Fe, data taken from NIST, Physical Reference Data. At ≈ 8 keV the ionization edge for the iron K-shell is visible.	9
2.7	Components of line-shape of a typical Si(Li) detector spectra, [14]. . .	10
2.8	Ranges and minimum detectable concentrations of elements as a function of atomic number and proton energy for organic specimens [13]. .	11
2.9	Intersection of excitation channel and detection channel.	12
2.10	Sketches of Polycapillaries: a) half-lens b) lens c) Poly-CCC	13
2.11	Sketch referring to the law of Snellius, the transition of electromagnetic waves from one material into another.	14
2.12	Structure of glass polycapillaries, the diameter of the hollow channel is in the order of some $10\mu\text{m}$. Fig. left and middle: Polycap. lens 73mls 08, Fig. right: closer look at structure - ifg Berlin [30]	14
2.13	Reflectivity of 10keV X-Rays with SiO_2 as reflector material.	17
3.1	Scheme of the Vienna Environmental Research Accelerator VERA. . .	23
3.2	Side view of the beam trajectories (without use of the Wienfilter) through the bending units starting from the accelerator exit.	24
3.3	Top view of the beam trajectories(without use of the Wienfilter), the achromatic point is located shortly before the Quadrupols.	24
3.4	PIXE setup at VERA.	25
3.5	Positioning lasers on a 2 Cent coin.	26
3.6	Detector Setup used for depth resolved PIXE measurements.	27
3.7	^{55}Fe spectra for energy calibration of the Si(Li)-detector.	28
3.8	^{55}Fe spectra for energy calibration of the Amptek-detector.	28
3.9	Beam profile in horizontal direction scanned with a $20\mu\text{m}$ Gold-Tungsten-wire.	29

3.10	Beam profile in vertical direction scanned with a 20 μm Gold-Tungsten-wire.	30
4.1	Foil-sandwich construction.	32
4.2	Foil-sandwich target during experiments with Poly-CCC 71mls-PCCC14.	32
4.3	Positioning scan in horizontal direction. Due to problems with the fixation of the housing the measuring points of the Poly-CCC show greater scatter.	33
4.4	Positioning scan in vertical direction.	34
4.5	Individual spectra of a Fe-Cu foil-sandwich depth-scan with a distance between the foils of 300 μm at the relative position 300 μm	35
4.6	Individual spectra of a Fe-Cu foil-sandwich depth-scan with a distance between the foils of 300 μm at the relative position -50 μm	35
4.7	Depth scan of a sandwich where a 3 μm thick Fe foil is the front layer and a 7 μm Cu foil is the second, the nominal distance between the foils equals 30 μm . The plot compares all three types of polycapillaries. The values for the measured foil distances are given in the box beneath the legend.	36
4.8	Sensitivity curves for different X-Ray energies referring to polycapillary half-lens 22mkl 06.	38
4.9	Sensitivity curves for different X-Ray energies referring to polycapillary lens 73mls 08.	38
4.10	Sensitivity curves for different X-Ray energies referring to Poly-CCC 71mls.	39
4.11	Change of distance between Poly-CCC entrance and target impact point.	40
4.12	Maximum of transmission dependent on energy in comparison with the different polycapillary types.	41
4.13	Scan of a Fe-Cu sandwich with a 30 μm distance, performed with half-lens 22mkl 06 (gray scales), intensity gain of front and back layer (colored scales).	42
4.14	Scan of a Fe-Cu sandwich with a 30 μm distance, performed with lens 73mls 08 (gray scales), intensity gain of front and back layer (colored scales).	43
4.15	Scan of a Fe-Cu sandwich with a 30 μm distance, performed with Poly-CCC 71mls-PCCC14 (gray scales), intensity gain of front and back layer (colored scales).	43
4.16	Comparison of nominal depth values to measured foil distances. The three strong deviating values of 22mkl-06 at 50, 200 and 300 μm are originating from a systematical error in the construction and are not used for further calculations.	44
4.17	Scan of a 2 Cent coin with half-lens 22mkl 06	45
4.18	Scan of a 2 Cent coin with lens 73mls 08	46
4.19	Scan of a 2 Cent coin with Poly-CCC 71mls	46

5.1	Scanning electron microscope picture of the cross-section of Coin # 41 [36].	48
5.2	Iridescent glass samples (from left to right): Glas232 in holder (unknown origin), Tiffany T10, Loetz sample in holder.	50
5.3	Intrinsic efficiency curve of our Si(Li) detector. The steep fall-off of the efficiency in the low energy region is due to absorbers, the decrease at high energy is related to the detector crystal thickness.	52
5.4	Cu content of ÖGUSSA Standards.	53
5.5	Ag content of ÖGUSSA Standards.	53
5.6	Comparison of Ag and Cu content in the Traian coins. V = PIXE results from VERA, A = XRF results from the Academy of Fine Arts.	55
5.7	Cross-section line-scans of Traian coin no. 34, the matrix elements Ag & Cu are assumed to be together a 100% of the content.	56
5.8	Cross-section line-scans of Traian coin no. 41, the matrix elements Ag & Cu are assumed to be together a 100% of the content.	56
5.9	Comparison of Ag and Cu content in the Ottoman coins. V = PIXE results from VERA, L = PIXE results from Louvre.	58
5.10	Comparison of spectra taken from the front (light spot) side and back side of the Loetz glass sample.	60
5.11	Line-scan of the cross-section polish of Traian coin number 34, performed with the Poly-CCC.	62
5.12	Spectra taken from the surface side of the Tiffany sample T10 in comparison with the same measurement performed with the Poly-CCC in front of the Si(Li).	63
5.13	Depth scan of Loetz Glass sample measured at a light colored surface spot.	64
A.1	Depth scan of Cu-Ti sandwich measured with half-lens 22mkl06 . The green rectangles indicate the Gross counts from Cu $K\alpha$ + Cu $K\beta$. The FWHM and the difference of the center values are given in the insert.	68
A.2	Depth scan of Cu-Ti sandwich measured with Poly-CCC 71mls	69
A.3	Depth scan of Cu-Ti sandwich measured with half-lens 22mkl06	69
A.4	Depth scan of Cu-Ti sandwich measured with lens 73mls08	70
A.5	Depth scan of Cu-Ti sandwich measured with Poly-CCC 71mls	70
A.6	Depth scan of Cu-Ti sandwich measured with lens 73mls08	71
A.7	Depth scan of Cu-Ti sandwich measured with half-lens 22mkl06	71
A.8	Depth scan of Cu-Ti sandwich measured with lens 73mls08	72
A.9	Depth scan of Cu-Ti sandwich measured with Poly-CCC 71mls	72
A.10	Depth scan of Fe-Cu sandwich measured with half-lens 22mkl06	73
A.11	Depth scan of Fe-Cu sandwich measured with half-lens 73mls08	73
A.12	Depth scan of Fe-Cu sandwich measured with Poly-CCC 71mls	74
A.13	Depth scan of Fe-Cu sandwich measured with half-lens 22mkl06	74

A.14	Depth scan of Fe-Cu sandwich measured with lens 73mls08	75
A.15	Depth scan of Fe-Cu sandwich measured with Poly-CCC 71mls . . .	75
A.16	Depth scan of Fe-Cu sandwich measured with half-lens 22mkl06 . . .	76
A.17	Depth scan of Fe-Cu sandwich measured with lens 73mls08	76
A.18	Depth scan of Fe-Cu sandwich measured with Poly-CCC 71mls . . .	77
A.19	Depth scan of Fe-Au sandwich measured with lens 73mls08	78
A.20	Depth scan of Fe-Au sandwich measured with Poly-CCC 71mls . . .	78
A.21	Depth scan of Au-Fe sandwich measured with lens 73mls08	79
A.22	Depth scan of Au-Fe sandwich measured with Poly-CCC 71mls . . .	79
A.23	Depth scan of Ti-Fe sandwich measured with lens 73mls08	80
A.24	Depth scan of Ti-Fe sandwich measured with Poly-CCC 71mls	80
B.1	Photographs of the polycapillary-optics, a) half lens 51mkl 02 , b) parallel structure mkl-84	85
B.2	Setup of proton channeling experiment	85
B.3	Detected protons with and without polycapillary at detector position 12.4 cm.	86
B.4	Angle-adjustment of polycapillary parallel structure mkl-84.	86
B.5	Distance change between surface-barrier-detector and polycapillary exit.	87
B.6	Counted proton dependent on detector distance: selected spectra referring to figure B.5.	87
B.7	Angle dependence of detected protons at the range of highest intensity, analyzed for different proton energies. The labeled points denote the angles where additional edge-scans were performed.	88
B.8	Edge-scan at horizontal tilt-angle 2.36° , left side: original measured data, right side: derivation of the intensity.	89
B.9	Edge-scan at horizontal tilt angle 2.37°	90
B.10	Edge-scan at horizontal tilt angle 2.38°	90
B.11	Edge-scan at horizontal tilt angle 2.40°	90
B.12	Edge-scan at horizontal tilt angle 2.42°	91
B.13	Proton paths in the case of scattering (left) and of reflection (right) respectively.	91
B.14	Horizontal-angle-adjustment-scan of polycapillary half lens 51mkl 02	92

Acknowledgments

At first I want to thank Walter Kutschera and Robin Golser to give me the possibility to do my diploma thesis at the VERA facility and to give me financial support for visiting conferences and other laboratories. Additionally, my thanks go to the whole VERA staff for their help and for the good working atmosphere.

Especially I want to say thank you to:

Robin Golser for his support, motivation and his trust in me and my work

Oliver Forstner for his help with tuning the accelerator

Alfred Priller for knowing the accelerator VERA so well and the immediately reparations in the case of technical emergencies

Peter Steier for his valuable suggestions during tuning processes, for the fabulous Thursday lunches and for introducing pink-lime-green pasta to me

the Pixlinge for the good collaboration

Martin for the help with the beam trajectory simulations

my office colleagues Franz and Kathi for their patience and their philosophical input

Ewald Friedl, Johann Lukas, Wolfgang Hieß and Gabi Obstmayer for their exact and fast production of all the small and big work-pieces

Aniouar and Semfira Bjeoumikhov from ifg Berlin for providing polycapillary-optics required for our investigations with X-rays and especially for the experiments with protons

Birgit Kanngießner from the TU Berlin for borrowing us the half-lens polycapillary

Manfred Schreiner and Marta Rodrigues from the Academy of Fine Arts in Vienna for providing art historical samples

Roman Schütz from the TU Berlin with whom I successfully carried out experiments about guiding protons through polycapillary-optics

Furthermore I want to thank my parents for their mental and financial support and that they always believe in me, my friends for their encouragement and last but not least Tom for his help with developing the software as well as for his patience, his encouraging words and for being my british boy.

Curriculum vitae

Name: Lea Reichhart

Date of birth: May 30th, 1984

Place of birth: Wels

Nationality: Austria

Education

1994-1998: WRG Körnerstraße, Linz

1998-2003: HTBLA Hallstatt f. Innenraumgestaltung u. Holztechnik

June 2003: Matura *mit ausgezeichnetem Erfolg*

since October 2003: Diploma study of *physics* at the University of Vienna

since October 2004: Diploma study of *intermedia art* at the University for applied arts of Vienna

July 2006: Internship at the Stefan-Meyer-Institut Vienna for subatomic physics, with a two week stay at the Paul Sherrer Institut in Switzerland (studies of pionic hydrogen)

August 2006 - February 2007: ERASMUS study visit at the Universitat Autònoma de Barcelona

July/August 2007: Internship at the Stefan-Meyer-Institut Vienna for subatomic physics, with a three week stay at CERN, Switzerland (investigating the hyperfine structure of antiprotonic helium)

since October 2007: Diploma thesis at VERA, Isotopic Research, Faculty of Physics, University of Vienna (supervisor: Prof. Robin Golser):
"Depth-resolved PIXE analysis with a polycapillary X-ray lens"

Lebenslauf

Name: Lea Reichhart

Geburtsdatum: 30. Mai 1984

Geburtsort: Wels

Staatsbürgerschaft: Österreich

Ausbildung

1994-1998: WRG Körnerstraße, Linz

1998-2003: HTBLA Hallstatt f. Innenraumgestaltung u. Holztechnik

Juni 2003: Matura *mit ausgezeichnetem Erfolg*

seit Oktober 2003: Studium *Physik Diplom* an der Universität Wien

seit Oktober 2004: Studium *Medienübergreifende Kunst* an der Universität für Angewandte Kunst Wien

Juli 2006: Praktikum am Stefan-Meyer-Institut Wien für subatomare Physik, mit einem zweiwöchigen Aufenthalt am Paul Scherrer Institut, Schweiz (Untersuchung von pionischem Wasserstoff)

August 2006 - Februar 2007: ERASMUS Studienaufenthalt an der Universität Autònoma de Barcelona

Juli/August 2007: Praktikum am Stefan-Meyer-Institut Wien für subatomare Physik, mit einem dreiwöchigen Aufenthalt in CERN, Schweiz (Untersuchung der Hyperfeinstruktur von antiprotonischem Helium)

seit Oktober 2007: Diplomarbeit bei VERA, Isotopenforschung, Fakultät für Physik, Universität Wien (Betreuer: Prof. Robin Golser):
"Depth-resolved PIXE analysis with a polycapillary X-ray lens"

